KAUNAS UNIVERSITY OF TECHNOLOGY

ALIONA ILJINA

NEUTRALIZATION OF AlF_3 PRODUCTION WASTE AND ITS APPLICATION FOR THE HYDROTHERMAL SYNTHESIS OF C-S-H

Doctoral Dissertation
Technological Sciences, Chemical Engineering (05T)

2017, Kaunas

This dissertation was prepared in the department of Silicate Technology, Kaunas University of Technology in 2013–2017. The scientific research was funded by Research Council of Lithuania.

Scientific supervisor:

prof. dr. Kestutis Baltakys (Kaunas University of Technology, Technological Sciences, Chemical Engineering (05T)).

Doctoral dissertation has been published in:
http://ktu.edu

Editor:

Armandas Rumšas (Publishing Office “Technologija”)

ISBN xxxx-xxxx

The bibliographic information about the publication is available in the National Bibliographic Data Bank (NBDB) of the Martynas Mažvydas National Library of Lithuania

KAUNO TECHNOLOGIJOS UNIVERSITETAS

ALIONA ILJINA

AlF_3 GAMYBOS ATLIEKOS NEUTRALIZAVIMAS IR PANAUDOJIMAS KALCIO HIDROSILIKATŲ SINTEZĖJE

Daktaro disertacija
Technologijos mokslai, chemijos inžinerija (05T)

2017, Kaunas

Disertacija rengta 2013-2017 metais Kauno technologijos universiteto cheminės technologijos fakultete silikatų technologijos katedroj
Lietuvos mokslo taryba.

Mokslinis vadovas:

Prof. dr. **Kęstutis BALTAKYS** (Kauno technologijos universitetas, technologijos mokslai, chemijos inžinerija (05T)).

Interneto svetainės, kurioje skelbiama disertacija, adresas:
http://ktu.edu

Redagavo:

Armandas Rumšas (leidykla “Technologija”)

ISBN (įrašyti gautą ISBN kodą)

Leidinio bibliografinė informacija pateikiama Lietuvos nacionalinės Martyno Mažvydo bibliotekos Nacionalinės bibliografijos duomenų banke (NBDB)

Table of Contents

Abbreviations

C-S-H – calcium silicate hydrate
C/S – molar ratio of CaO and SiO_2
XRD – X-ray powder diffraction
STA – simultaneous thermal analysis
DSC – differential scanning calorimetry
TG – thermogravimetry
FT-IR – Fourier transform infrared spectroscopy
SEM – scanning electron microscopy
AAS – atomic absorption spectrometry
EDX – energy dispersive X-ray spectrometry
S_{BET} – the specific surface area of sample calculated by the BET equation
w/s – ratio of water and solid
CF – CaF_2
C – calcite
G – gyrolite
T – 1.13 nm tobermorite
Tr – truscottite
K – cuspidine
X – xonotlite
Z – Z-phase
C(I) – C-S-H(I)
H – hydrogarnet
W – wollastonite
AF – $AlF_3 \cdot 3H_2O$

Introduction

Relevance of the work

Landfills are one of the easiest solutions to the problem of waste disposal, but they occupy large areas, they are concentrated pollution sources of air, groundwater and soil. According to an EU Directive, solid waste landfilling is the least preferable option and should be limited to the necessary minimum in order to prevent or reduce as far as possible the negative effects on the environment. Unfortunately, AlF_3 production waste – silica gel – due to various impurities containing fluoride ions is not widely used or processed but is actually stored in landfill sites instead.

Most methods (chemical precipitation, nanofiltration, etc.) which have been developed in order to remove fluoride ions still have drawbacks including the high initial cost, the lack of selectivity, the low capacity, and the difficulty in operation or regeneration. Due to this reason, perspective neutralization methods are urgently required, and effective application areas of waste silica gel need to be found. Only fragmentary data on the neutralization of fluoride ions from the limited solubility of solid materials and waste during hydrothermal synthesis have been published in scholarly literature.

It is presumed that during hydrothermal synthesis of calcium silicate hydrates F^- ions in the AlF_3 production waste will be combined into a stable (up to 1418 °C) compound, calcium fluoride, and the synthesized product could be used in binders and in the building materials industry. For this reason, by creating the innovative technology of calcium silicate hydrate synthesis from AlF_3 production waste, two goals would be solved at once: the neutralization and/or utilization of this waste and the synthesis of new generation calcium silicate hydrate adsorbents.

The aim of this work is to examine the influence of AlF_3 production waste on the crystallization of low base calcium silicate hydrates and their adsorption capacity for heavy metal ions as well as to propose the expedient areas for the application of the above mentioned waste.

In order to achieve the aim of the work, we have to accomplish the following **goals**:

1. To determine the chemical and mineralogical composition of AlF_3 production waste and to evaluate the peculiarities of neutralization or removal of F^- ions from this waste.
2. To examine the influence of AlF_3 production waste and the molar ratios of CaO/SiO_2 (0.55, 0.66, 0.83, and 1.0) of the primary mixtures on the formation of low base calcium silicate hydrates and to compare with the data obtained in the pure mixtures.
3. By conducting an experiment, to evaluate and, according to thermodynamic calculations, to validate the formation mechanism of calcium silicate hydrates and their stability temperature as well as the duration intervals.
4. To investigate the stability of synthetic calcium silicate hydrates as well as formed CaF_2 at a temperature in the range from 600 to 1000 °C.
5. To evaluate the influence of adsorption kinetic parameters and adsorptive pH values on the reaction of Zn^{2+} ions with different crystallinity gyrolite samples and to describe these reactions by using adsorptionkinetic models.

6. To propose recommendations for the application of AlF_3 production waste.

Scientific Novelty of the Research

Fluoride ions which are present in AlF_3 production waste participate not only in the formation of CaF_2 but also intercalate into the structure of the formed calcium silicate hydrates, and also exchange the sequence of new compounds formation. It was proven that the stability of the formed CaF_2 in the temperature range between 600 and 1000 °C depends on the mineralogical composition of the synthesized products and the CaO/SiO_2 molar ratio. The adsorption reactions of gyrolite in the alkaline solution are specific to chemisorption process, which is confirmed by a pseudo second-order model.

Practical Significance of the Scientific Research

A method for calcium silicate hydrates synthesis combining the utilization of AlF_3 production waste and the immobilization of F^- ions in the formed products during hydrothermal treatment was presented. Synthetic calcium silicate hydrates can be used for zinc ions removal from alkaline solutions. A principal technological scheme has been designed for AlF_3 production waste neutralization and utilization by using Ca-containing compounds under static or hydrothermal conditions.

Approval and Publication of Research Results

The results of the research have been presented in 6 scientific publications included into the Thomson Reuters Web of Knowledge database: 2 of them were published in the *Journal of Thermal Analysis and Calorimetry*; 1 was presented in the *Desalination and Water Treatment*, 2 articles were delivered in the *Romanian Journal of Materials*, and 1 article was submitted to the *Materials Science (Medžiagotyra)* journal. The results of the dissertation have been reported in 5 conferences proceedings, 4 of which were international: "Medžiagų inžinerija" (2013, Lithuania), "BaltSilica" (2014, Poland), "Chemistry and Chemical Technology" (2014, Lithuania), "3rd Central and Eastern European Conference on Thermal Analysis and Calorimetry" (2015, Slovenia), "BaltSilica" (2016, Lithuania).

Structure and Content of the Dissertation

The dissertation consists of the introduction, a survey of the relevant scholarly literature, the experimental part, the results and discussion part, the conclusions, the list of references and publications on the dissertation topic as well as appendixes. The list of references includes 180 bibliographic sources. The main results are discussed on 104 pages illustrated in 15 tables and 50 figures.

Statements Presented for Defence

1. AlF_3 production waste changes the compound formation mechanism and also affects their thermal behaviour in comparison with the pure CaO-SiO_2-H_2O system during hydrothermal synthesis.
2. It was proven that the adsorption of gyrolite for zinc ions in the alkaline solution is specific to the chemisorption process, which was confirmed by a pseudo second-order model.

1. Literature Review

1.1. Solid Wastes and Their Utilization

Solid wastes are the unwanted or useless solid materials generated from combined residential, industrial and commercial activities in a given area (1–4). It may be categorized according to its origin (domestic, industrial, commercial, construction or institutional); according to its contents (organic material, glass, metal, plastic, paper, etc.); or, according to its hazard potential (toxic, non-toxic, flammable, radioactive, infectious, etc.) (5, 6). Despite the requirements set upon pollution control measures, this waste is generally dumped on solid ground or discharged into water bodies without adequate treatment, and thus it becomes a major source of environmental pollution and a health hazard. Therefore, it is necessary to find the best ways of utilizing such waste (7–9).

There are various techniques which can minimize the solid waste, such as incineration or combustion, resource recovery, recycling, composting, biological treatment, landfilling, etc. (10–12). According to the waste management hierarchy, landfilling is the least preferable option and should be limited to the necessary minimum. The objective of the EU Directive on the landfill of waste (European Council, 1999) is to prevent or reduce as far as possible the negative effects on the environment, in particular, on surface water, groundwater, soil, air, and on human health from the landfilling of waste by introducing stringent technical requirements for waste and landfills (13). According to an EU directive, all the member states were restricted to landfilling by 2006 a maximum of 75% of the total amount by weight of the solid waste produced in 1995. This target decreased to 50% in 2009 and to 35% in 2016 (13). Recently, according to EU directives, it has been recommended to change the manufacturing process by reducing the amounts of contaminants, to use advanced recuperative waste removal technologies and, prior to 2020, to prepare methods for the reuse and recycling of waste materials such as (at least) paper, metal, plastic and glass from households and possibly from other origins as far as these waste streams are similar to waste from households, and this share shall be increased to a minimum of 70% by weight (14).

Therefore, there is a tremendous scope for setting-up secondary industries for recycling and reusing huge quantities of solid waste as minerals or resources in the production of construction materials (15–18). Environmentally-friendly, energy-efficient, and cost-effective alternative materials produced from solid waste will show a good market potential to fulfil people's needs in rural and urban areas. In order to effectively utilize the solid waste in producing alternative construction materials, detailed physico-chemical, engineering, thermal, mineralogical and morphological properties of these types of waste need to be evaluated with good accuracy. The construction products from solid waste practically will be useless despite their good mechanical properties if the durability performance is not satisfactory. Therefore, rigorous quality control and assurance should be practiced for durability improvement while using solid waste in construction materials. In addition, the impact of solid waste on the durability performance of construction materials must be properly assessed before commercialization. The performance of

solid waste-based construction materials in real-life construction must also be evaluated prior to setting up secondary industries for recycling and utilization of solid wastes (18). In order to maximize the use of alternative construction materials produced from different types of solid waste and to make the lab-based production processes feasible in the real world, technology-enabling centres are needed in order to facilitate effective commercialization. The good mechanical and durability performance of the newer products, the dissemination of technologies emphasizing the cost-benefit analysis, and a feasibility assessment report will significantly contribute to the successful commercialization of the innovative processes (18). Alternative construction materials obtained from industrial, agro-industrial and mining solid waste have ample scope for introducing new building components, which will reduce the costs of construction to some extent. Therefore, entrepreneurs and construction agencies must be encouraged to develop new products and processes by using solid waste as raw materials thus paving the innovative way for setting up secondary industries.

1.1.1 Solid Waste of AlF_3 Production

Aluminum fluoride is used in many industrial processes. It is one of the minor constituents added to the electrolytic cells during the production of metallic aluminum. It is also used in the preparation of white enamels, as an anti-reflection coating in complex optical systems, as a constituent in welding fluxes, and in the preparation of fluorine-containing glasses (19).

Generally, it is well known that aluminum fluoride may be produced by stoichiometrically reacting hydrated alumina or an alumina-containing material with fluosilicic acid in an aqueous solution at elevated temperatures (20). Aluminum fluoride forms in the solution. Insoluble silica is also formed as one of the reaction products. The main process of the fluosilicic acid interaction with aluminum hydroxide can be described by the following reaction (19):

$$H_2SiF_6+2Al(OH)_3 \rightarrow 2AlF_3+ SiO_2 \cdot nH_2O +H_2O +Q$$

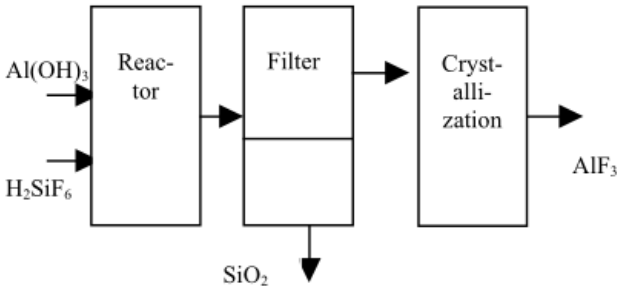

Figure 1.1. Process for production of aluminum fluoride (19)

The process of the production of aluminum fluoride and silica is schematically shown in Figure 1.1. AlF_3 is produced by neutralizing fluosilicic acid with aluminum hydroxide in the reactor by forming saturated aluminum fluoride solution and silica gel. The formed pulp is filtered hot, and the insoluble silica is easily separated with a filter. Solid aluminium fluoride trihydrate is crystallized from the

hot filtrate liquor. The obtained crystals of aluminum fluoride trihydrate are dehydrated to produce the final product of anhydrous aluminum fluoride (USA Patent, 1962). During the production process of AlF_3, a large amount of silica gel contaminated with F^- ions as a by-product is obtained, which is not widely used or processed, but is instead stored in landfill sites.

Due to the reason specified above, an investigation of utilization of by-product silica has been carried out by A. Krysztafkiewicz (21). The author's investigation heads in five different directions: recycling of waste silica into solutions of sodium or potassium metasilicate (the so-called water glass), Na_2SiO_3 and K_2SiO_3 of different modules, obtaining active silica as a filtration medium in pharmaceutical, food, and other industries, production of average medium fillers for polymers or carriers to be used in catalytic mass preparation, synthesis of substituent building materials from the by-product silicas with the use of chalks, application of waste silicas in polishing and cosmetic pastes. The fundamental condition that the waste silicas have to fulfil before being applied any further is their purification, i.e. the removal of fluorine compounds trapped on its surface. This is very important, especially in the case of waste silicas being applied as a raw material for the synthesis of C-S-H.

D. Vaičiukynienė et al. (22) investigated the use of the by-product of AlF_3 production waste as the basic ingredient of a new pozzolanic material. The goal of this study was to investigate the possibilities of using AlF_3 production waste washed in ammonia solution in cement stone specimens. The chemically treated silica gel additive was proven to reduce the amount of $Ca(OH)_2$ and $CaCO_3$ in hardened cement paste samples. This experimental research revealed that the density in hydrated samples reduces from 2220 kg/m^3 to 2030 kg/m^3 with the increase of the silica gel content from 0% to 35%. The compressive strength of the samples containing 10% of silica gel additive increased by 8.04% compared to the samples without the additive. SiO_2 additive used at the extent of 10% and 20% increased the maximum hydration temperature. In this case, the additive was shown to modify the hydration kinetics.

Idris and Saedused silica gel sludge is generated from a silica gel factory as an adsorbent (after its surface modification) for the removal of phenol from aqueous solution. It was found that, after the complete treatment process, the use of a raw adsorbent would be reduced to a greater extent and thus would become highly cost-effective (23).

Thus it is urgent to remove fluoride from solid wastes because fluoride ions can be leached and, due to the hazardous effects, may negatively affect groundwater.

1.1.2 The Methods for F^- ions Removal

The objective and principles of the environmental policy in the European Union (EU) consists of preventing, reducing and, as far as possible, eliminating pollution by giving priority to intervention at the source and ensuring prudent management of natural resources, in compliance with the principle of pollution prevention. The goal is an integrated pollution control so that to enable the reduction of emissions in order to promote the sustainable development (24). This concept aims at harmonizing the

economic, social and environmental dimensions of its development strategies and it is now a key feature of policy making in the EU.

Fluoride is one of the well-known anionic pollutants worldwide showing strong affinity with bone tissue-caused skeletal fluorosis (25). The contamination of ground water with fluoride can occur naturally by the dissolution of fluoride-rich minerals whereas artificial pollution occurs due to the waste water produced from mines, metal refining, plating industries, aluminum smelters and high tech-semiconductor factories (26). Each of these well-known processes produces a solid waste residue including significant amounts of soluble fluoride residual and a relatively high level of other contaminants which, presently, go to landfills or are simply allowed to accumulate on the smelter site as a tailings pile or in sludge ponds. This residue, when contacted with the environmental fluids (such as ground water), may contaminate water supplies and other valuable resources. A variety of treatment procedures have been reported for the removal of fluoride ions based on precipitation, ion exchange, reverse osmosis, electrodialysis, nanofiltration, membrane-based methods, electrocoagulation, and adsorption by employing various adsorbents (27, 28). The choice of the method depends on such conditions as the area, concentration, availability of resources, etc.

Reverse osmosis (RO). In membrane filtration, the water containing high concentration of pollutants is passed through a semi-permeable membrane. The membrane discards atoms on the criteria of size and electric charge. The pollutants are removed from the water and collected at the retentive side; whereas, clean water is recovered through permeate (29). In RO, the pressure greater than the natural osmotic pressure is applied to the concentrated side of the membrane. Kettunen and Keskitalo (30) evaluated the performance of a low energy RO membrane with a NF membrane. A membrane filtration plant of 1625 m^3/h capacity was constructed in Laitila, Finland, to control the F and Al concentration in drinking water. The comparative removal was above 95% and 76% for F and Al, respectively, and RO required ~1.6 bar excess feed pressure in comparison with that used in NF (30).

Nanofiltration (NF) is a relatively new process in contrast to RO, ultrafiltration (UF) and microfiltration (MF), and it is emerging as a practically functional technology in treating industrial wastewaters. Nanofiltration is characterized by attributes in-between reverse osmosis (RO) and ultrafiltration (UF). Regardless of the similarity in operation with RO, NF operates at a comparatively lower pressure yielding identical permeate flux even at a lesser pressure. NF removes less than 60% of the monovalent ions as opposed to 90% by RO membranes. RO can completely demineralize water with very low or practically no selectivity for monovalent ions but it suffers from high operating pressure, low permeate flux and high energy requirements (31, 32).

Chemical precipitation technique involves addition of aluminum salts along with lime to the F rich water followed by flocculation and sedimentation or filtration. In the first step, lime reacts with F impurities, such as NaF, HF, etc. to form insoluble calcium fluoride (33).

$$Ca(OH)_2 + 2F^- \rightarrow CaF_2 + 2OH^- \quad (1)$$

$$Ca(OH)_2\,(aq) + 2NaF\,(aq) \rightarrow CaF_2\,(s) + 2NaOH\,(aq) \quad (2)$$

Essentially, in the second step, aluminum sulphate or aluminum chloride, or both, is/are added. Aluminum salt acts as a coagulant and is commonly used for viable and effective fluoride removal from water. The basicity present in water with alum yields an aluminum salt, [$Al(OH)_3$], which is insoluble. It has been reported that the pH of the contaminated water increases up to 12; however, the best fluoride removal is achieved between the pH range of 6–7 (33). The dose of alum is typically around 20-fold the lime required. The fluoride from groundwater can be removed up to the extent of 96% from the initial concentration of 109 mg/L by using lime (34). Similar findings on fluoride removal by calcium salts have been confirmed by Jadhav *et al*. (35).

Eletrocoagulation (EC) can be effectively employed to treat oily wastewaters (36), dye and textile industry effluents (37) and removal of organic matter (38), heavy metals (39) and fluoride (40). EC is advantageous since no impurities are introduced whereas the useful content which is present in raw water can be retained during defluoridation. An electrocoagulation reactor typically consists of an electrolytic cell with an anode and a cathode. The passage of the electric current leads to the deterioration of the anode and cathode which may be made of the same or different materials (40).

Electrocoagulation deals with electrochemical production of destabilization agents, which leads to the neutralization of electric charge while removing pollutants. Charged particles coagulate together to produce a mass. Effective removal of pollutants by flotation and sedimentation is augmented by metal-based coagulants having a similar effect as the metal cations produced by the anode. The key reactions are as follows (41, 42):

$Al \rightarrow Al^{3+} + 3e$ at the anode (3)

$Al^{3+} + 3H_2O \rightarrow Al(OH)_3 + 3H^+$ (4)

$Al(OH)_3 + xF^- \rightarrow Al(OH)_{3-x}F_x + xOH^-$ (5)

$2H_2O + 2e \rightarrow H_2 + 2OH^-$ at the cathode (6)

The evolution of hydrogen bubbles at the cathode improves the fluoride ion mass transfer rates and also leads to the floating of the aluminum complex ($Al(OH)_{3x}F_x$) flocs at the top of the electrocoagulation system. Effective fluoride removal can be achieved by isolating the aluminum complex from the aqueous phase periodically. Therefore, the formation of aluminum complex [$Al(OH)_{3x}F_x$] results in the defluoridation of the polluted waters (41, 42).

Electrodialysis is another emerging technique for removing ionic compounds from aqueous media by using ion exchange membranes in which the applied electric field acts as a driving force and is responsible for the separation of contaminants (42). The application of the electric current between two electrodes results in the passage of cations to the cathode and anions to the anode through the negatively charged cation exchange membrane and the positively charged anion exchange membrane, respectively. The end result is the increased and decreased concentration of cations and anions in alternate partitions. The global trend is shifting towards electrodialysis as an alternate technique for defluoridation primarily because of its simplicity and capacity to overcome the shortcomings of the chemical processes (42).

Ion exchange (IE) has been highlighted in a number of reports due to the efficacy of ion exchange with other techniques (43). Usually, the ion exchange technique removes fluoride by adsorption rather than by exchanging ions. The fundamental reason is that the fluoride concentration is comparably lower than the concentration of other ions present in water. Cation exchange resins are more selective for fluoride removal than anion exchange resins (44). However, the defluoridation capacity and selectivity for fluoride is dependent on the type of resin. The loading of metal ions influences the fluoride removal drastically, owing to the variations in their properties (45). Ion exchange treatment has a great fluoride removal potential (up to 95%). However, the resins are costly, thereby making the entire ion exchange method expensive as well. Regenerating the resins is simple but it generates a large volume of fluoride-loaded waste which again is a problem (45).

Among all these techniques, adsorption methods are denoted by a higher number of advantages because of their greater accessibility, good economy, ease of operation, and effectiveness in removing fluoride from water to the maximum extent.

1.1.3 The Types of Adsorbents

Adsorption techniques have been fairly popular in recent years due to their simplicity as well as the availability of a wide range of adsorbents. There are many types of inorganic (activated alumina, zeolites, some clays, etc.), organic (activated carbon, polymers, peat, etc.) and synthetic (calcium silicate hydrates, silica, synthetic zeolites, etc.) adsorbents (46–48). The most important attributes of an adsorbent for any application are: capacity, selectivity, regenerability, compatibility and costs (49).

Activated alumina is a porous aluminum oxide which is distinctively known for its high surface area among other aluminum oxides, mechanical strength and amphoteric properties (50, 51). Activated alumina is a well-known adsorbent used widely as a support material for a broad spectrum of catalytic and adsorption applications. Examples of these applications include its usage as a support material in the defluoridation of drinking water and the removal of heavy metals from water (50). This material is also known for other aspects of a wide spectrum of industrial applications, such as its usage as an adsorbent in liquid and gas purification processes, usage in plasma spray coating for the production of advanced ceramics, usage in production of wear-resistant composites, etc. (50, 52, 53).

Zeolites are hydrated aluminosilicates crystalline solids, which, in addition to being used as adsorbents and ion exchangers in several industrial applications such as drying processes (54), water treatment and softening (55), agriculture and animal husbandry (56), mining and metallurgy (57), construction (58), started to be used at energy recovery and storage systems as well (59–61). The structural framework of zeolites consists of exchangeable alkaline and alkaline earth metal cations (normally, Na^{+}, K^{+}, Ca^{+2}, Mg^{+2}, etc.) as well as water. Zeolites are commonly used as an adsorbent because they have a large surface area, are denoted by low cost, and are easily obtainable materials (60).

Clay minerals are used as an adsorbent in many studies because of their low cost, high natural abundance and their numerous valuable properties, such as a large specific surface area, excellent capacity to exchange the cation and the anion, and their tendency to adsorb water in their interlayer space (62, 63). They feature a 2:1 or 1:1 layer structure resulting from the condensation of alternating silica tetrahedral (SiO_4) layers and aluminum octahedral layers [$Al(OH)_3$]. Clay surfaces are characterized by a permanent negative charge due to isomorphic substitution exhibiting consequently a low adsorption capacity of some anionic elements, and the removal efficiency of clays for heavy metals is normally lower than that of natural zeolites (64).

Activated carbon is one of the most widely used adsorbents employed to adsorb dyes and other organic compounds from water because it is denoted by a distinctive structure, a well-developed pore structure and surface properties, large surface area, low density, high chemical resistance and high adsorption capacity for various organic compounds (65–67). Moreover, activated carbon has also been used for many other advanced applications, such as catalyst supports, medicine, electrode materials, air filters and gas storage. Therefore, the world demand for activated carbons can be expected to dramatically increase (potentially rising at 8.1% per year to 2.1 million metric tons in 2018) (65). As a result, the application of activated carbons as an adsorbent might be limited because of its high cost.

There are a substantial number of other adsorbents; however, it should be underlined that many organic and inorganic adsorbents are denoted by a lower adsorption capacity, their adsorption process continues longer, or it is hard to regenerate adsorbents and to use them repeatedly. Meanwhile, the use of synthetic adsorbents has more advantages: by changing synthesis conditions (such as the CaO/SiO_2 and water/solid ratios, isothermal curing temperature and duration, stirring intensity, cooling rate), the crystallite size of the synthesis products, the crystal shape and the composition can be controlled, and organic/inorganic anions/cations having a low affinity for these compounds group can be intercalated (68).

Many authors (69–72) have reported that calcium silicate hydrates prepared under hydrothermal treatment act as adsorbents for the removal of heavy metal ions.

1.2. Classification, Synthesis and the Main Properties of Calcium Silicate Hydrates

Calcium silicate hydrates (C-S-H), whose formula is expressed by the correlation of constituent components: $xCaO{\cdot}ySiO_2{\cdot}pH_2O$ (indexes: x, y, p – the number of moles), essentially are a silicic acid salt (73). Many of these compounds occur in the nature as hydrothermal alteration products of calcium carbonate rocks and as vesicle fillings in basalts. They include many chemically and structurally distinct phases. Other calcium silicate hydrates can be produced either by air curing, e.g. like in cement or concrete, or hydrothermally by high pressure steam curing in an autoclave (73). The formation of these calcium silicate hydrates depends on the duration and temperature of hydrothermal synthesis, stoichiometric composition of the initial mixture (the CaO/SiO_2 (C/S) molar ratios), the granulometric composition

(grading) and the strain of the raw materials, the additives being used, the mixing intensity and a number of other factors (74–76).

There are more than forty crystalline calcium silicate hydrates covering the C/S ratios between 0.44–3.00. Low-base (C/S = 0.6–1.5) and high-base (C/S = 1.5–2.0) calcium silicate hydrates belong to the set of key binding compounds (73, 77, 78). They can be used as fillers for the production of rubber, plastics, paper, and paint (79); for cleaning the water contaminated with heavy and radioactive metal ions (80), for non-asbestos heat insulations (81), as adsorbents of organic and inorganic effluents (82), or as cation exchangers (83–86). Therefore, calcium silicate hydrates formed under hydrothermal conditions are the subject of numerous scientific studies.

It should be noted that the changeable composition and the large amount of interfering ions of various element into the crystal lattice structure of C-S-H complicate the investigation of the structure and properties of these compounds. Therefore, the crystal structures of not all calcium hydrosilicates have already been investigated, and, consequently, their classification is constantly evolving. The most recognized classification of C-S-H was delivered by H.F.W. Taylor and R.M. Roy, which was supplemented in 1996 by W. Kraus and G. Nolze, and in 2008 by I.G. Richardson (73). This classification consists of wollastonite, tobermorite, jennite, gyrolite, γ-Ca_2SiO_4, and other groups of C-S-H, formed under hydrothermal synthesis conditions.

Wollastonite group minerals include nekoite, okenite, xonotlite, foshagite, hillebrandite, wollastonite and pectolite. From the wollastonite group of calcium silicate hydrates, xonotlite ($Ca_6(Si_6O_{17})(OH)_2$) is of great practical importance and interest because this compound has been industrially produced as a main constituent for heat insulating materials, building materials and artificial wood due to its high stability at high temperatures and its fibrous crystal form (87). This compound can be synthesized at 190–400 °C when the molar ratio of the mixture is C/S = 1.0. Xonotlite is characterized by interplatelet distance *d* of 0.7 nm (76). Nocuń-Wczelik reports that the synthesis of xonotlite highly depends on the SiO_2 strain, and the temperature and duration of the synthesis. In addition, this author observes that xonotlite may be formed directly, without the formation of an intermediate mineral – 1.13 nm tobermorite (76).

Tobermorite group minerals are 1.4 nm tobermorite, 1.1 nm tobermorite, 1.13 nm tobermorite, 0.93 nm tobermorite, clinotobermorite, 0.9 nm clinotobermorite, oyelite, C-S-H(I) ($C/S \leq 1.5$) (76, 88). The 1.13 nm tobermorite is the most prevalent among calcium silicate hydrates found in the nature and is a main constituent of autoclaved calcium silicate products, such as sand-lime brick, autoclaved aerated concrete (AAC), thermal insulation board, fiber-reinforced calcium silicate sheets and other types of building materials. These products are made hydrothermally by using silica with lime or cement under saturated steam pressure at 170–210 °C for 5 to 8 h. Tobermorite is also known as a natural mineral, first discovered by Heddle (1954) at Tobermory, Scotland (89). Taylor, Claringbull and Hey (89) showed that natural tobermorite and "well-crystallized synthetic calcium silicate hydrate (I)" were essentially identical. Tobermorite has been studied by investigating both

natural and synthetic phases. Natural tobermorite is usually more highly crystalline than the synthetic counterpart.

Jennite group minerals are jennite, metajennite, C-S-H(II). The structure of the first two minerals is similar to that of poorly-crystallized synthetic calcium silicate hydrates. Jennite, $Ca_9(Si_6O_{18})(OH)_6 \cdot 8H_2O$, is a rare natural mineral, usually found in contact with tobermorite 14 Å (90). It can be synthesized in suspensions of $Ca(OH)_2$ and hydrous silica at a 60–100 °C temperature (90, 91). The ideal C/S ratio is 1.5, which is higher than that of 1.4 nm tobermorite (C/S ratio of 1) (91). The crystal structure of jennite was determined by x-ray diffraction refinement (90, 92). The structure of jennite is composed of tilleyite ribbons of edge-sharing calcium octahedral, with the Si–O dreierketten chains running along [010] and the additional calcium octahedral sitting between the chains (92). Upon dehydration at 70–90 °C, water molecules are lost, which alters the atomic environment of the interlayer Ca. In order to be of stable configuration, the structure shrinks in the *c* direction, leading to metajennite, $Ca_9[Si_6O_{16}(OH)_2](OH)_8 \cdot 2H_2O$. Above 350 °C, the Ca–OH groups of metajennite are eliminated thus forming an amorphous phase which finally transforms to wollastonite and larnite (β-Ca_2SiO_4) above 800 °C (93).

Gyrolite group minerals are gyrolite, fedorite, K-phase, Z-phase, reyrite, and truscottite. In recent years, the interest in gyrolite ($Ca_{16}Si_{24}O_{60}(OH)_8 \cdot 14H_2O$) has grown considerably because gyrolite can be used as an adsorbent for the removal of impure ions and has a greater adsorption capacity in comparison with other C-S-H (76). It was claimed that gyrolite is stable at 120–200 °C in hydrothermal conditions under saturated steam pressure. Truscottite ($Ca_{14}Si_{24}O_{58}(OH)_8 \cdot 2H_2O$) is formed at temperatures higher than 200 °C, although metastable gyrolite may be obtained at temperatures up to 270 °C (76, 94). It is assumed that gyrolite is formed only at temperatures higher than 120 °C. The results of the research showed that the optimal temperature of the synthesis of gyrolite is rather high (approximately 200 °C) and that the duration is long (32 h) when amorphous $SiO_2 \cdot nH_2O$ is used as the SiO_2 component (94).

γ-Ca_2SiO_4 group minerals are calcium chondrodite, kilchoanite,γ-Ca_2SiO_4. These compounds are formed at hydrothermal treatment conditions. Kilchoanite $Ca_6(SiO_4)(Si_3O_{10})$, (C/S = 1.5) was the first mineral found with both isolated tetrahedra (Q0) and finite triple chains. The silicon tetrahedra are connected to 6-fold and 8-fold coordinated calcium atoms. The triple chains contain one Q_2 tetrahedron and two Q1 tetrahedra. The number of chains and isolated tetrahedra is equal in kilchoanite, so there are $\frac{1}{4}Q_0$, $\frac{1}{2}Q_1$ and $\frac{1}{4}Q_3$ tetrahedra in the structure (95). Garbev *et. al*. (95) described that kilchoanite manifests a direct relationship between the degree of polymerization and the temperature of formation. Mitsuda (1971) and Taylor (1972) reported that kilchoanite could be prepared from mixtures of lime and quartz at 280–600 °C and at 500–1000 bars.

Other calcium silicate hydrate compounds are afwillite, cuspidine, α-C_2SH, dellaite, jaffeite, killalaite, poldervaartite, rosenhahnite, suolunite, tilleyite. Most of these compounds are less significant for cement and binding materials chemistry. However, recently, the synthesis, properties and structure of α-C_2SH ($2CaO \cdot SiO_2 \cdot H_2O$) (a largely common compound formed during the hardening of

autoclaved calcium silicate products or the hydration of G-oil well cement pastes (96)) gained new interest because, on its basis, a new family of hydraulic cementitious materials (HCM) has been created. The alternative HCM is produced in a two-step process including hydrothermal treatment in an autoclave and mechanochemical grinding of the hydrothermal products together with quartz sand in 1:1 equality in terms of mass. According to several sources (97, 98), α-C_2SH forms quite easily under hydrothermal conditions from CaO and silicic acid as starting materials in the temperature range of 150–200 °C. Crystallization from quartz and $Ca(OH)_2$ is very slow. The best results were obtained when using C_2S polymorphs as the starting material (99). As indicated by H.F.W. Taylor in 1950, the rudiments of crystals aid the formation of α-C_2SH under hydrothermal conditions (99).

1.2.1. Synthesis and Properties of the Main Compounds: Gyrolite, Tobermorite and Xonotlite

The mineral **gyrolite** (Figure 1.2.), with the most likely chemical formula $Ca_{16}Si_{24}O_{60}(OH)_8 \cdot (14+x)H_2O$ (100) was first discovered on the Isle of Skye by Anderson in 1851. This compound is commonly found in volcanic and basaltic rocks, in voids or gaps, and it exists only with related minerals. At the laboratory scale, gyrolite can be synthesized by hydrothermal treatment of CaO and SiO_2 mixtures (100, 101).

Figure 1.2. Mineral gyrolite found in nature (102)

The hydrothermal synthesis of gyrolite is a long and complex process. However, this compound is usually prepared from an aqueous suspension of CaO and various forms of SiO_2 by hydrothermal treatment at temperatures of about 200 °C, when the molar ratio of CaO/SiO_2 equals to 0.66 (101). E.P. Flint *et al*. in 1938 (he was the first to synthesize gyrolite) reported that after 6–42 days of hydrothermal treatment at 150–350 °C temperature, when the molar ratio of the starting materials changes from 0.5 to 0.66, the only product of synthesis was gyrolite. Meanwhile, Mackay and Taylor in 1953 synthesized this compound at 150 °C temperature within 76 days of isothermal curing (103).

Moreover, in 1978, Kalousek and Nelson (104), and also in 1983 Stevula and Petrovic (105) found that gyrolite could also be prepared by the interaction of dicalcium silicate ($2CaO \cdot SiO_2$) with SiO_2 in aqueous suspension under hydrothermal conditions. Kalousek and Nelson determined that, under hydrothermal conditions,

gyrolite is stable prior to reaching 200°C temperature; meanwhile, at 300 °C temperature, truscottite was formed (104).

Later on, other scientists continued the studies of the synthesis of gyrolite (106, 107). It was declared that gyrolite is stable in the temperature range of 120–200 °C in hydrothermal conditions under saturated steam pressure. Truscottite is formed at temperatures higher than 200 °C, although metastable gyrolite may be obtained up to 270 °C (106). It is assumed that gyrolite is formed only at temperatures higher than 120 °C (106). At lower temperatures, a semicrystalline phase having no crystal structure (C-S-H gel) is obtained (106). At a variable C/S ratio, the formation of other calcium silicate hydrates which are stable at the given conditions (pressure, temperature) takes place(108). Therefore, C-S-H gel is transformed into a semicrystalline C-S-H (I). However, during sufficiently long hydrothermal treatment, this compound may turn into a metastable phase due to the formation of gyrolite. It has been shown that during hydrothermal treatment of gyrolite, an intermediary compound Z-phase is often formed with a 1.5 nm basic reflection characteristic (108).

Also, conditions for the formation and stability of gyrolite have been extensively studied by Baltakys and Siaučiūnas (94). The influence of SiO_2 modification on the crystallization process of gyrolite was determined. The authors showed that gyrolite does not form even within a week in the mixtures of CaO and amorphous SiO_2 at 150 °C under saturated steam pressure. The temperature increase positively affects the synthesis of this compound as pure gyrolite is produced at 175 °C after 72 h, and after 32 h it is produced at 200 °C (94). It should be underlined that in the mixtures with quartz, the mechanism of compound formation is quite different. Due to a low quartz solubility rate in the temperature range from 150 to 200 °C, neither Z-phase, nor gyrolite is formed even after 72 h of hydrothermal curing. α-C_2S hydrate and C-S-H(II) prevail at the beginning of the synthesis, and they gradually recrystallize into 1.13 nm tobermorite and xonotlite (94).

Tobermorite ($Ca_5Si_6H_2O_{18}\cdot 4H_2O$) (Figure 1.3.) (89, 109) is one of the most industrially important calcium silicate hydrates because it is a major constituent of autoclaved aerated concrete (AAC). A typical manufacturing process of AAC includes hydrothermal treatment of a mixture of quartz sand, lime, cement, gypsum and some other additives at around 200 °C for several hours under saturated steam pressure. The mechanical properties of AAC are considered to be affected by the quantity and quality of tobermorite formed through this process (109). Kikuma *et al.* (110) investigated the formation process of tobermorite under hydrothermal conditions in detail.

Natural tobermorites are usually more highly crystalline than the synthetic ones; however, their rare occurrence is the main reason for the production of synthetic alternatives. Synthetic 11 A˚ tobermorites and their Al- and Fe-substituted forms have been readily synthesized under saturated steam or hydrothermal conditions at temperatures between 80 and 225 °C from a range of starting materials including various mixtures of the following: lime, zeolites, quartz, gibbsite, cement, clays, fly ash, sodium silicate and aluminum chloride, and more recently, a number of industrial by-products (112–114). Al-substituted 11 A˚ tobermorite has been

synthesized from newsprint recycling residue comprising gehlenite ($Ca_2Al_2SiO_7$), akermanite ($Ca_2MgSi_2O_7$), β-dicalcium silicate (Ca_2SiO_4) and anorthite ($CaAl_2Si_2O_8$) under hydrothermal conditions at 100 °C within 1–2 days in the presence of NaOH (112, 113). In a recent study, the hydrothermal alkaline activation of oil shale fly ash converted it into mainly 11 A˚ tobermorite after 24 h treatment under hydrothermal conditions at 160 °C in the presence of NaOH. Tobermorite fibers 40–100 mm in length and 0.1–1 mm in diameter were hydrothermally synthesized at 200 °C for 5 h while using a solution containing silicate ions and Ca(II)–EDTA complex precursor. The starting C/S molar ratio did not greatly influence the phase and morphology of tobermorite but determined its final composition. Komarneni *et al*. in 1988 (115) used microwave heating in tobermorite synthesis in order to increase the kinetics of crystallization. A highly crystalline Al-substituted tobermorite with high cesium ion selectivity was rapidly synthesized in 2h at 180 °C under microwave heating from two zeolites (natural phillipsite and Linde 3A zeolite), calcium oxide, sodium silicate, aluminum chloride and sodium hydroxide (115).

Figure 1.3. Mineral tobermorite found in nature (111)

Xonotlite ($Ca_6Si_6O_{17}(OH)_2$) (Figure 1.4.) was described first by Rammelsberg in 1866 in contact-metamorphic limestones of Tetela de Xonotla, Mexico and can be found in nature as a vein-forming mineral in many different localities. Xonotlite is formed mainly as a product of Ca-metasomatism in the contact-zone of Ca-bearing rocks with igneous (often ultramafic) rocks (116). Xonotlite crystallizes in monoclinic symmetry and is usually forming acicular to fibrous crystals up to centimetre size (116).

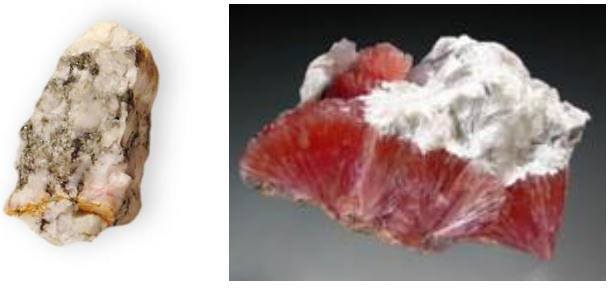

Figure 1.4. Mineral xonotlite found in nature (117)

Xonotlite has been industrially produced as a main constituent for heat insulating material and building material because of its high stability at high

temperatures and fibrous crystal form (118, 119). Xonotlite can be prepared from a silica and calcium hydroxide suspension while using the hydrothermal process (120, 121). The xonotlite crystal formation mechanism from the suspension is complicated and dependent on the reactivity of the raw materials because the various intermediate reaction products are formed in the reaction processes (122, 123). For example, calcium hydroxide reacts with low quartz particles to form calcium-rich C-S-H (low crystalline calcium silicate hydrates) in the first reaction stage due to a low quartz dissolution rate. As the hydrothermal reaction temperature and steam increased, the Ca/Si ratio in C-S-H gradually decreased, which led to tobermorite and xonotlite crystallization.

Baltakys et al. (124) examined the stability and crystal morphology of C-S-H(I) in $Ca(OH)_2$, silica fume and H_2O systems under saturated steam pressure at various temperatures and observed that the final xonotlite phase can be obtained through an intermediate phase, C-S-H(I). Yanagisawa *et al*. (87) observed that xonotlite whiskers can be hydrothermally prepared directly by diffusing the constituent ions dissolved from low-quartz and calcium hydroxide placed separately into a multi-chamber autoclave. Arabi *et al*. (125) investigated the relationship between the structure, the formed phases and the strength of sand-lime bricks produced by autoclaving under different conditions and incorporation of granulated slag. They observed that the reaction products consisted mainly of 11 A˚ tobermorite and xonotlite, and tobermorite transformed into xonotlite as the autoclave temperature was increased (125).

1.2.2. The Influence of Additives on the Formation of Calcium Silicate Hydrates

The formation and stability of various calcium silicate hydrates depends on various factors such as the duration and temperature of hydrothermal synthesis, the stoichiometric composition of the initial mixture (CaO/SiO_2 (C/S) molar ratios), the granulometric composition (grading) and the strain of the raw materials, the mixing intensity, as well as on the additives used.

It is known that ions of various chemical elements can penetrate into the structure of calcium silicate hydrates. The effectiveness of each additive may vary depending on the raw material used, the process treatment and other factors. Scholarly literature indicates that the additive which contains sodium, and aluminum ions exhibits the greatest impact for the C-S-H formation (100, 126–129).

Baltakys and Siaučiūnas (130) determined the influence of γ-Al_2O_3, Na_2O and hydrothermal synthesis parameters on the gyrolite formation process at 200 °C when the molar ratios of primary mixtures were $CaO/(SiO_2 + Al_2O_3) = 0.66$ and $Al_2O_3/(SiO_2 + Al_2O_3) = 0$ or 0.025. These authors discovered that Na_2O additive positively affects the synthesis of gyrolite because the duration of hydrothermal treatment shortens almost 2–3 times (6 h, 200 °C) in comparison with pure mixtures. However, gyrolite is not stable in the mixture with Na_2O, and it already recrystallized into pectolite after 16 h of isothermal curing. Moreover, the presence of (Na_2O + γ-Al_2O_3) additive stabilizes gyrolite and prevents its transformation to pectolite (130).

The basicity of synthesized calcium silicate hydrates described in terms of the C/S molar ratio is influenced more by alkaline additives than by changes in temperature. Depending on the concentration of Na^+ ions, the ratio of water/solid materials and the initial composition of the mixture, the duration of the hydrothermal synthesis may be significantly reduced (129). Blakeman *et al*. found in 1974 that at a constant C/S molar ratio of 0.83 and a varying quantity of NaOH in the primary mixtures, various compounds are formed (C-S-H(I), 1.13 nm tobermorite, pectolite, xonotlite) (131).

Nocun-Wczelik (129) investigated the influence of additives containing sodium and aluminum oxides on the composition and properties of calcium silicate hydrates. This scholar discovered that during the hydrothermal treatment of CaO- and SiO_2-bearing components, Na^+ ions accelerate the formation of poorly crystallized calcium silicate hydrates but further transformation of this intermediate product into more-ordered, well-developed crystalline forms can be disturbed with some admixture content. Xonotlite is the final product of the synthesis if the C/S molar ratio of the primary mixture is equal to 1.0. However, if over 20% of Na_2O is added into the mixture, all of the intermediate products, which are ordered phases of calcium silicate hydrates, transform into tobermorite. Meanwhile, the formation of gyrolite or Z-phase in mixtures with lower C/S ratios (0.67 or less) is faster in pure suspensions, and, additionally, C-S-H(I) residue is present when Na_2O admixture of 5–10% is involved (129).

Miyake, Iwaya and Suzuki (1990) successfully synthesized Al-substituted gyrolite and used it for the exchange reactions of ions (K^+ and Cs^+) in aqueous solutions. Since the specimen has a smaller amount of Na^+ ions than substituted Al^{3+} ions, it was supposed that Ca^{2+}ions make up for the deficiency in order to keep the charge neutrality (100). Al-substituted gyrolite retained the crystal structure and showed the same behavior in case of heating and the same lamellar morphologies as the original gyrolite. In addition, the basal spacing of gyrolite, d-spacing 2.2 nm, was not altered after the uptake of K^+ and Cs^+ ions (100). Moreover, it is easier to intercalate K^+ ions than Cs^+ ions into the crystal lattice of this compound. However, the researchers noticed that Cs^+ ions are better absorbed by Al-substituted tobermorite (68, 100). Al-substituted gyrolite may be used to eliminate heavy metal ions and remove them from wastewaters, and this type of gyrolite is known for its selectivity to DNA (132, 133).

K. Baltakys and R. Siaučiūnas (134) examined and explained the influence of gypsum additive on the gyrolite formation process and a sequence of intermediary compounds formation in the $CaO\text{-}SiO_2\cdot nH_2O\text{-}H_2O$ system. They determined that the quantity of sulphur which penetrates into the crystalline structure of gyrolite depends not only on the synthesis conditions but also on the composition of the initial mixture. A larger amount of sulphate ions stimulates the formation not only of gyrolite, but also of $CaSO_4$. Gypsum additive has no influence on the re-crystallization temperature of C-S-H(I), Z-phase and gyrolite transforming into wollastonite. The composition of the initial mixtures is recommended to be calculated according to molar ratios. In other cases, upon increasing the amount of

sulphate ions, the basicity of the mixture decreases and it becomes more difficult to form gyrolite.

It is known that some of Ca^{2+} or Si^{4+} ions in the crystal lattice of calcium silicate hydrate (mainly 1.13 nm tobermorite, 1.13 nm-substituted tobermorites and xonotlite) can be substituted by various ions (Na^{+}, K^{+}, Cs^{+}, Cu^{2+}, Fe^{2+}, Zn^{2+}, Cd^{2+}, Pb^{2+}, Mg^{2+}) under the hydrothermal reaction, thus altering their physicochemical behavior. The effectiveness of each additive may vary depending on the properties of the raw materials, the parameters of the hydrothermal reactions and on other factors (135).

1.2.3. Adsorption Properties of Calcium Silicate Hydrates and Their Utilization

S. Komarneni *et al*. (115) reported that calcium silicate hydrates prepared under hydrothermal treatment act as a cation exchanger with some metal cations with Ca^{2+} or Si^{4+} in their lattice structure (69, 70, 83).

Tobermorite ion exchange capacity depends on its chemical composition as well as on the structure of the crystalline lattice. Naturally occurring and synthetic unsubstituted tobermorites are noted for their low ion exchange capacity. This is predetermined by the fact that Ca^{2+} ions in these compounds are inserted between separate layers and are connected by a strong chemical bond with the oxygen atoms (115). Aluminum substituted tobermorites are denoted by similar properties. Si^{4+} ions in their crystal lattice are replaced with Al^{3+} ions. However, the situation is changing when Na^{+} ions are inserted into an aluminum substituted tobermorite crystal lattice. Al^{3+} ions are isomorphously substituted for Si^{4+} ions in tetrahedral sites, and alkali metal ions, such as Na^{+}, are placed in the interlayer and compensate the deficient charge. Na^{+} is very mobile and easily passes into the solution being replaced by other ions with a higher oxidation degree. [Na^{+} + Al^{3+}]-substituted tobermorites also show selectivity for some cations, firstly for Cs^{+} and Rb^{+} (70, 136). Recent data indicates that this compound is selective to Sr^{2+} ion (137). Moreover, Fe^{3+} ion may interfere into the tobermorite crystal lattice during the ion exchange reaction. Such modified tobermorites may be used as a catalyst in various technologically important chemical reactions (70).

El. Korashy *et al*. (138) studied the adsorption reactions of the transition metal ions (Mn^{2+}, Fe^{2+}, Co^{2+}, Ni^{2+}, Cu^{2+}, Zn^{2+}, Pb^{2+}, Cs^{+}, Cd^{2+}, Hg^{2+}) with some synthetic crystalline calcium silicates such as xonotlite, gyrolite and β-wollastonite. The total amounts of ion uptake by these solids were found to be as follows (in the descending order): xonotlite – gyrolite – β-wollastonite. Moreover, the quantities of Fe^{2+}, Co^{2+} and Ni^{2+} ions taken up by xonotlite and wollastonite were found to be higher than those of the other cations. On the other hand, gyrolite showed low selectivity towards different elements. It should be underlined that the reaction of xonotlite and β-wollastonite with Fe^{2+}, Pb^{2+}, Cd^{2+} and Hg^{2+} leads to the precipitation of geothite [FeO(OH)], hydrocerussite [$Pb_3(CO_3)_2(OH)_2$], otavite [$CdCO_3$] and $HgCO{\cdot}2HgO$ phases. Meanwhile, the reaction of Cu_{2+} and Zn_{2+} ions with β-wollastonite or gyrolite leads to the precipitation of gerhardite [$Cu_2(OH)_3NO_3$] and zincate [$CaZnO_2{\cdot}XH_2O$] phases (69, 83).

It is known that gyrolite can adsorb more chemical elements than other C-S-H because the interlayer sheets with a thickness of about 2.2 nm (one of the largest in all of the calcium silicate hydrates) in gyrolite are available for the intercalation of a new guest by controlling the charge of the host (139).

Bankauskaitė *et. al*. (69) determined that gyrolite shows excellent cation exchange properties because almost of all of Cu^{2+} ions (99.5% removal efficiency) were intercalated into the structure of this compound depending on the initial concentration of copper ions in the alkaline medium. However, the experimental data obtained by V. Kasperavičiūtė *et al*. (71) showed that in the acidic medium, gyrolite acts as a chemosorbent which can adsorb as little as 41.48% of Cu^{2+} ions. It should be noted that the cation exchange capacity of gyrolite substituted with Na^{+} ions increases to 92.30 mg Cu^{2+}/g and is greater than tobermorite substituted with (Al^{3+} + Na^{+}) ions (53.22 mg Cu^{2+}/g) (100, 140).

Another investigation (101) indicated that gyrolite can be used as a cation exchanger for the separation of alkali metal hydroxides (K^{+} and Na^{+}) from their aqueous solutions or pollutant(s) via the $Ca^{2+} \leftrightarrow 2K^{+}$ or Na^{+} exchange process. It is important that the uptake of K^{+} and Na^{+} by gyrolite is larger than the uptake of these ions by another hydrated calcium silicate – xonotlite. Na^{+} ions inserted into the crystal structure of gyrolite have a positive influence on the gyrolite cation exchange capacity. In case of Cu^{2+} ions, the Na^{+}-substituted gyrolite ion exchange capacity is almost twice better than that for (Al, Na)-substituted tobermorite (101).

A. Bankauskaitė *et al*. (141) examined the intercalation mechanism of Co^{2+}, Ni^{2+}, Zn^{2+}, Mn^{2+}, Fe^{3+} ions into the gyrolite structure. It was found that the adsorption of Co^{2+} ions proceeded slower at the beginning of the process because, after 30 s, the amount of the adsorbed ions was equal to 3 mg Co^{2+}/g when the initial concentration was 0.25 g/dm^3. It was determined that within 30 s of the adsorption experiment, the removal efficiency of gyrolite for Zn^{2+} ions reaches 50% (12 mg Zn^{2+}/g). Meanwhile, the kinetics of Mn^{2+} ion uptake is more rapid than that with zinc ions. In this case, after 30 s of the course of the reaction, the removal efficiency of the adsorbent reaches 70% (17 mg Mn^{2+}/g). It was thus found that gyrolite showed extremely high and selective uptake of Fe^{3+} ions because the elimination of the mentioned ions is completed within 30 s (~98% of the ions is adsorbed). Researchers investigated that the selectivity sequence of the studied metal ions by gyrolite can be written as follows: $Co^{2+} > Zn^{2+}/Mn^{2+}/Ni^{2+} > Fe^{3+}$ (141).

Gyrolite adsorption for Fe^{3+} and Ni^{3+} ions was intensively studied by Žadavičiūtė *et al*. (142).Additionally, the adsorption kinetics was described by using pseudo first order and pseudo second order equations. It was determined that the adsorption capacity of gyrolite and the intrusion of heavy metal ions in its structure depends on the reaction time and the pH value of the adsorptive. It was observed that the incorporation of Fe^{3+} ions occurs more intensively than the incorporation of Ni^{2+} ions. It was found that, in the acidic solution, the intrusion of Fe^{3+} ions into the gyrolite structure proceeds by two types of chemical reaction mechanisms: substitution and addition. Meanwhile, nickel ions participated only in the substitution reaction: gyrolite-Ca^{0} + $Me^{x+} \leftrightarrow$ gyrolite-Me^{0} + Ca^{2+}. It was noted that the pseudo second order model fits well for the iron and nickel ions adsorption

mechanism. It was thus estimated that the adsorption reactions are not a reversible process and that the crystal structure of gyrolite is stable (142).

A highly important problem related with the adsorption process is the utilization of contaminated adsorbents. The stabilization/solidification (S/S) technique aims at immobilizing heavy metal contaminants by converting them into a less soluble form (stabilization) and encapsulating them by the creation of a durable matrix (solidification) (143–145). For the application of the S/S process, wastes are mixed with cementitious additives in order to form an inert and stable solid material which can be disposed to land safely (143). The goal of the S/S methods is to keep the hazardous waste components within the allowable limits established by regulations, to produce a solid material from liquid waste or sludge, to improve the physical and handling characteristics of the waste, to decrease the surface area, to inhibit the transfer of the waste contaminants among each other, and to limit the mobility of the components when they are exposed to leaching fluids (143). S/S processes not only improve the physical and chemical properties of the wastes, but are also cheap due to the use of the cheapest binders such as cement, lime, pozzolan if compared to other treatment techniques.

The solidification of heavy metals containing inorganic materials in mortars and concretes produced while using Ordinary Portland cement (OPC) is an effective way of immobilization, and the mechanism of the processes occurring in the course of immobilization, as well as the assessment of the effectiveness of solidification has been widely studied and discussed in numerous reports (146–149). A significant role in the immobilization process is attributed to the so-called C-S-H phase (calcium silicate hydrates) – the main component of a hardened paste (149). Absorbability, low permeability preventing the migration of liquids and the presence of small gel pores (micropores) are among the decisive factors affecting the high immobilization potential of C-S-H (149). The properties and the amount of C-S-H are highly bound with the content of mineral additions in the cementitious material. The positive effects of mineral additions on the properties of solidifying composites are listed below (149): additional amounts of C-S-H with lower C/S are formed; calcium aluminates and sulfoaluminates fill the pores (these are the products of the reactions between active components of mineral additions and $Ca(OH)_2$ evolved in the course of calcium silicate phases hydration (from cement)); the modification of the microstructure owes to the presence of the mineral addition (dense, compact C-S-H of low porosity, the presence of the addition in the form of small particles acting as fillers). The role of calcium aluminate and sulfoaluminate hydrates in the immobilization process should not be ignored. In the structure of calcium sulfoaluminates, the incorporation of mono- and bi-valent ions is possible. This relates both to anions and cations (149). Calcium sulfoaluminates play an exceptional role as Cr and Mo immobilizers by forming solid solutions with these elements (149). According to Gougar *et al*. (150), aluminum in ettringite may be replaced synthetically with Ni^{3+}, Co^{3+}, Cr^{3+} and Ti^{3+}. Instead of sulfate, AsO_4^{3-}, CrO_4^{2-}, SeO_4^{2-} or MoO^{4-} are incorporated. It is also possible to replace Ca^{2+} with Sr^{2+}, Cd^{2+}, Co^{2+}, Ni^{2+} and Zn^{2+}. The precipitated, insoluble hydroxides of heavy

metals, such as Cr(III), Pb, Zn, modify the porosity of the cement matrix – the total porosity is reduced, and the gel pore ratio increases (150).

A. Eisinas *et al*. (133, 151) determined that gyrolite substituted with Cd^{2+} ions can be immobilised in Ordinary Portland cement. It was found that, under normal conditions, the addition of adsorbents with impure Cd^{2+} ions could not have had any substantial effect on the mineralogical composition of OPC samples. It was also noted that Cd^{2+} ions were bound in the cement stone under all experimental conditions. In addition, the samples containing adsorbents with impure Cd^{2+} ions had a higher compressive strength than OPC samples.

****

Solid wastes are the unwanted or useless solid materials generated from combined residential, industrial and commercial activities in a given area. Despite requirements for pollution control measures, these wastes are generally dumped on land or discharged into water bodies without adequate treatment and thus become a major source of environmental pollution and a health hazard. The industry of aluminum fluoride generates a large amount of silica gel contaminated with F^- ions as a by-product, which is not widely used or processed, but is instead stored in a landfill site. Therefore, it is necessary to find the best ways of utilizing such waste. The problems associated with fluoride ion pollution could be reduced or minimized by precipitation, ultra-filtration, electrode deposition, reverse osmosis, etc. Most methods still involve drawbacks, including the high initial cost, the lack of selectivity, the low capacity, and the difficulty in operation or regeneration. Due to this reason, it is urgent to propose perspective neutralization methods and to find effective application areas of waste silica gel. Among various methods, adsorption is now recognized as one of the most effective methods for the removal of heavy metals from the environment. In addition, adsorption is the most widely used method because it is universal, denoted by low cost, and viable. There are many types of inorganic, organic and synthetic adsorbents. It is known that calcium silicate hydrates prepared under hydrothermal treatment are characterized as high capacity adsorbents for the removal of impure ions. Thus one of the utilization methods for AlF_3 production waste could be its application as SiO_2 containing raw material for the synthesis of calcium silicate hydrates.

2. Materials and Methods

2.1 Materials

1.**Calcium oxide**, which was produced by burning calcium hydroxide ("Stanchem," Poland, purity 97%) at 950 °C for 30 minutes and ground to the specific surface area S_a of 1190 m^2/kg, with the quantity of free CaO equal to 97.41%;
2. **Fine ground $SiO_2 \cdot nH_2O$** ("Reaktiv," Russia, purity 98%) having a specific surface area S_a = 1529 m^2/kg, with loss of ignition – 6.10%;
3. **Silica gel**, i.e., a waste product of AlF_3 production in the chemical plant of "Lifosa" (Kėdainiai, Lithuania) (with moisture content 60–65%), dried for 7 days at room temperature (20–25 °C) in the laboratory and for an additional 48 hours at 50 °C in the dryer, S_a = 964 m^2/kg);
4. **NaX zeolite** ("Reaktiv," Russia).
5. **Opoka** (Stoniškis quarry, Lithuania).
6. **Limestone** (Karpėnai quarry, Lithuania).
7. **$Zn(NO_3)_2$** solution (c = 0.3 g Zn^{2+}/dm^3), which was prepared by dissolving $Zn(NO_3)_2 \cdot 6H_2O$ ("Poch," Poland, purity 99%) in distilled water;
8. **Lime milk**, which was prepared by using the lime from AB "Naujasis kalcitas", Lithuania. The chemical composition of lime was determined according to the standard (LST EN 459-1:2010) (152) and the obtained values are written in Table 2.1.

Table 2.1. Chemical composition of lime

Parameters	Result
Active amount of CaO + MgO, %	84.3
Total amount of CaO + MgO, %	90.30
Free CaO, %	81.6
MgO, %	2.52
CO_2, %	2.65
SO_3, %	0.48
Ignition loss, %	3.16
Time of extinction, min	3.5
Temperature of extinction, °C	86

9. **Other pure chemical reagents** (acetone, HCl, K_2CO_3, Na_2CO_3, $AgNO_3$, NH_4Cl, HNO_3 (ρ = 1400 kg/m^3), NH_3, NH_4NO_3, NaOH, KOH, $(NH_4)_2CO_3$, NaF.

2.2 Methods

The Synthesis of Calcium Silicate Hydrates

The initial mixtures whOSE compositions correspond to the C/S molar ratios 0.55, 0.66, 0.83, and 1.0 were put in plastic vessels together with 5–6 grinding balls used in order to improve the blending quality. The obtained mxtures were stirred for 45 min at 49 rpm/min speed by using Shaker Mixer "Turbula T2F." The homogenized raw materials were mixed with distilled water to obtain the water/solid ratio in the suspension equal to 10. The hydrothermal synthesis was carried out in unstirred suspensions in 25 ml volume PTFE cells which were placed in a stainless steel autoclave ("Parr instruments 4566B" Germany) under saturated steam pressure

at 200 °C temperature for 4, 8, 16, 24, 32, 48, 72, 120, 168, 336, and 504 hours by applying extra argon gas in order to reach the pressure of 10 bar. The suspensions were filtered after synthesis, the products were rinsed with acetone so that to prevent carbonization of materials, then dried at 50 °C ± 5 temperatures for 24 h, and finally sieved through a sieve with an 80 μm mesh.

The Determination of Free CaO (152)

1 g of the sample was weighed and placed into a 250 cm^3 conical flask, poured with 150 cm^3 of distilled water, and 5–10 pieces of glass beads were added. The slurry was heated for 5 minutes. After that, the suspension was cooled down, the inner wall of the flask was sprayed with distilled water, and 2–3 drops of phenolphthalein indicator were added. Finally, the suspension was titrated with 1N HCl until the pink color disappeared. The amount of free CaO (*X*) in the sample was calculated by using the following equation:

$$X = \frac{V \cdot N \cdot 28.04 \cdot 100}{G \cdot 1000}, \quad (2.1)$$

Where *N* is the normality of HCl; *V* is the volume of titrated HCl, cm^3; 28.04 is CaO equivalent, g; *G* is the initial mass of sample, g.

The Chemical Analysis

The chemical analysis of the AlF_3 production waste was carried out according to the methodology developed by O.A. Alekin (153).

Standard method of SiO_2 chemical analysis. 1 g of the sample was mixed with sodium and potassium carbonate mixture (5 or 6 g) and put in a platinum crucible. The crucible was placed into a furnace and melted at 900 – 1000 °C temperature for 1 h. After fusion, the crucible was placed into a 200 cm^3 porcelain plate with distilled water in order to solidify the melt on the crucible wall while it was cooling down. Later, the crucible was put into a porcelain plate, a large amount of 10 % HCl was added and mixed until CO_2 gas was released from solution. After that, the crucible was removed from the porcelain plate, and this plate was being heated on the sand bath until the solution evaporated. Subsequently, the formed residue was powdered with a glass stick, a few drops of concentrated HCl acid was poured in, and the porcelain plate was left to cool down. After 30 min, hot distilled water was added into the porcelain plate in order to dissolve the chlorides. Then, the solution with the residue of SiO_2 was filtrated through an ash-free filter and rinsed with distilled water so that to eliminate chloride ions (the amount of chloride ions was proofed by adding one drop of clean filtrate and a drop of 1 % $AgNO_3$ solution on a glass). The obtained filtrate was used for the second chemical analysis of SiO_2 and, finally, both filtrate papers were put in the crucibles and heated at 1000 °C for 1 h. The amount of SiO_2 was calculated by using the following equation:

$$SiO_2 = \frac{a_1 \cdot 100}{a}, \% \quad (2.2)$$

Where a_1 is the mass of the heated residue after the experiment, g; *a* is the initial mass of the sample, g.

Standard method of Al_2O_3 chemical analysis. Al_2O_3 was determined in the obtained filtrate after SiO_2 separation. This solution was poured into a 250 cm^3

volumetric flask, diluted with distilled water to the indicated level and mixed. After that, 50 cm^3 of filtrate was poured into a 300 cm^3 glass vessel and heated until boiling. Then, 1.5 g of NH_4Cl, 3–4 drops of HNO_3 (ρ = 1400 kg/m^3), as well as 3–4 drops of methylorange indicator were added, and the amount of 10% ammonium was also added till the solution color in the glass changed into yellow. Subsequently, the formed precipitates were filtrated and rinsed with hot solution of 2% NH_4NO_3. The obtained filtrate was used for the second chemical analysis of Al_2O_3 and, finally, both filtrate papers were put into the crucibles and heated at 1000 °C for 20 min. The amount of Al_2O_3 was calculated by using the following equation:

$$Al_2O_3 = \frac{a \cdot 100}{m}, \% \quad (2.3)$$

Where *a* is the mass of the heated residue after the experiment, g; *m* is the initial mass of the sample, g.

The determination of fluoride. 1 g of the sample was put into a platinum plate and mixed with 10 g of sodium and potassium hydroxides mixture (5 g of NaOH and 7 g of KOH). After that, a platinum plate was put in a sand bath and heated for approximately 40 min. During the heating the mixture was intensively mixed with a platinum spatula. After fusion, the platinum plate was turned around so that the melt would solidify on the internal walls. Then, 150 cm^3 of distilled water was added, and the platinum plate was put into a boiling water bath in order to melt salts. Afterwards, 15 g of chemically pure $(NH_4)_2CO_3$ powder was added, which was melted by mixing with a platinum spatula, and plate was being held in a boiling water bath until the solution evaporated yielding dry salt. Subsequently, the salt was poured over with 150 cm^3 of distilled water and melted by mixing in the boiling water bath. As the next step, the hot solution with precipitates was poured into a 250 cm^3 flask, which was resistant against the variations of temperature. The solution in the flask was cooled down and diluted with water to the indicated level. After that, the solution was filtrated, and concentrations of fluoride ions in the solution were measured by using a Metler Toledo T70 potentiometer. The error of the selective electrode for F^- ions is ±1ppm (0.0001%).

The Elution of Fluoride

The elution of F^- ions from AlF_3 production waste to the aqueous phase was done by keeping the suspensions at different temperatures (25, 50, 75, and 95 °C) for 1 h when water-to-solid (w/s) ratios were 10 and 500. The neutralization of compounds containing F^- ions in AlF_3 production waste was performed by adding 6.5, 10, and 20 wt. % CaO to the system. The suspension was kept at 25 °C for 1 h when w/s = 10 and 500. The concentration of fluoride ions in the liquid medium and pH values were measured by using a Metler Toledo T70 potentiometer.

Adsorption Experiments and Kinetics Models

Adsorption experiments were carried out at a 25 °C temperature in thermostatic adsorber Grant SUB14 (“Keison products,” UK) by stirring 1 g of sample in 100 ml of $Zn(NO_3)_2$ aqueous solution (pH ~5.6) containing 0.3 g/dm^3 of Zn^{2+} ions for 120 min. In order to maintain the alkaline value of the solution (pH ~9.0) and to prevent

$Zn(OH)_2$ precipitation, the aqueous solution (c = 10%) of NH_4OH was used. The pH value was measured by a Hanna-developed instrument (Hi 9321, microprocessor pH meter). Calibration curves are given in Figure 2.1 for the determination of Zn^{2+} and Ca^{2+} ions concentration in the solution.

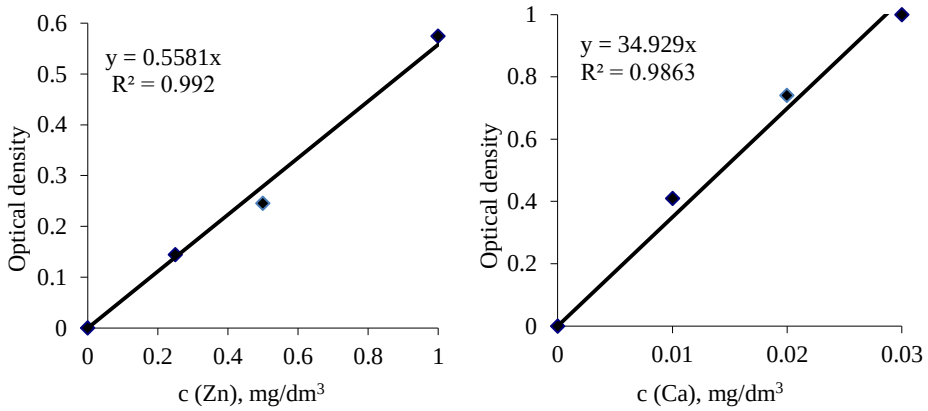

Figure 2.1. Calibration curves for the calculation of Zn^{2+} and Ca^{2+} ions concentration

In order to determine the kinetic parameters of adsorption reactions, kinetic models were developed and fitted for the adsorption process of the Zn^{2+} ions into gyrolite. The *first order adsorption kinetics* model was chosen analogous to the Largergren model (154, 155), which can be represented by the equation:

$$\frac{dX_t}{dt} = k_1(\Sigma X_e - X_t), \tag{2.4}$$

Where ΣX_e and X_t are the adsorption capacity at equilibrium and at time t_e, respectively ($mg \cdot g^{-1}$), and k_1 is the rate constant of pseudo first order adsorption (min^{-1}). After the integration and after applying boundary conditions t=0 to t=t_e and X_t=0 to X_t=ΣX_e, the integrated form becomes as follows:

$$log(\Sigma X_e - X_t) = \Sigma X_e - \frac{k_1}{2.303} t \ . \tag{2.5}$$

The *pseudo second order adsorption kinetic* model was chosen also analogous to these models (154, 155), which can be expressed as:

$$\frac{dX_t}{dt} = k_2(\Sigma X_e - X_t)^2, \tag{2.6}$$

Where k_2 is the rate constant of the pseudo second order adsorption ($g \cdot mg^{-1} \cdot min^{-1}$). For the boundary conditions t=0 to t=t_e and X_t=0 to X_t=ΣX_e, the integrated form of the equation becomes as follows (the integrated rate law for the pseudo second-order reaction):

$$\frac{1}{\Sigma X_e - X_t} = \frac{1}{\Sigma X_e} + k_2 t\,. \qquad (2.7)$$

The Particle Size Distribution

The particle size distribution of waste silica gel was measured by using a CILAS 1090 LD (France) grain-size analyser which features a sensitivity range from 0.04 to 500 μm. Water was used as the carrier liquid. The particles were dispersed with ultrasound for 2 min while the obscuration of particles in water reached 14%. The ultrasound duration during the measurement was 70 s. The standard operating procedure in use was the Fraunhöfer method.

Granulometric Analysis

The granulometric analysis of synthesis products was determined by using "L3P Sonic Sifter" fractional equipment. Sifting was conducted with a separation device whose performance is based on the principle of a vibrating air pole (dry separation), i.e. a vertical pulse or a shock wave every four seconds is transferred to sieves (425, 212, 106, 80 μm), in which, the easily together joined or agglomerated particles are dispersed and destroyed.

Thermal Stability

The thermal stability of the synthesized samples was estimated in a high-temperature furnace "SNOL 30/1300" in temperatures ranging from 600 to 1000 °C for 30 min.

The X-ray Powder Diffraction (XRD)

The XRD analysis of compounds was performed on a D8 Advance diffractometer (Bruker AXS, Karlsruhe, Germany) operating at the tube voltage of 40 kV and the tube current of 40 mA. The X-ray beam was filtered with a Ni 0.02 mm filter to select the CuKα wavelength. Diffraction patterns were recorded in Bragg-Brentano geometry by using a fast counting detector Bruker LynxEye based on the silicon strip technology. The specimens were scanned over the range of 3–70° (2 θ) at a scanning speed of 6° min^{-1} while employing the coupled two theta/theta scan type. The XRD data of gyrolite synthesized after 32–504 h and gyrolite with interfered Zn^{2+} ions was collected with a DRON–6 powder X-ray diffractometer with Bragg–Brentano geometry by using a Ni-filtered Cu K_α radiation and graphite monochromator operating under the voltage of 30 kV and the emission current of 20 mA. The step-scan covered the angular range of 2–60° (2 θ) in steps of 0.02°. Computer software X-fit was used for the diffraction profile refinement under the pseudoVoid function and for the description of the diffractional background under the 3rd degree Tchebyshev polynom (156).

X-ray Fluorescence Spectroscopy (XRF)

XRF was performed on a Bruker X-ray S8 Tiger WD spectrometer equipped with a Rh tube with the energy of up to 60 keV. Powder samples were measured in Helium atmosphere, and the data was analyzed with Spectra Plus Quant Express standard software.

Fourier Transform Infrared Spectroscopy (FT-IR)

FT-IR spectrum was recorded with the help of a Perkin Elmer FT–IR system Spectrum X spectrometer. The specimens were prepared by mixing 1 mg of the

sample in 200 mg of KBr. The spectral analysis was performed in the range of 4000–400 cm^{-1} with the spectral resolution of 1 cm^{1}.

Simultaneous Thermal Analysis (STA)

STA (differential scanning calorimetry–DSC and thermogravimetry–TG) was employed for measuring the thermal stability and phase transformation of samples. The tests were carried out by using two different apparatuses:

1) Netzsch instrument STA 409 PC Luxx whose parameters are as follows: a heating rate of 15 °C/min and the temperature range from 30 °C up to 1000 °C under air atmosphere. Ceramic sample handlers and crucibles of Pt-Rh were also used.

2) Linseis PT10 instrument whose parameters are as follows: a heating rate of 15 °C/min and the temperature range from 30 °C up to 575 °C under air atmosphere. Ceramic sample handlers and Al crucibles were also used.

***Scanning Electron Microscopy* (SEM)**

SEM (JEOL JSM-7600F, Japan) coupled with energy dispersive X-ray spectrometry (EDX) (Inca Energy 350, Oxford Instruments), Silicon Drift type detector X-Max20) was performed by using accelerating voltage of 10 kV, the working distance of 8.6 and 8.7 mm for SEM observation, and 200 s accumulation time for EDX analysis.

Atomic Absorption Spectrometry

The concentration of Ca^{2+} and Zn^{2+} ions was determined by using a Perkin Elmer Analyst 400 atomic absorption spectrometer with the following parameters: Zn^{2+} wavelength = 213.86 nm; Ca^{2+} wavelength = 422.67 nm; hollow cathode lamp current (I) = 30 mA; the type of flame was C_2H_2–air; oxidant air = 10 l/min; acetylene = 2.5 l/min. All the tests were repeated three times.

The Texture of the Synthesis Products

The surface area, the total pore volume and the pore size distribution of the synthesis products were performed by a BET surface area analyzer "KELVIN 1042 Sorptometer" (Costech Instruments). The specific surface area of gyrolite was calculated by employing the BET equation while using the data of the lower part of the N_2 adsorption isotherm ($0.05 < p/p_0 < 0.35$):

$$\frac{1}{X\left(\frac{p_0}{p}-1\right)} = \frac{C-1}{X_m C}\cdot\frac{p}{p_0} + \frac{1}{X_m C}, \qquad (2.8)$$

Where X is the mass of the adsorbate (adsorbed on the sample at relative pressure p/p_0), p is the partial pressure of adsorbate, p_0 is the saturated vapor pressure of the adsorbate, X_m is the mass of adsorbate (adsorbed at a coverage of one monolayer), C is a constant which is a function of the heat of the adsorbate condensation and the heat of adsorption (C_{BET} is a constant).

BET equation yields a straight line when $1/X[(p_0/p) - 1]$ is plotted versus p/p_0. The slope of $(C - 1)/X_mC$ and the intercept of $1/X_mC$ was used to determine X_m and C:S = slope = $(C - 1)/X_mC$ and I = intercept = $1/X_mC$. Solving for X_m yields $X_m = 1/(S + I)$. BET plot is usually found to be linear in the range of p/p_0 = 0.05–0.35. The total surface area of sample S_t was determined by equation $S_t = X_mNA_{cs}/M$, where M is the molecular mass of the adsorbate, N the Avogadro constant, A_{cs} is the cross-sectional area occupied by each nitrogen molecule ($16.2\cdot10^{-20}$ m^2). The

specific surface area was given by equation $S_{BET} = S_t/m$, where m is the mass of the synthesized product sample.

The total pore volume and the pore size distribution were calculated according to the corrected Kelvin equation and Orr *et al*.-developed scheme (157) while using the entire N_2 desorption isotherm at 77 K. The Kelvin equation relates the adsorbate vapor pressure depression to the radius of a capillary which has been filled with adsorbate:

$$ln\frac{p}{p_0} = -2\frac{\gamma V_m \cos\theta}{RTr_k}, \tag{2.9}$$

Where p is the saturated vapor pressure in equilibrium with the adsorbate condensed in a capillary or a pore, p_0 the normal adsorbate saturated vapor pressure, γ is the surface tension of nitrogen at its boiling point (γ = 8.85 ergs/cm^2 at (-195.8 °C)), V_m is the molar volume of liquid nitrogen (V_m = 34.7 cm^3), θ is the wetting angle (usually taken at 0° and cos θ = 1), R is the gas constant ($R = 8.134 \cdot 10^7$ ergs deg^{-1} mol^{-1}), T is the absolute temperature (T = 77 °K) and r_K is the Kelvin radius of a pore.

Thermodynamic Calculations

For the thermodynamic calculations of the hypothetical reaction parameters, the values of enthalpy $\Delta H_{298}^{0,f}$, entropy $\Delta S_{298}^{0,f}$ and molar specific heat capacities (C_p) of the formed compounds are applied and given in Table A1 (see Appendix 1). For the estimations, we used a method of absolute entropies, according to which, the change standard free Gibbs energy of reaction $\Delta_r G_T^0$ can be calculated with the following equation:

$$\Delta_r G_T^0 = \Delta_r H_T^0 - T\Delta_r S_T^0, \tag{2.10}$$

Where $\Delta_r H_T^0$ and $\Delta_r S_T^0$ are the change/alteration/variation of the reaction enthalpy and entropy at temperature T. The change of enthalpy and entropy for the reaction can be calculated form the following equations:

$$\Delta_r H_T^0 = \Delta_r H_{298}^0 + \Delta C_p (T_1 - 298), \tag{2.11}$$

$$\Delta_r S_T^0 = \Delta_r S_{298}^0 + \Delta C_p \left(\frac{T_1}{298}\right), \tag{2.12}$$

Where $\Delta_r H_{298}^0$ is the change of the standard enthalpy of the reactions, J/mol; $\Delta_r S_{298}^0$ is the standard entropy change of the reactions, J/mol; and $\Delta_r a, \Delta_r b, \Delta_r c, and\ \Delta_r c'$ are the constants of heat capacity dependence on temperature.

In the integral form, it can be written as follows:

$$\Delta_r H_T^0 = \Delta_r H_{298}^0 + \Delta a(T - 298) + \frac{\Delta b(T^2 - 298^2)}{2} + \frac{\Delta c(T^3 - 298^3)}{3} - \Delta c'\left(\frac{1}{T} - \frac{1}{298}\right), \tag{2.13}$$

$$\Delta_r S_T^0 = T\left[\Delta_r S_{298}^0 + \Delta a \ln\frac{T}{298} + \Delta b(T-298) + \frac{\Delta c(T^2 - 298^2)}{2} - \frac{\Delta c'}{2}\left(\frac{1}{T^2} - \frac{1}{298^2}\right)\right],$$

(2.14)

The standard molar thermodynamic properties values at 298 °K and 1 bar (Table A1) were taken from scholarly literature (Babushkin *et al*., Thermodynamics of Silicates, 1985).

3. Results and Discussions

3.1 Neutralization and Removal of Compounds Containing Fluoride Ions from AlF_3 Production Waste

The industry of aluminum fluoride generates a large amount of silica gel contaminated with F^- ions as a by-product which is not widely used or processed but is instead stored in landfill sites. Several methods have been developed to remove fluoride ions: adsorption and biosorption, ion exchange, chemical precipitation including electrocoagulation/flotation, membrane filtration, electrodialysis, and nanofiltration (158–162). Most methods for removing fluoride have drawbacks including high initial cost, lack of selectivity, low capacity, and difficulty in operation or regeneration. Besides, there is lack of information about the fluoride ions removal from solid; therefore, new methods for the removal of such waste are required.

3.1.1 Chemical and Mineralogical Composition of AlF_3 Production Waste

Firstly, before starting experiments, the chemical and mineralogical composition of AlF_3 production waste was determined by using two methods: chemical analysis and XRF. In the first stage of the investigation, the chemical analysis of aluminum fluoride production waste – silica gel (dried for 7 days at room temperature (20–25 °C) – in the laboratory and an additional 48 hours at 50 °C in the dryer) was performed. It was established that AlF_3 production waste consists of 77.67% silicon dioxide, 8.82% F^-, and 4.08% Al_2O_3 (see Table 3.1). These results were in a good agreement with the data of XRF analysis (see Table 3.1). In addition, the thermogravimetric analysis showed that the above mentioned sample lost 9.56 wt. % of mass at 30–1000 °C temperatures (see Table 3.1).

Table 3.1. Chemical composition of AlF_3 production waste

Parameter	Quantity, wt. %		Average quantity, wt. %
	XRF analysis	Chemical analysis	
SiO_2	77.77	77.57	77.67
F^-	-	8.82	8.82
Al_2O_3	4.03	4.12	4.08
Mass loss			9.56

XRD analysis data showed that the main compound containing fluoride ions in AlF_3 production waste is $AlF_3 \cdot 3H_2O$ (*d*-spacing: 0.545, 0.386, 0.329, 0.244 nm) (Figure 3.1., a). Furthermore, silicon dioxide is amorphous because a broad peak in the angle of diffraction that varied from 18 to 26° was observed. The diffraction maximums of compounds containing other aluminum components (due to a small quantity) were not identified on the XRD pattern.

These results were confirmed by FT-IR data: absorption bands at 1107, 930, and 802 cm^{-1} are characteristic of valence Si–O bond vibrations and are typical for silica (Figure 3.1., b). A sharp absorption band near the 467 cm^{-1} frequency range is characteristic of the deformation vibration of Si–O–Si. Moreover, in the FT-IR spectrum, the absorption band found at 3664 cm^{-1} and the broad absorption band

found at 3398 cm^{-1} describe the vibrations of hydroxyl groups connected to each other by hydrogen bonds. The deformation vibration of crystallization water is characterized by an absorption band at 1649 cm^{-1}. In addition, the absorption band at 565 $cm^{-1}$was assigned to the F–Al–F vibrations and confirmed the presence of fluoride ions in waste silica gel.

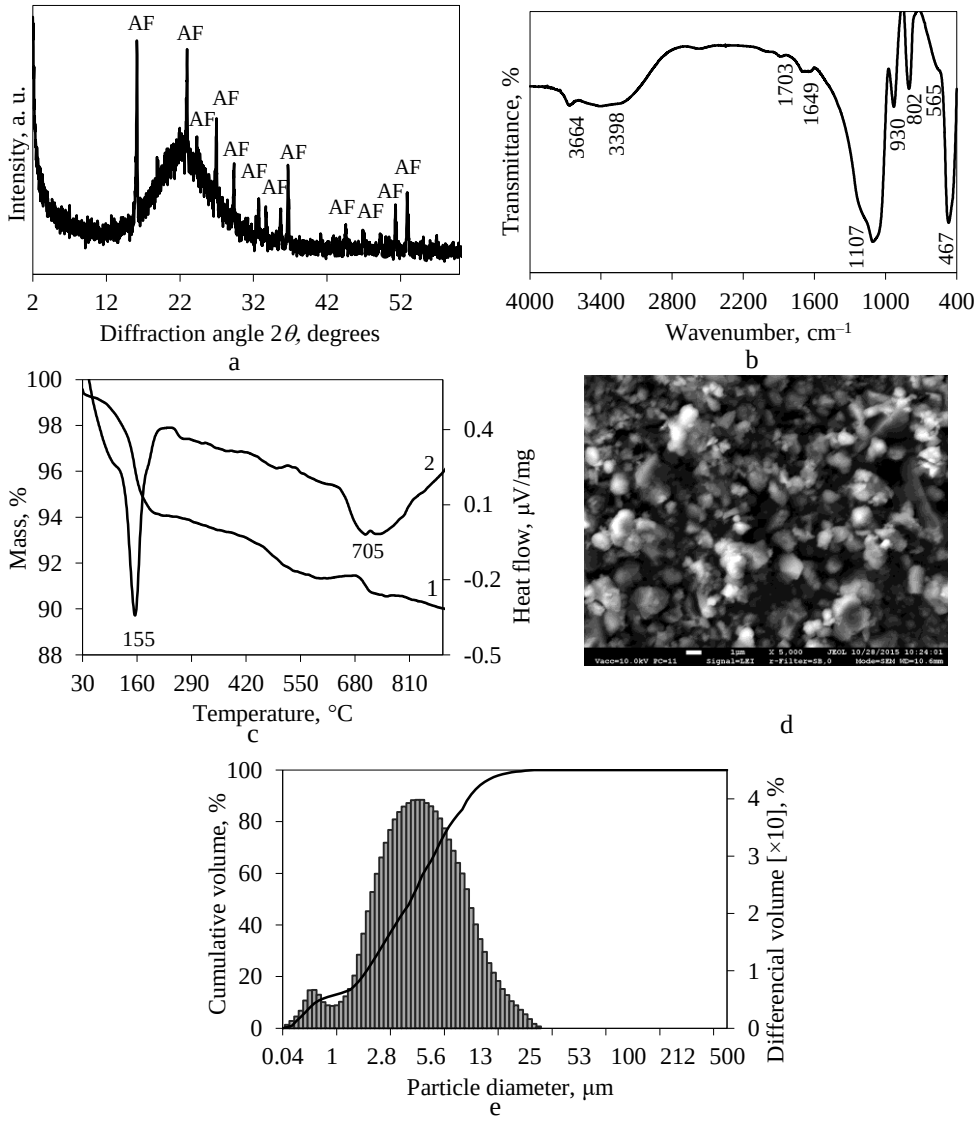

Figure 3.1. XRD pattern (a), FT-IR spectrum (b), STA curves (1 – TGA curve; 2 – DSC curve) (c), SEM micrograph (d), and particle size distribution (e) of AlF_3 production waste. Index: AF – $AlF_3 \cdot 3H_2O$.

In the DSC curve, a significant endothermic peak observed at 155 °C temperature was mainly due to the removal of crystallization water from the $AlF_3 \cdot 3H_2O$ structure (Figure 3.1., c). During this process, the AlF_3 production waste

sample mass loss was about 5.50 wt. %. The stoichiometric calculations of $AlF_3 \cdot 3H_2O$ show that only 5.8% of fluoride ions are combined into the structure, and the remaining amount of them are adsorbed by the amorphous $SiO_2 \cdot nH_2O$. The removal of the crystallization water in the AlF_3 production waste structure occurs at higher thermal treatment temperatures. The blurred endothermic effect was identified at 705 °C, which characterizes the aluminum trifluoride phase transition (α–; β–).

In the SEM micrograph, an amorphous mass of $SiO_2 \cdot nH_2O$ and tetragonal crystals of $AlF_3 \cdot 3H_2O$ with a size of 2.5–3 μm × 4–8 μm are observed (Figure 3.1., d). According to the results of the particle size distribution analysis, the diameter of the AlF_3 production waste particles varied between 0.04 to 25 μm (Figure 3.1., e). In addition, the fraction with the particle size of 2–13 μm, is predominant in this waste.

In the next stage of investigation, the possibility of F^- ion elution from AlF_3 production waste to a liquid medium was examined.

3.1.2 The Elution of F^- Ions from AlF_3 Production Waste

The water-soluble fluoride compounds presented on the AlF_3 production waste surface could be removed by using hot water. Extraction with hot water promotes the release of hydrogen fluoride and the reconstruction of active silanolgroups on the surface of waste silica gel:

$$\equiv Si - F + H_2O \rightarrow \equiv Si - OH + HF\ , \qquad (3.1)$$

Temperature has a significant effect on the efficiency of fluoride removal (163). For this reason, the elution of F^- ions from waste silica gel to the liquid medium within the temperature range from 25 to 95 °C was performed.

It was obtained that the mineralogical composition of AlF_3 production waste slightly varies during elution at 25 °C for 1 h when the ratio of w/s = 10 (Figure 3.2., curve 1). It was ascertained that the increase of the temperature positively affects the decomposition of $AlF_3 \cdot 3H_2O$ as the intensities of this compound's diffraction peaks decreased by 1.5 times when the process temperature was equal to 95 °C (Figure 3.2., curve 4). Meanwhile, the data for the chemical analysis of the liquid medium showed that the amount of F^- ions remained approximately the same: ~0.02 wt. % in the temperature range from 25 to 95 °C (Table 3.2.). Therefore, in order to completely destroy the structure of the above mentioned compound, the ratio of the liquid medium to AlF_3 production waste was increased to 500. In this case, all the crystalline structure compounds were decomposed (Figure 3.2., curve 5). The only visible item is a broad peak typical of amorphous SiO_2 at the angle of diffraction that varied from 18 to 26° on the XRD curve. Moreover, unexpected results were obtained after the chemical analysis of the liquid medium: although $AlF_3 \cdot 3H_2O$ decomposes, the released amount of F^- ions into the medium is only equal to 0.5 – 0.6 wt. % (Table 3.2.). It should be noted that the negligible decrease of F^-ion concentration can be explained by the strong adsorption properties of the AlF_3 production waste when the temperature of liquid medium was increased (Table 3.2.). This fact was confirmed by the slight increase of the liquid medium pH value.

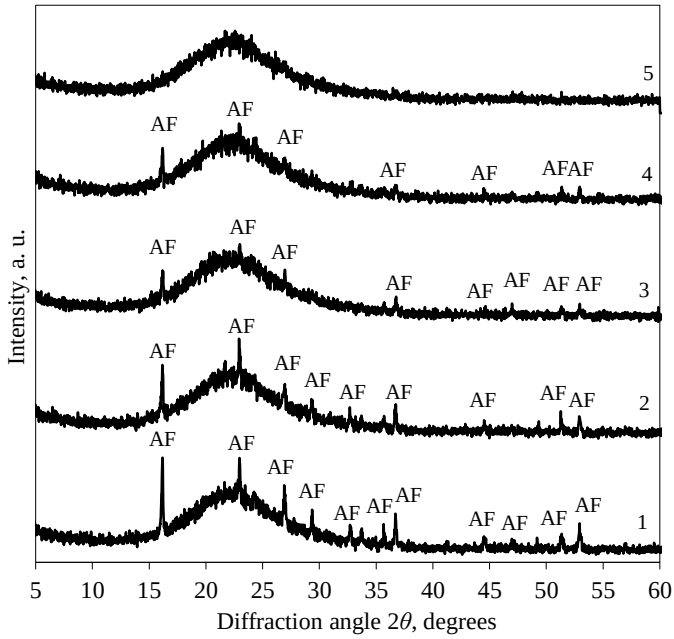

Figure 3.2. XRD patterns of AlF_3 production waste when w/s ratio was equal to 10 (curves 1–4) and 500 (curve 5) after 1 h treatment in different temperatures, °C: 1 and 5 at 25; 2 at 50; 3 at 75; 4 at 95. Index: AF – $AlF_3 \cdot 3H_2O$.

Table 3.2. Concentration of F^- ions and pH values of the liquid medium after 1 h elution at different temperatures with w/s at 10 or 500

Temperature, °C	F^- ions concentration·10^{-2} in the liquid medium, wt. %		pH		F^- ions concentration in the AlF_3 production waste, wt. %	
	w/s = 10	w/s = 500	w/s = 10	w/s = 500	w/s = 10	w/s = 500
25	2.4	61.3	2.80	5.15	8.62	8.03
50	2.3	59.7	2.84	5.32	8.62	8.04
75	2.1	53.3	2.89	5.38	8.62	8.11
95	2.0	52.5	2.90	5.76	8.62	8.12

In order to increase the pH value of the liquid medium and to destruct the structure of $AlF_3 \cdot 3H_2O$, additives, such as NaX zeolite, opoka and limestone (which contain 1 mm diameter particles (w/s = 250 at 25 °C temperature)) were used.

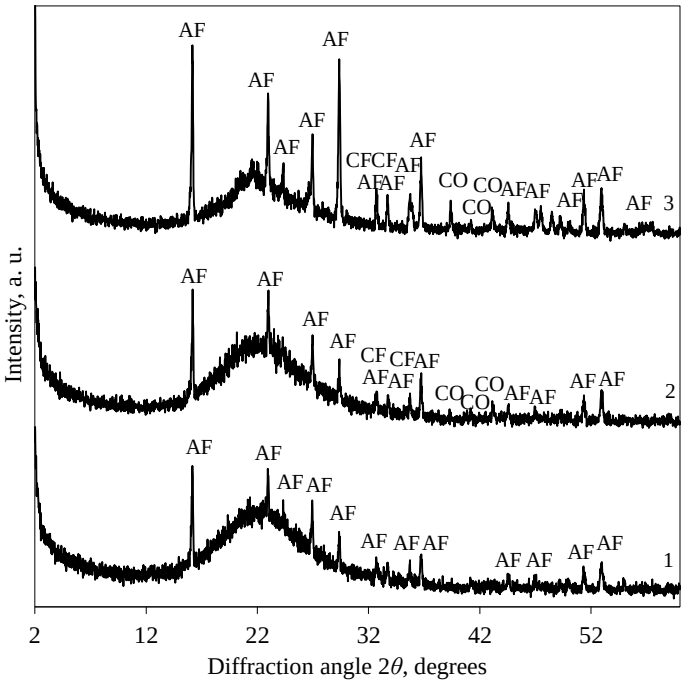

Figure 3.3. XRD patterns of AlF_3 production waste after interaction with: 1– NaX zeolite; 2 – limestone; 3 – opoka. Indexes: AF – $AlF_3 \cdot 3H_2O$; CF – CaF_2; CO – CaO.

XRD analysis data showed that after the interaction with NaX, the structure of AlF_3 production waste does not change because the diffraction peaks of $AlF_3 \cdot 3H_2O$ were identified (Figure 3.3., curve 1). Meanwhile, after the interaction with limestone and opoka, higher intensity peaks of $AlF_3 \cdot 3H_2O$ and small peaks of CaF_2 and CaO were observed in the XRD patterns (Figure 3.3., curves 2 and 3). Thus the results of XRD analysis showed that natural minerals do not have influence on the stability of aluminum trifluoride trihydrate.

When summarizing the above mentioned results, it can be stated that fluoride ions removal into the liquid medium depends on such factors as dissociation, solubility, w/s ratio and adsorption properties of the AlF_3 production waste. In order to reduce the adsorption properties of the AlF_3 production waste and the mobility of F^- ions, in the next stage of the experiment, mechanical activation was used.

3.1.3 The effect of Mechanical Activation on the Mobility of F^- in the AlF_3 Production Waste Samples

Mechanical activation was successfully applied in order to disturb the structure of phosphogypsum crystals and to improve their binding properties (164, 165). The phenomenon of activation occurs when, during the destruction of gypsum crystals, the impurities of acid solutions, which block the hydration process, are removed. The activation by disintegrator takes only several seconds; that is, the activation takes only the time until the activated material reaches the outlet. Agglomerates of

material particles are destroyed by the very intense force of the impact (164, 165). In this research, mechanical activation was used to decompose the structure of $AlF_3 \cdot 3H_2O$ and to reduce the adsorption properties of amorphous SiO_2.

Mechanical activation of silica gel was carried out using the DEZI-14 disintegrator, which works on the principle of the impact by employing the centrifugal force. The rotation speed of the activation discs was 1500 rotations per minute. The duration of the mechanical activation of the sample was a few seconds. Firstly, the experiment was performed by using only raw AlF_3 production waste, later on, additional quantity of water was supplied when the water-to-solid ratios were equal to 10 and 30.

It was determined that, after mechanical activation, the structure of $AlF_3 \cdot 3H_2O$ did not change: XRD patterns show intensive diffraction peaks typical of the mentioned compound (Figure 3.4., curves 1–3).

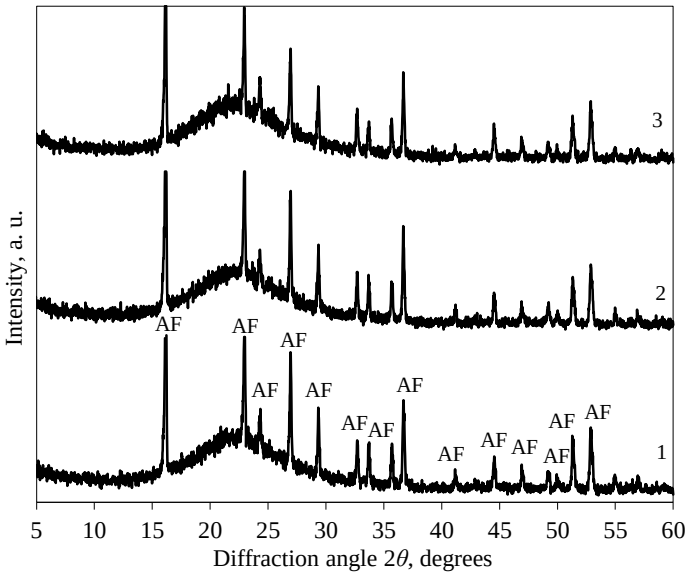

Figure 3.4. XRD patterns of mechanically activated waste silica gel: 1 is for raw material; 2 for w/s = 10; 3 for w/s = 30. Index: AF represents $AlF_3 \cdot 3H_2O$.

Chemical analysis the data of AlF_3 production waste showed that the concentration of fluoride ions in the liquid medium increased slightly because, when the w/s ratio was equal to 10, the concentration of fluoride ions was equal to 0.0072 wt. %, and, by increasing the w/s ratio 3 times (w/s = 30), it reached 0.0529 wt. % (see Table 3.3.). Meanwhile, pH of the liquid medium maintains a highly acidic value and equals to 2.835. One of the main reasons is the extremely short-term interaction during the mechanical activation; thus the mineralogical composition of the AlF_3 production waste sample remained stable (Figure 3.4.).

Table 3.3. Concentration of F^- ions in the liquid phase after mechanical activation

Sample	F^- (wt. %)	pH
Raw material	0.0018	1.482
Activated silica gel, w/s = 10	0.0072	2.130
Activated silica gel, w/s = 30	0.0529	2.835

It should be noted that the higher w/s ratio during activation by the disintegrating process was due to the principle of the operation (i.e. the level of the impact force of the particles is reduced) is impossible and economically useless/pointless. Therefore, in the next stage of the research, in order to decrease the mobility of fluoride ions, the alkaline additive was used.

3.1.4 The Effect of Alkaline Additive on the Mobility of F^- Ion in the AlF_3 Production Waste

Precipitation reactions are often used to remove F^- ions from wastewater because of the formation of CaF_2 precipitate. In order to reduce the F^-ion mobility in the AlF_3 production waste, in elution experiments, different amounts of CaO additive (6.5, 10, 20 wt. %) were used at 25 °C for 1 h when the ratio of w/s = 10 and 500. The amount of 6.5 wt. % CaO additive was used because, according to stoichiometric calculations, it is a sufficient amount of Ca^{2+} ions to bind all the F^- ions in the AlF_3 production waste. Afterwards, the amount of the additive was increased to 10% and 20% in order to bind all the F^- ions into a stable compound.

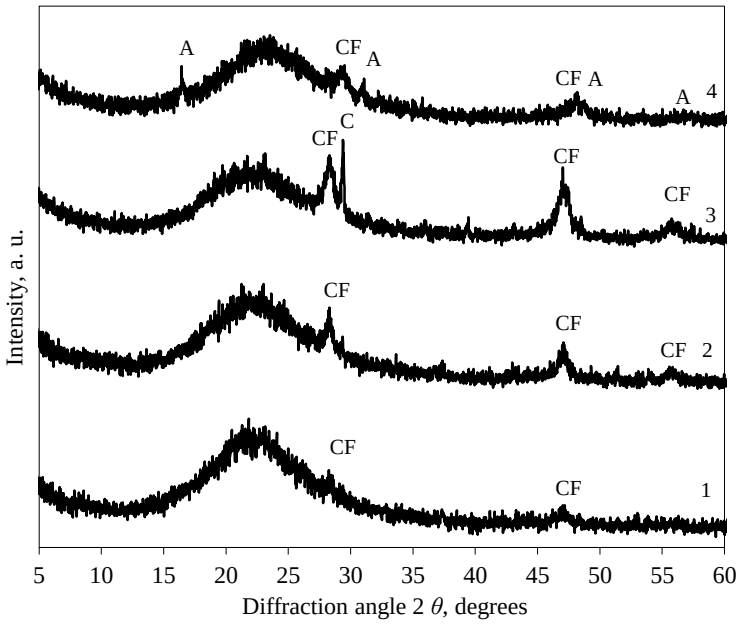

Figure 3.5. XRD patterns of AlF_3 production waste after interaction with CaO additive at 25 °C at a w/s ratio of 500 (1–3) and of 10 (4) and at the following CaO content (wt. %): 1 at 4–6.5%; 2 at 10%; 3 at 20%. Indexes: A represents $Al_2(OH)_{2.76}F_{3.24}\cdot H_2O$; CF denotes CaF_2; C stands for $CaCO_3$.

It was determined that CaO stimulates the formation of CaF_2 because low-intensity peaks of the latter compound were observed (Figure 3.5., curve 1). Also, the concentration of F^- ions in the liquid medium decreased to 0.19 wt. % (see Table 3.4.). Therefore, by adding a larger amount of CaO additive (10 wt. %, 20 wt. %) into waste silica gel samples, the intensities of the CaF_2 diffraction peaks noticeably increased (Figure 3.5., curves 2, 3).

In addition, the concentration of F^- ions in the liquid medium decreased almost 3 times, i.e. to 0.06 wt. % (Table 3.4.). One of the main reasons of this phenomenon may be the formation of CaF_2 and/or the reduction of SiO_2 adsorption properties in the alkaline medium (pH = 10.81). In addition, in samples with 20 wt. % of the CaO additive, the formation of calcite (*d*-spacing: 0.304 nm) was observed (Figure 3.5., curve 3).

Table 3.4. Concentration of F^- ions and pH values of the liquid medium after 1 h of interaction of AlF_3 production waste with CaO additive at 25 °C when w/s = 500

CaO additive, wt. %	F^- ions concentration in the liquid medium, wt. %	pH
6.5	0.19	7.07
10	0.17	8.81
20	0.06	10.81

It should be noted that the elution of F^- ions from the AlF_3 production waste and the CaO sample was not effective when the ratio of water-to-solid was equal to 10: the concentration of F^- ions in the liquid medium was higher, and the typical diffraction peaks of $Al_2(OH)_{2.76}F_{3.24}\cdot H_2O$ together with CaF_2 were identified in the XRD curve (Figure 3.5., curve 4).

However, a small amount (0.06–0.2 wt. %) of fluorine ions still remained in the liquid medium under all the experimental conditions. Besides, it was discovered that the CaO additive exerts a positive influence on the decomposition of $AlF_3\cdot 3H_2O$ and on the formation of CaF_2. For this reason, during the next experimental stage, the application of AlF_3 production waste to the formation of a low-base calcium silicate hydrate under hydrothermal synthesis conditions was performed.

3.1.5 Application of AlF_3 Production Waste to the Synthesis of Low-Base Calcium Silicate Hydrates

Hydrothermal synthesis includes various techniques of crystallizing substances from high-temperature aqueous solutions at high vapor pressures. It is presumed that, during hydrothermal synthesis, F^- ions in the AlF_3 production waste will be combined into a stable compound, calcium fluoride, and this material could be used in binders and in the building materials industry. Only fragmentary data on the removal of fluoride ions from the solid materials and waste of limited solubility during hydrothermal synthesis has so far been published in academic literature (166). For this reason, the influence of silica containing compounds (pure SiO_2 and

AlF_3 production waste) as well as molar C/S (0.55, 0.66, 0.83, and 1.0) ratios of the primary mixtures on the formation of calcium silicate hydrates were estimated.

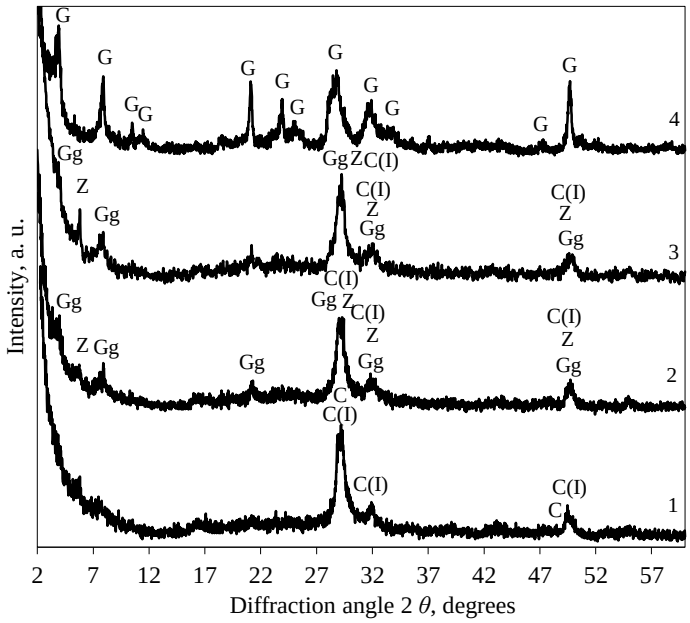

Figure 3.6. XRD patterns of hydrothermal synthesis products after different isothermal treatment at 200 °C of mixtures with amorphous silica oxide, when C/S molar ratio 0.55: 1 at 8 h; 2 at 16 h; 3 at 24 h; 4 at 72 h. Indexes: G denotes gyrolite; C(I) represents C-S-H(I); Z stands for Z-phase; Gg shows gyrolite gel; C depicts calcite.

It was determined that in the pure $CaO–SiO_2–H_2O$ system, when the molar ratio of CaO/SiO_2 = 0.55, after 8 h of isothermal curing at 200 °C, semi-crystalline calcium silicate hydrate C-S-H(I) (*d* being at 0.304, 0.278, 0.183 nm) was formed (Figure 3.6., curve 1). By prolonging the duration of isothermal curing to 16 h, a low-base calcium silicate hydrate Z-phase (*d* being at 0.155, 0.419, 0.382, 0.304, 0.183 nm) was formed together with gyrolite gel (*d*-spacing: 2.312; 1.138; 0.839; 0.421; 0.280; 0.221 nm), and these compounds remained stable until 24 h (Figure 3.6, curve 2). The above listed compounds fully recrystallized into gyrolite (*d*-spacing: 2.273; 1.126; 0.844; 0.420; 0.365; 0.280; 0.224 nm) (Figure 3.6., curve 4) after 48 h (Appendix 4, Figure A4.1., curve 1) of synthesis.

Moreover, carbonation was observed when the products were dried in an air-conditioned chamber (50 ºC, 24 h) because the diffraction peaks characteristic to calcium carbonate (PDF 04-012-0489; *d*-spacing at 0.304; 0.191 nm) were detected in the XRD pattern after 8 h of synthesis (Figure 3.6., curve 1).

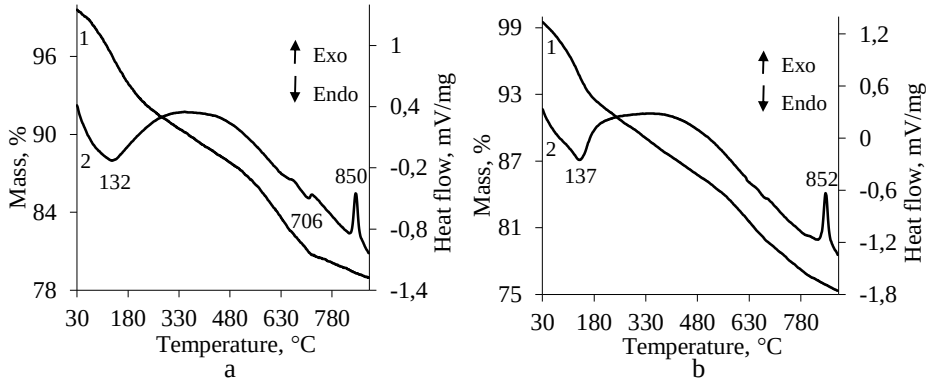

Figure 3.7. STA (1 – TGA curve; 2 – DSC curve) curves of hydrothermal synthesis products after different isothermal treatment at 200 °C of mixtures with amorphous silica oxide, when C/S molar ratio stands at 0.55: *a* at 8 h; *b* at 72 h.

The previous results were confirmed by STA analysis data. It was determined that the endothermic effect at ~132–137 °C can be attributed to the dehydration of calcium silicate hydrates (Figure 3.7., a, b, curve 2). The exothermic effects at 850 °C and 852 °C were assigned to semi-crystalline C-S-H(I) and gyrolite recrystallization into wollastonite, respectively (Figure 3.7., a and b, curve 2). It should be underlined that the heat of the above mentioned reaction increases from 27.36 J/g to 39.77 J/g by increasing the duration of synthesis (Figure 3.7., curve 2). Furthermore, the endothermic effect at ~706 °C can be assigned to the decomposition of calcium carbonate (Figure 3.7., a, curve 2).

Thus the sequence of compounds which formed in a $CaO\text{-}SiO_2\text{-}H_2O$ system with the C/S = 0.55 molar ratio looks as follows:

$$CaO + SiO_2 \cdot nH_2O + H_2O \xrightarrow{8\,h} \left| \begin{matrix} CaCO_3{}^{*} \\ C\text{-}S\text{-}H(I) \end{matrix} \right. \xrightarrow{16h} \left| \begin{matrix} Z-phase \\ C\text{-}S\text{-}H(I) \\ gyrolite gel \end{matrix} \right. \xrightarrow{72\,h} gyrolite$$

* – calcite formed during the drying process of synthesis products.

It was determined that in $CaO–AlF_3$ production waste $–H_2O$ system when the molar ratio of CaO/SiO_2 = 0.55, after 8 h of isothermal curing at 200 °C, the main synthesis product is a high-crystallinity low-base calcium silicate hydrate Z-phase, the stoichiometric composition of which corresponds to the molar ratio CaO/SiO_2 = 0.55 of the initial mixture (Figure 3.8., curve 1). In addition, the main compound in the waste silica gel containing F^- ions, i.e. $AlF_3 \cdot 3H_2O$ was unstable and decomposed. Thus the F^- ions actively interacted with calcium ions and formed calcium fluoride (*d* being at 0.315, 0.193, 0.165 nm), the structure of which is stable under hydrothermal synthesis conditions (Figure 3.8., curves 1–4). It should be noted that CaO also reacts with Al^{3+} ions during hydrothermal treatment and forms hydrogarnet ($Ca_3Al_2O_6(H_2O)_6$, PDF- 76-0557; *d* being at 0.513, 0.443, 0.336 nm), which also remained stable after the all synthesis conditions (Figure 3.8., curves 1–4). After 16 h of synthesis, Z-phase recrystallizes into gyrolite gel (Figure 3.4, a,

curve 3) which is not stable and transforms into gyrolite after 24 h (Figure 3.8., curves 2 and 3).

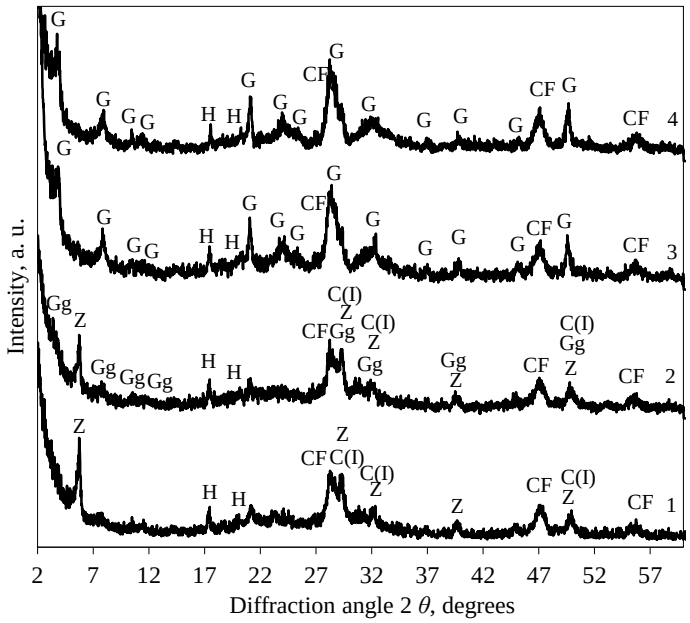

Figure 3.8. XRD patterns of hydrothermal synthesis products after different isothermal treatment at 200 °C of mixtures with AlF_3 production waste, when C/S molar ratio is 0.55: 1 at 8 h; 2 at 16 h; 3 at 24 h; 4 at 72 h. Indexes: G represents gyrolite; H shows hydrogarnet ($Ca_3Al_2O_6(H_2O)_6$); C(I) denotes C-S-H(I); CF depicts CaF_2; Z illustrates Z-phase; Gg stands for gyrolite gel.

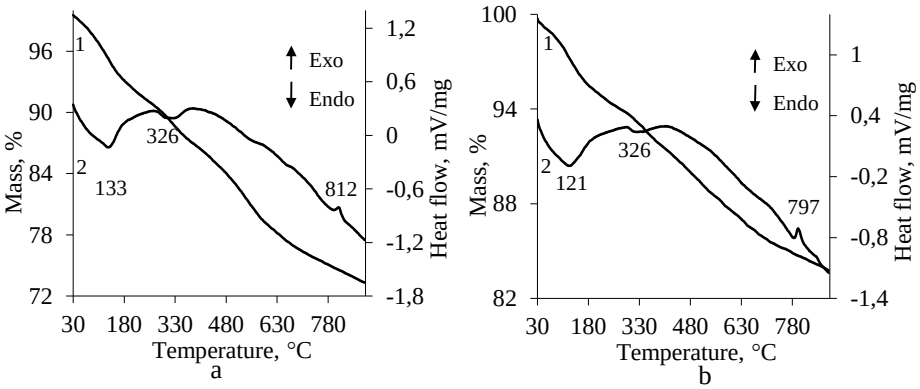

Figure 3.9. STA (1 – TGA curve; 2 – DSC curve) curves of hydrothermal synthesis products after different isothermal treatment at 200 °C of mixtures with AlF_3 production waste, when C/S molar ratio is 0.55: a at 8 h; b at 72 h.

In DSC curves, the endothermic peak which describes the dehydration process of hydrogarnet was identified at 326 °C temperature (Figure 3.9., a, b, curve 2). The

first broad endothermic peak at the temperatures of 133 °C and 121 °C is related to the loss of physisorbed and interlayer water from the crystal structure of the C-S-H. It should be noted that the modification of SiO_2 exerts influence on the C-S-H(I) and gyrolite recrystallization into wollastonite because, in the mixtures with waste silica gel, this process is accelerated and identified at 812 °C and 797 °C temperatures. Meanwhile, in the pure system, the above mentioned reaction proceeds at higher temperatures (~850 °C) (see Figure 3.7., a, b, curve 2).

The reactions of the new compounds formation in the $CaO–AlF_3$ production waste – the H_2O system, when C/S = 0.55 – occur in the following sequence:

$$CaO + AlF_3\ \text{production waste} + H_2O \xrightarrow{8\ h} \begin{matrix} Z-\text{phase} \\ C\text{-}S\text{-}H(I) \\ CaF_2 \\ \text{hydrogarnet} \end{matrix} \xrightarrow{16h} \begin{matrix} Z-\text{phase} \\ C\text{-}S\text{-}H(I) \\ \text{gyrolite gel} \\ CaF_2 \\ \text{hydrogarnet} \end{matrix} \xrightarrow{24-72\ h} \begin{matrix} \text{gyrolite} \\ CaF_2 \\ \text{hydrogarnet} \end{matrix}$$

It was established that by increasing the C/S molar ratio of the initial mixture to 0.66, the mineralogical composition of calcium silicate hydrates remained unchanged.

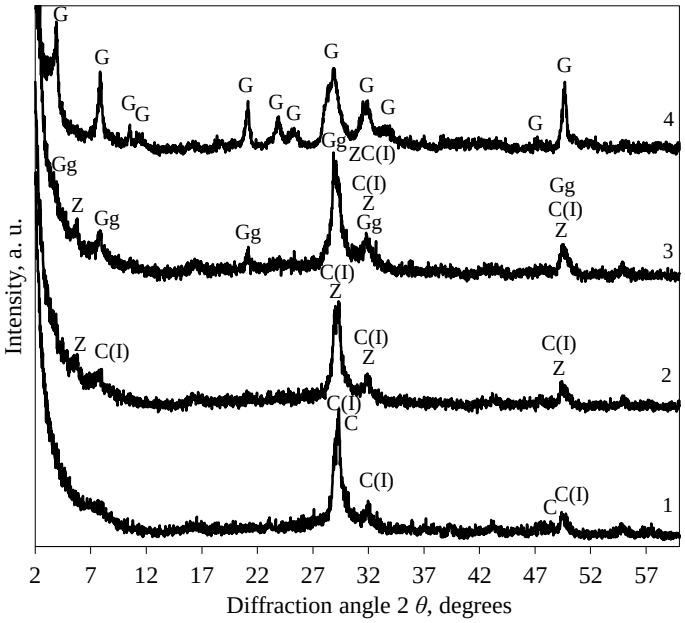

Figure 3.10. XRD patterns of hydrothermal synthesis products after different isothermal treatment at 200 °C of mixtures with amorphous silica oxide, when C/S molar ratio is equal to 0.66: 1 at 8 h; 2 at 16 h; 3 at 24 h; 4 at 72 h. Indexes: G represents gyrolite; Gg stands for gyrolite gel; C(I) denotes CSH(I); Z shows Z-phase.

It was determined that in a pure $CaO–SiO_2–H_2O$ mixture, after 8 h of isothermal treatment, the X-ray diffraction pattern shows basic reflections characteristic only to C-S-H(I) and calcite (Figure 3.10., curve 1). By prolonging the

duration of isothermal curing to 16 h, Z-phase was formed. After 24 h, the intensities of the gyrolite gel were observed together with Z-phase (Figure 3.10., curve 3). It was estimated that gyrolite gel fully recrystallizes into gyrolite after 48 h of synthesis (Appendix 4, Figure A4.1., curve 2) and remained stable until 72 h (Figure 3.10., curve 4). This data was confirmed by the results of STA analysis (Figure 3.11.).

Thus the sequence of compounds formed in the $CaO\text{-}SiO_2\text{-}H_2O$ system with the C/S = 0.66 molar ratio during the synthesis looks as follows:

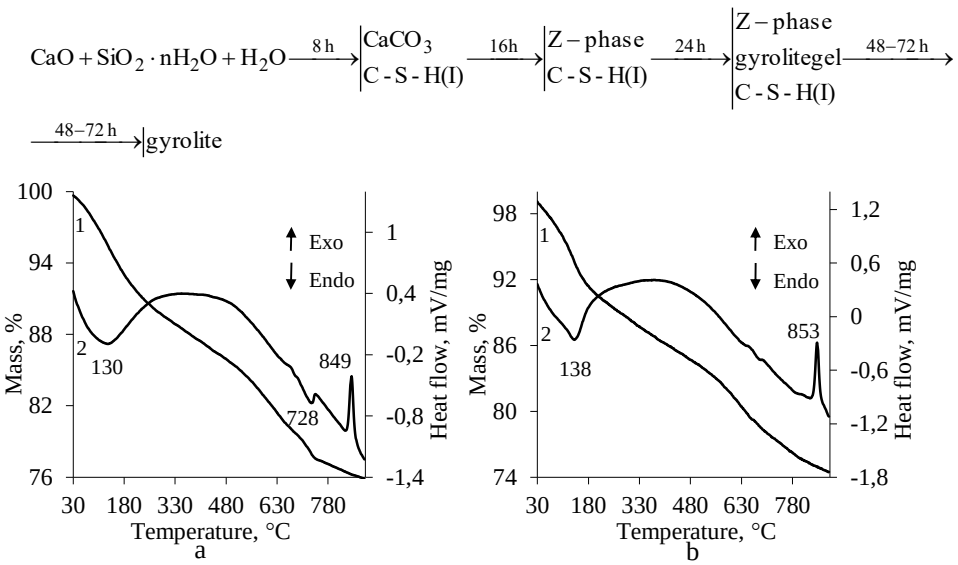

Figure 3.11. STA (1 shows the TGA curve; 2 depicts the DSC curve) curves of hydrothermal synthesis products after different isothermal treatment at 200 °C of mixtures with amorphous silica oxide when C/S molar ratio equals to 0.66: a at 8 h; b at 72 h.

The obtained results are supported by other authors' work. Baltakys and Siaučiūnas (94) determined that the optimal temperature of gyrolite synthesis is rather high (approximately 200 °C), and the duration is long (about 32 h) when amorphous silica is used as a SiO_2 component. These authors showed that gyrolite does not form even during a week in the mixtures of CaO and amorphous SiO_2 at 150 °C under saturated steam pressure. The increment of temperature positively affects gyrolite formation because this compound is produced at 175 °C after 72 h, and after 32 h at 200 °C. Besides, Eisinas in his PhD thesis noted that the formation of gyrolite proceeds via disordered intermediate phases: the initial C-S-H gel transforms to Z-phase and then finally recrystallizes to gyrolite (167).

It should be underlined that the mechanism of hydrothermal reactions and the sequence of the compounds formed in $CaO\text{-}AlF_3$ production waste $\text{-}H_2O$ mixtures are quite different when C/S = 0.66. It was found that after 8 h of isothermal curing gyrolite gel, Z-phase, C-S-H(I) and CaF_2 were formed (Figure 3.12., curve 1). Gyrolite already formed after 16 h of hydrothermal treatment, and this compound remained stable by prolonging the duration of synthesis until 72 h (Figure 3.12., curves 2–4). In this case, calcium fluoride and hydrogarnet were formed at the

beginning of the synthesis and remained stable (for 72 h) as in the mixtures with C/S = 0.55.

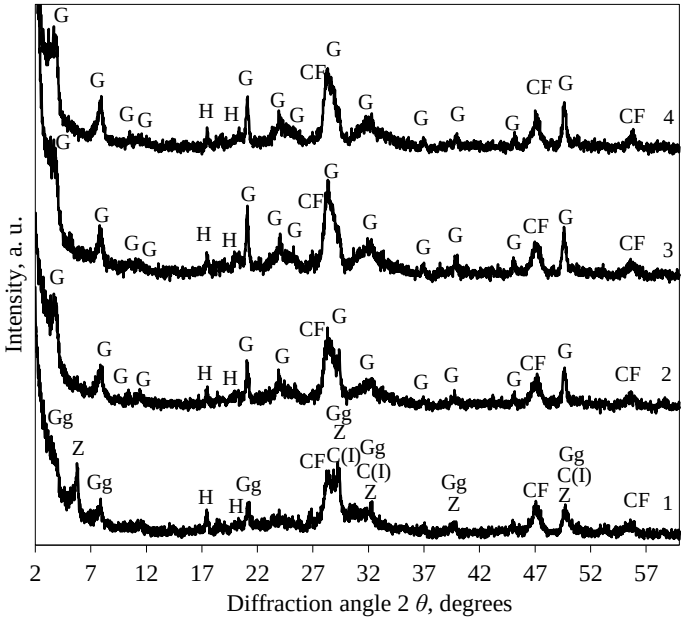

Figure 3.12. XRD patterns of hydrothermal synthesis products after different isothermal treatment at 200 °C of mixtures with AlF_3 production waste when C/S molar ratio equals 0.66: 1 at 8 h; 2 at 16 h; 3 at 24 h; 4 at 72 h. Indexes: G denotes gyrolite; H stands for hydrogarnet ($Ca_3Al_2O_6(H_2O)_6$); Gg represents gyrolite gel; C(I) depicts CSH(I); CF shows CaF_2; Z reflects Z-phase.

The above mentioned results were confirmed by STA analysis data which is in good agreement with the data of the C/S molar ratio equaling 0.55 (Figure 3.9. a, b). Four endothermic peaks are visible in the DSC curves at 325 °C and at 129 °C as well as at 123 °C temperatures which describe the dehydration processes of formed compounds and two exothermic effects at 820 °C and 804 °C; this indicates the recrystallization of the reaction products into wollastonite (Figure 3.13., a, b, curve 2).

The reactions of the new compounds formation in the CaO-AlF_3 production waste -H_2O system when C/S = 0.66 occur in the following sequence:

$$CaO + AlF_3\ \text{production waste} + H_2O \xrightarrow{8\ h} \begin{array}{l} Z-\text{phase} \\ C\text{-}S\text{-}H(I) \\ \text{gyrolite gel} \\ CaF_2 \\ \text{hydrogarnet} \end{array} \xrightarrow{16-72\ h} \begin{array}{l} \text{gyrolite} \\ CaF_2 \\ \text{hydrogarnet} \end{array}$$

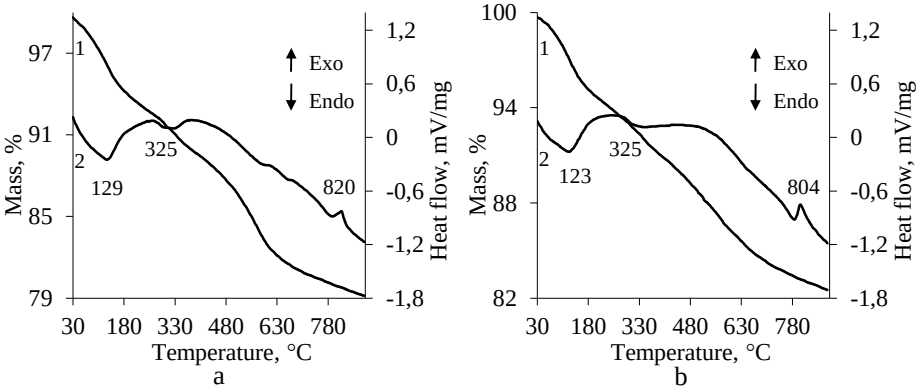

Figure 3.13. STA (1 is the TGA curve; 2 is the DSC curve) curves of hydrothermal synthesis products after different isothermal treatment at 200 °C of mixtures with AlF_3 production waste when C/S molar ratio equals to 0.66: a at 8 h; b at 72 h.

It was determined that by prolonging the synthesis duration from 8 h to 72 h when the sieve mesh diameter is less than < 80 μm, the particle size of the smallest fraction decreased: when CaO/SiO_2 = 0.55, it decreased by 1.5 times (Figure 3.14., a, curve 1); when CaO/SiO_2 = 0.66, it decreased by 1.2 times (Figure 3.14., a, curve 2). Meanwhile, when the sieve mesh diameter was 106 μm, the particle size increased about 1.2 times in both cases (Figure 3.14., b).

Thus granulometric analysis of synthesis products which were synthesized in the mixture with AlF_3 production waste showed that the silica-containing compound exerts influence not only on the mineralogical composition but also on the particle size distribution of the synthesis products.

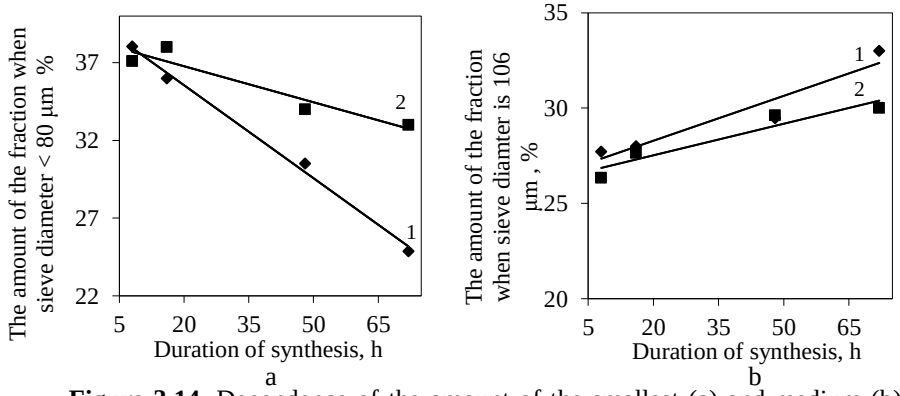

Figure 3.14. Dependence of the amount of the smallest (a) and medium (b) particle fractions of the synthesis products synthesized in the mixture with AlF_3 production waste on the duration of the synthesis process. Indexes: 1 denotes C/S = 0.55, 2 shows C/S = 0.66.

The data of the liquid medium analysis after the hydrothermal synthesis process showed that quantity of fluoride ions released into the liquid medium was very low (see Table 3.5.).

Table 3.5. Concentration (wt. %) of F^- ions in the liquid medium after the synthesis process.

Duration of synthesis, h	Concentration (wt. %) of F^- ions when CaO/SiO_2 molar ratio equals to	
	0.55	0.66
8	0.057	0.060
16	0.031	0.045
24	0.031	0.032
72	0.037	0.060

Thus it was established that AlF_3 production waste is a prospective raw material for the synthesis of low base calcium silicate hydrates because the kinetics of the compound formation is faster than the equivalent values in pure mixtures. Besides, during the hydrothermal synthesis, the F^- ions were not released into the liquid medium but instead combined into a stable compound, calcium fluoride.

In scientific work (132), the influence of the isothermal curing duration equalling to 168 h at 200 °C temperature on gyrolite structure characteristics was examined in detail. However, the effect of longer hydrothermal treatment duration on the gyrolite structure was not investigated. Therefore, in order to predict the application possibilities of the synthesized product, it is necessary to analyze and experimentally explain with thermodynamic calculations the gyrolite formation mechanism, the sequence of intermediate compounds formation as well as their stability temperature and duration intervals.

The theoretical hypothesis was supported with thermodynamic calculations. The recrystallization reactions of gyrolite which are possible during the hydrothermal synthesis at 200 °C are given below.

(1) Truscottite:

$2CaO{\cdot}3SiO_2{\cdot}2.5H_2O + 10H_2O \rightarrow 0.25(7CaO{\cdot}12SiO_2{\cdot}3H_2O) + 0.25Ca(OH)_2 + 11.5H_2O,$

(2) Xonotlite:

$2CaO{\cdot}3SiO_2{\cdot}2.5H_2O + 10H_2O \rightarrow 0.33(6CaO{\cdot}6SiO_2{\cdot}H_2O) + SiO_2 + 12.17H_2O,$

(3) 1.1 nm tobermorite:

$2CaO{\cdot}3SiO_2{\cdot}2.5H_2O + 10H_2O \rightarrow 0.4(5CaO{\cdot}6SiO_2{\cdot}5.5H_2O) + 0.6SiO_2 + 10.3H_2O,$

(4) Okenite:

$2CaO{\cdot}3SiO_2{\cdot}2.5H_2O + 10H_2O \rightarrow 1.5(CaO{\cdot}2SiO_2{\cdot}2H_2O) + 0.5Ca(OH)_2 + 9H_2O,$

(5) 1.4 nm tobermorite:

$2CaO{\cdot}3SiO_2{\cdot}2.5H_2O + 10H_2O \rightarrow 0.4(5CaO{\cdot}6SiO_2{\cdot}10.5H_2O) + 0.6SiO_2 + 8.3H_2O,$

(6) Z-phase:

$2CaO{\cdot}3SiO_2{\cdot}2.5H_2O + 10H_2O \rightarrow 1.5(CaO{\cdot}2SiO_2{\cdot}2H_2O) + 0.5Ca(OH)_2 + 9H_2O.$

The theoretical possibilities of truscottite (curve 1), xonotlite (curve 2), 1.1 nm tobermorite (curve 3), okenite (curve 4), 1.4 nm tobermorite (curve 5) and Z-phase (curve 6) formation reactions are given in the Figure 3.15 ($\Delta_r G_T^0 = f(T)$ plot) and in Table 3.6.

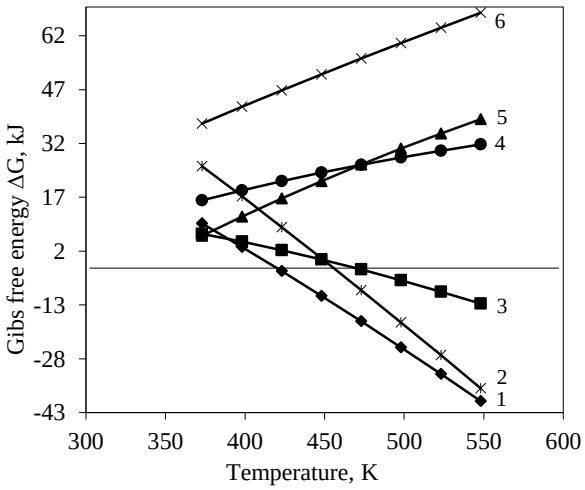

Figure 3.15. Gibbs free energy values as a function of temperature for truscottite (curve 1); xonotlite (curve 2); 1.1 nm tobermorite (curve 3); okenite (curve 4), 1.4 nm tobermorite (curve 5) and Z-phase (curve 6) formation reactions at 373–548 °K.

The thermodynamic parameters of reactions (Figure 3.15., Table 3.6.) showed that the negative values of $\Delta_r G_T^0$ would be reached only at higher than 423 °K temperatures for all the studied reactions. Moreover, by increasing the temperature, most likely, reactions 1 and 2 would occur; meanwhile, the thermodynamic possibility of reaction (3) is significantly lower even if the calculated $\Delta_r G_T^0$ values are negative. Thus it can be seen that during the hydrothermal treatment at 473 °K (200 °C) temperature, the greatest possibility is that gyrolite will transform into truscottite because the obtained Gibbs free energy value of this compound is the lowest one (ΔG = -39.8 kJ) (Figure 3.15., curve 1, and Table 3.6.). Reaction (2) could also influence the process; however, its thermodynamic possibility is lower than the first one's (ΔG = -36.2 kJ) (Figure 3.15., curve 2). It should be noted that the formation of Z-phase in such conditions is the least probable, and it still decreases with increasing temperature (ΔG = -79.1 kJ) (Figure 3.15, curve 6, and Table 3.6.).

Table 3.6. Thermodynamic data of reaction dependence on temperature for truscottite (1) and Z-phase (6) formation reactions at 373–548 °K

Reactions	T, K	373	398	423	448	473	498	523	548
1	$\Delta_r H_T^0$,kJ	105.1	108.4	111.7	115.1	118.3	121.6	124.9	128.2
	$\Delta_r S_T^0$,J	256.0	264.5	272.5	280.1	287.2	294.0	300.4	306.6
	$\Delta_r G_T^0$, kJ	9.6	3.1	-3.5	-10.4	-17.5	-24.7	-32.2	-39.8
2	$\Delta_r H_T^0$,kJ	149.9	152.5	154.9	157.4	159.9	162.5	165.0	167.5
	$\Delta_r S_T^0$,J	333.1	339.7	345.8	351.6	357.0	362.2	367.1	371.8

	$\Delta_r G_T^0$,kJ	25.7	17.2	8.7	-0.01	-8.8	-17.8	-26.9	-36.2
6	$\Delta_r H_T^0$,kJ	-32.4	-31.0	-29.6	-28.3	-26.9	-25.5	-24.2	-22.8
	$\Delta_r S_T^0$,J	-187.6	-184.0	-180.7	-177.6	-174.6	-171.8	-169.1	-166.6
	$\Delta_r G_T^0$,kJ	37.5	42.2	46.7	51.2	55.6	59.9	64.2	68.4

It was determined that, in the CaO and $SiO_2 \cdot nH_2O$ mixture after 120 h of hydrothermal treatment when the molar ratio of the initial mixture CaO/SiO_2 ~0.66, gyrolite (*d*-spacing: 2.273, 1.126, 0.844, 0.420, 0.365, 0.280, and 0.224 nm) formed as the final product of the synthesis (Figure 3.16., curve 1). By extending the treatment duration to 168 h, the intensity of the main diffraction peak (*d* ~2.273) and the crystallite size of the above mentioned compound increased from 112.6 to 130.6 a.u. (Table 3.7.) as well as from 46.2 nm to 55.3 nm, respectively (Figure 3.17., b).

Meanwhile, after extending the duration of isothermal curing to 336 h, gyrolite became metastable because the traces of a new compound of calcium silicate hydrate – truscottite (*d*-spacing: 1.880, 0.942, 0.769, 0.471, 0.314, 0.183, and 0.176 nm) – were formed (Figure 3.16., curve 3). The visible changes in the main diffraction peak (*d* ~2.273) of gyrolite can be seen in Figure 3.17., a, because a doublet peak with the *d*-spacing of 2.2047 nm and the *d*-spacing of 2.030 nm formed in the range of 3–5° diffraction angles (Figure 3.17., a, curves 2, 3).

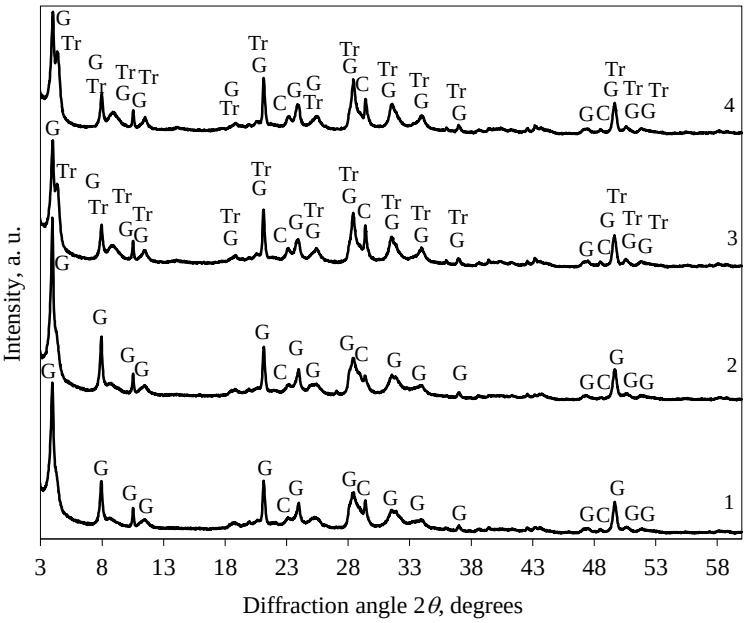

Figure 3.16. X-ray diffraction patterns of synthesis products in the mixtures with amorphous silica for varying durations of hydrothermal treatment at 200 °C, in h: 1 at 120; 2 at 168; 3 at 336; 4 at 504. Indexes: G represents gyrolite, Tr shows truscottite, C represents calcite. All the curves were corrected with X-fit software.

On the other hand, the intensity of the gyrolite diffraction peak significantly decreased (to 94.55 a. u.). Meanwhile, the peak intensities of truscottite remained the same (~ 62 a. u.) till 504 h (Table 3.7.). At the same time, the crystallite size of gyrolite decreased from 56.1 nm to 52.3 nm, whereas the crystallite size of truscottite increased from 45.5 to 50.2 nm (Figure 3.17., b).

Table 3.7. The intensities of the main gyrolite *d*-spacing (2.273 nm) and truscottite *d*-spacing (2.040 nm) diffraction peaks

Duration of synthesis, h	Peak intensity of gyrolite $\cdot 10^2$, a. u.	Peak intensity of truscottite $\cdot 10^2$, a.u.
120	112.6	-
168	130.6	-
336	94.6	62.5
504	91.5	62.9

The presented results are only in a partial agreement with the data of Flint *et al*. obtained in 1938, which indicated that, after 6–42 days of hydrothermal treatment at 150–350 °C temperatures, the only product – gyrolite – forms when C/S changes from 0.5 to 0.66. Meanwhile, Mackay and Taylor in 1953 synthesized this compound at 150 °C within 76 days of isothermal treatment. Later on, K. Garbev synthesized gyrolite from C-S-H gel with C/S=0.66 after 10 days at 200 °C and after 33 days at 220 °C (168).

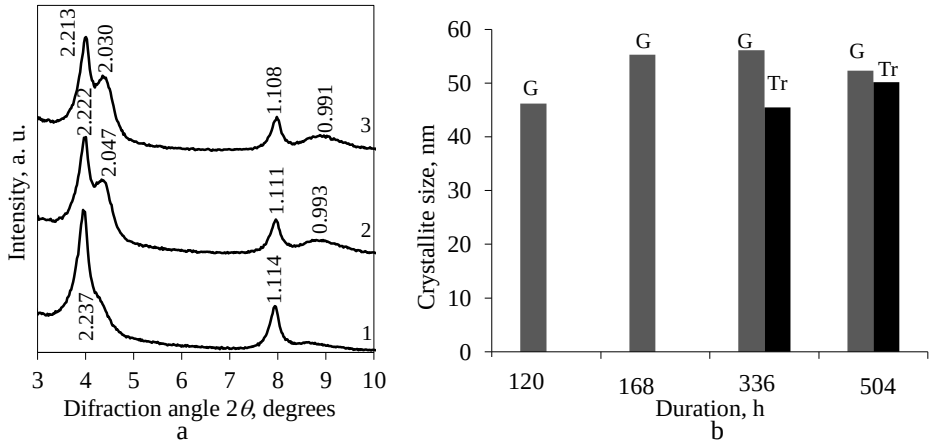

Figure 3.17. X-ray diffraction patterns (a) and crystallite size (b) of synthesis products with varying durations of hydrothermal treatment at 200 °C, h: 1 at 120; 2 at 336; 3 at 504. Indexes: G represents gyrolite, Tr stands for truscottite.

The obtained results were confirmed with STA analysis data (Figure 3.18., Tables 3.7. and 3.8.). On the DSC curve within the 139–143 °C temperature range, the broad endothermic peak is related to the loss of physisorbed and interlayer water from the crystal structure of the synthesis products. This peak slightly decreased by prolonging the synthesis duration to 504 h (Figure 3.18., curve 3). The second exothermic peak (~870 °C) is associated with the recrystallization of this compound into wollastonite. Moreover, at ~700 °C, due to the decarbonation of synthesis

products, a peak typical of calcium carbonate is also observed (Figure 3.18., curve 1–3).

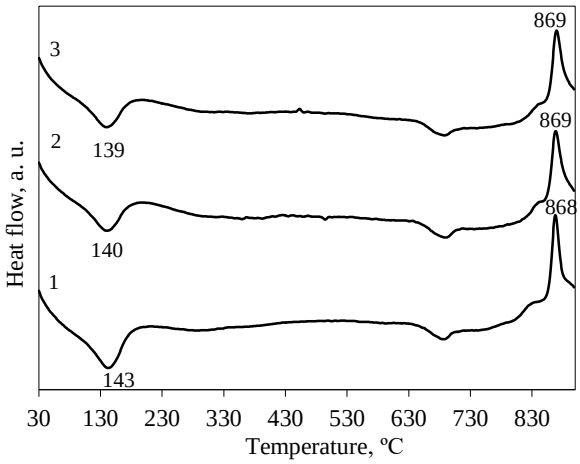

Figure 3.18. DSC curves of synthesis products in the mixtures with amorphous silica with varying durations of hydrothermal treatment at 200 °C, in h: 1 at 120 h; 2 at 336 h; 3 at 504 h.

It was observed that after 120–504 h of hydrothermal treatment, the heat of the endothermic effects at 80–200 °C decreased from 71.1 J/g to 54.2 J/g (Figure 3.18., Table 3.8.). Also, the typical temperatures of this effect shift to lower temperatures: T_{onset} from 111 °C to 108 °C; T_{max} from 143 °C to 140 °C; T_{end} varies from 176 °C to 175 °C. At the same time, the mass loss of this compound decreases from 3.9 wt. % to 3.1 wt. % (see Table 3.8.).

Table 3.8. The parameters of the endothermic effect at 80–200 °C of synthesis products in the mixtures with amorphous silica for varying durations of hydrothermal treatment.

Duration of hydrothermal treatment, h	T_{onset}, °C	T_{max}, °C	T_{end}, °C	Mass loss, %	Heat of reaction, J/g
120	111	143	175	3.9	71.1
168	115	145	177	3.6	69.3
336	108	140	174	3.3	55.1
504	108	140	175	3.1	54.2

It was estimated that the heat of the exothermic effect at 830–890 °C practically did not change till reaching 336 h but by prolonging the hydrothermal treatment duration till 504 h, it decreased to 47.8 J/g (Figure 3.18., Table 3.9.). Also, the typical temperatures of this effect shift to higher temperatures: T_{onset} from 857 °C to 858 °C; T_{peak} from 868 °C to |870 °C; T_{end} from 878 °C to 882 °C. Besides, the mass loss remained the same (Table 3.9.).

Table 3.9. Parameters of the exothermic effect at 830–890 °C of synthesis products in the mixtures with amorphous silica at varying durations of hydrothermal synthesis.

Duration of hydrothermal treatment, h	T_{onset}, °C	T_{max}, °C	T_{end}, °C	Mass loss, %	Heat of reaction, J/g
120	857	868	878	0.2	49.9
168	855	866	876	0.2	49.9
336	857	869	880	0.2	49.1
504	858	870	882	0.2	47.8

At the same time, the total amount of water in the formed calcium silicate hydrate structure slightly decreased by prolonging the synthesis duration from 120 to 504 h (Figure 3.19.) and can be expressed as:

(3.3 wt. % H_2O) 168 h <duration of synthesis (τ)< 168 h (4.1 wt. % H_2O)

The obtained results are in a good agreement with the data obtained by Gard *et al*. (169) and Lachowski *et al*. (170).

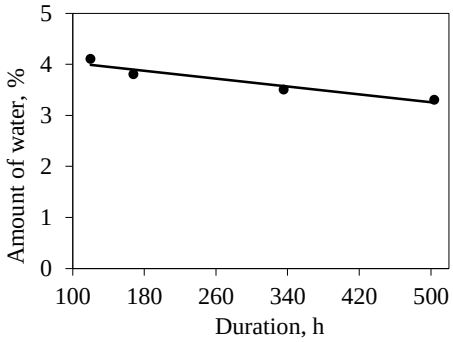

Figure 3.19. Dependence of the amount of water in the structure of the synthesis products on the duration of hydrothermal treatment at 200 °C.

FT-IR analysis data supports the above mentioned results. It was established that the hydrothermal treatment duration exerts influence on the width of the absorption bands and the peak intensities. It was also determined that by prolonging the treatment duration to 504 h, a sharp peak near 3639 cm^{-1} becomes more prominent and shows the decrease of the intensity of the H_2O bending and stretching bands (Figure 3.20., curves 2–3). A wide band near 3444–3554 cm^{-1} indicates that molecular water forms hydrogen bridges in the interlayers. The decrease of this band intensity shows the lower quantity of molecular H_2O in the synthesis product structure (see Figure 3.20., curves 2–3). Also, additional stretching bands at about 1252 and 807 cm^{-1} can be assigned to cross-linked tetrahedral units formed due to the polymerization of the single silicate sheets to double sheets thus forming a

framework (Q^4) (Figure 3.20., curves 2–3). Garbev *et al*. determined that these bands should be assigned to truscottite (171).

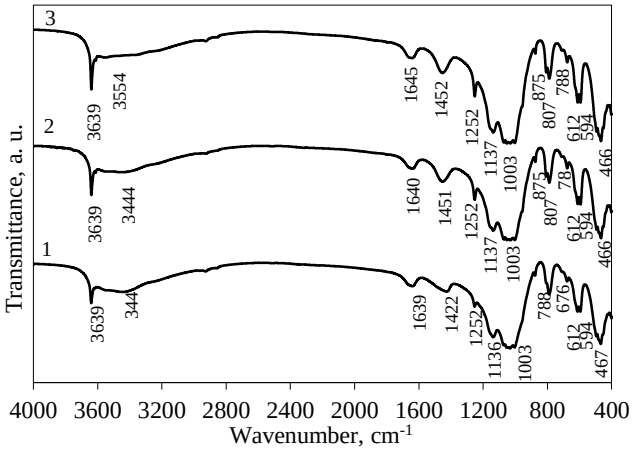

Figure 3.20. IR spectra of synthesis products in the mixtures with amorphous silica for varying durations of hydrothermal synthesis at 200 °C, in h: 1 at 168 h; 2 at 336 h; 3 at 504 h.

It has to be noted that duration of hydrothermal treatment exerts influence on the structure of the synthesis products as well as on its specific surface area (Table 3.10.).

Table 3.10. Parameters of the specific surface area (S_{BET}) of the synthesis products in the mixtures with amorphous silica

Duration of hydrothermal treatment, h	Sample mass *m*, g	BET equation constants		Capacity of monolayer X_m, g	S_{BE}, m^2/g	Constant C_{BET}	Reliability coefficient R^2
		Slope $S=tg\alpha$	Intercept *I*				
168	0.036	2095.7	7.0	0.0005	46.0	284.2	0.9991
336	0.063	1606.3	16.3	0.0006	35.8	99.5	0.9995
504	0.062	1735.4	15.7	0.0006	33.4	111.2	0.9994

It was determined that S_{BET} of the product was equal to 46.0 m^2/g after 168 h of isothermal treatment. When prolonging the hydrothermal synthesis duration to 336 h, the value of S_{BET} decreased to 35.8 m^2/g. Besides, this tendency was also observed after 504 h of treatment.

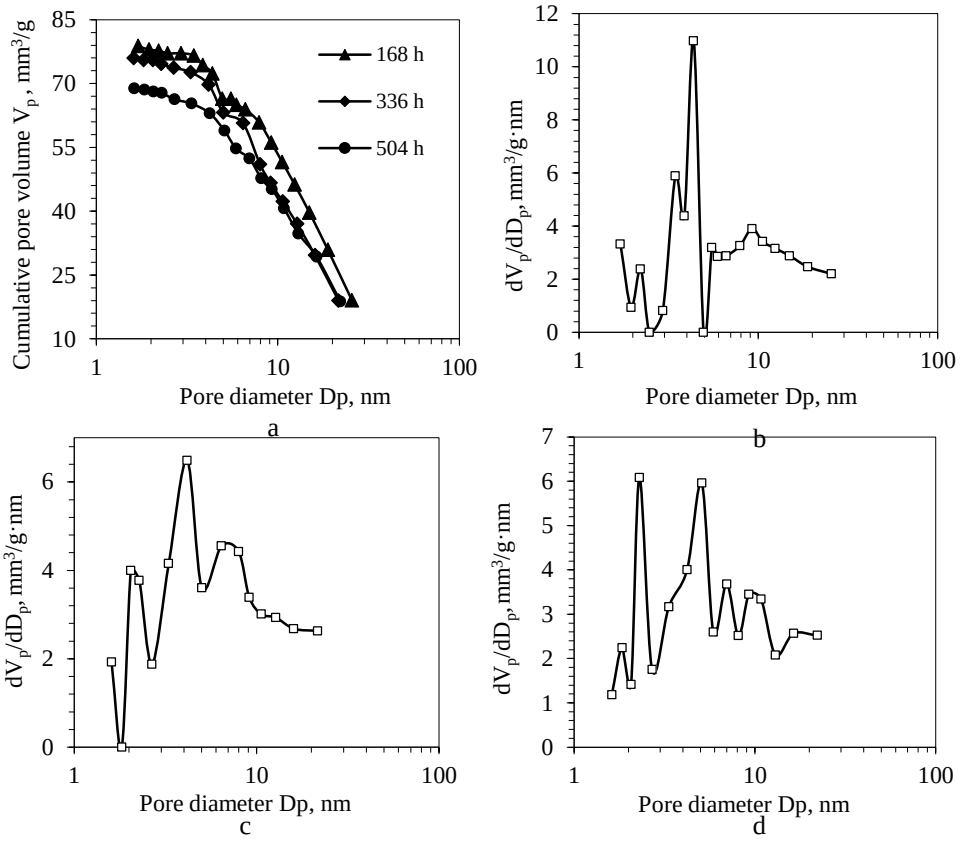

Figure 3.21. Total pore volume (a) and differential pore volume plot (b–d) of the synthesis product in the mixtures with amorphous silica at varying durations of hydrothermal treatment at 200 °C in, h: b at 168 h; c at 336 h; d at 504 h.

As it was expected, the pore volume of the synthesis product samples also decreased from 78.8 to 68.8 mm^3/g (Figure 3.21., a). Besides, the pores with the 2.0–5.0 nm radius dominated in the gyrolite structure after 168 h of synthesis (Figure 3.21., b). Meanwhile, the pores with the 3.0–5.0 nm and even larger radiuses started to form after 336 h of hydrothermal treatment (Figure 3.21., c). One of the main reasons could be the formation of new compound – truscottite. This tendency of the pore growth was manifested when continuing isothermal treatment (up to 504 h) because the pores with the 3.0–6.0 nm and 6.0–10.0 radius dominated in the synthesis product (Figure 3.21., d).

In order to examine the influence of silica-containing components with higher C/S molar ratios on the properties and the crystallization processes of calcium silicate hydrates under hydrothermal treatment, in the next stage of the experiment, the synthesis of higher basicity calcium silicate hydrates (C/S = 0.83 and 1.0) were performed.

3.2 Application of AlF_3 Production Waste to the Synthesis of Higher Basicity Calcium Silicate Hydrates

It was determined that, in a pure $CaO\text{-}SiO_2\text{-}H_2O$ mixture, when C/S molar ratio equals 0.83 after 8 h of isothermal treatment at 200 °C, the X-ray diffraction pattern shows basic reflections characteristic of 1.13 nm tobermorite (*d*-spacing of 1.138, 0.547, 0.308, 0.298, 0.184 nm) and C-S-H(I) (Figure 3.22., curve 1). By prolonging the duration of the synthesis to 24 h, the intensities of 1.13 nm tobermorite diffraction peaks noticeably increases, and the crystal structure of this compound becomes more orderly (Figure 3.22., curve 3). It was estimated that 1.13 nm tobermorite becomes unstable and starts to recrystallize into xonotlite (*d*-spacing of 0.713, 0.424, 0.308, 0.282, 0.204, 0.234, 0.184 nm) after 72 h (Figure 3.22., curve 4).

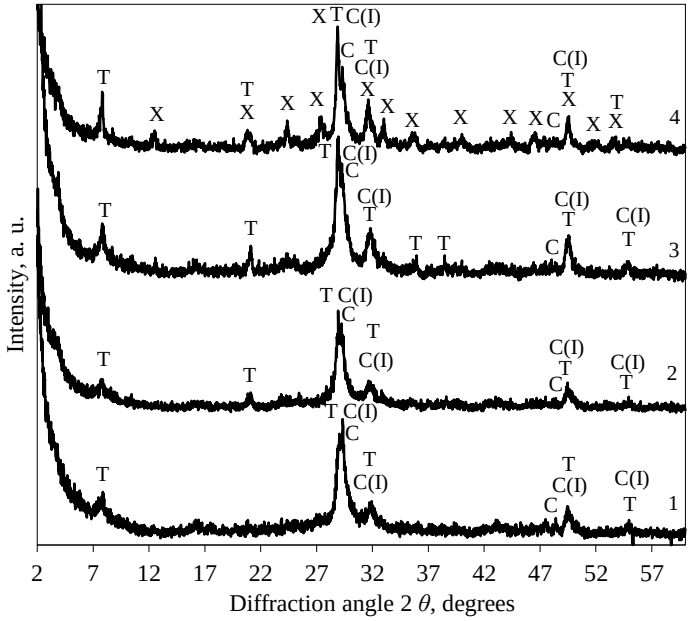

Figure 3.22. XRD patterns of hydrothermal synthesis products after different types of isothermal treatment at 200 °C in mixtures with amorphous silica oxide when C/S molar ratio is 0.83: 1 at 8 h; 2 at 16 h; 3 at 24 h; 4 at 72 h. Indexes: C(I) represents C-S-H(I); T denotes 1.13 nm tobermorite; X stands xonotlite; C depicts calcite.

Moreover, carbonation appeared when the products were dried in an air-conditioned chamber (50 ºC, 24 h) because the diffraction peaks characteristic of calcium carbonate were detected in the XRD patterns (Figure 3.22., curve 1).

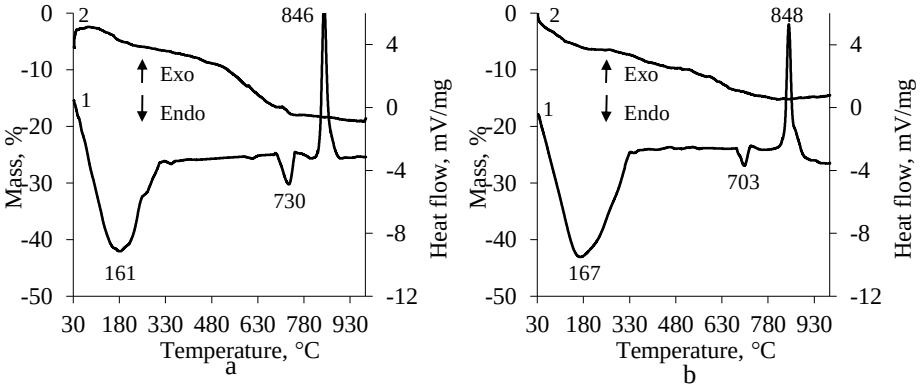

Figure 3.23. STA curves (1for DSC, 2 for TG) of synthesis products in pure mixtures when C/S = 0.83 and the duration of isothermal curing were, h: a at 8 h; b at 72 h.

The previously obtained results were confirmed with the STA and FT-IR analysis data. It was determined that the formed 1.13 nm tobermorite is denoted by lower crystallinity (Figure 3.22.), as expected; hence the endothermic effect at 160–167 °C, which can be attributed to the dehydration of 1.13 nm tobermorite (Figure 3.23., a, b), occurs at lower temperatures compared to the classic 1.13 tobermorite (172). It was determined that the exothermic effect at higher temperatures (~850 °C) was assigned to semi-crystalline C-S-H(I) recrystallization into wollastonite. It should be underlined that the heat of the above mentioned reaction decreases from 78.47 to 55.69 $J \cdot g^{-1}$ by increasing the duration of the synthesis (Figure 3.23.). Moreover, the endothermic effects at 703 °C and 730 °C can be assigned to the decomposition of calcium carbonate (Figure 3.23., a, b).

The FT-IR spectra showed that the stretching vibrations of OH– groups in H_2O or hydroxyls appear as a broad band in the range of 3455–3480 cm^{-1} and can be assigned to tobermorite (Figure 3.24., curve 1). The bending vibration band of molecular H_2O appears at ~1635 cm^{-1}. This broadening is due to the formation of hydrogen bonds with a wide range of strengths. The most intense spectral features of silicates appear as a complex group of bands in the area of ~974 cm^{-1}, which is attributed to asymmetrical stretching vibrations of SiO_4 tetrahedra. The second most intense silicate bands are broadly characterized as O-Si-O deformation or bending modes which occur in the 455 cm^{-1} region, and the band at ~672 cm^{-1} is due to Si-O-Si bending vibrations. The asymmetric stretching bands of CO_3^{2-} appear at 1488–1489 cm^{-1}. The last curve of the spectra confirms that the 1.13 nm tobermorite begins to recrystallize into xonotlite after 72 h of synthesis because absorption bands characteristic of xonotlite at 3612, 1201, and 611 cm^{-1} are dominant (see Figure 3.24., curve 3).

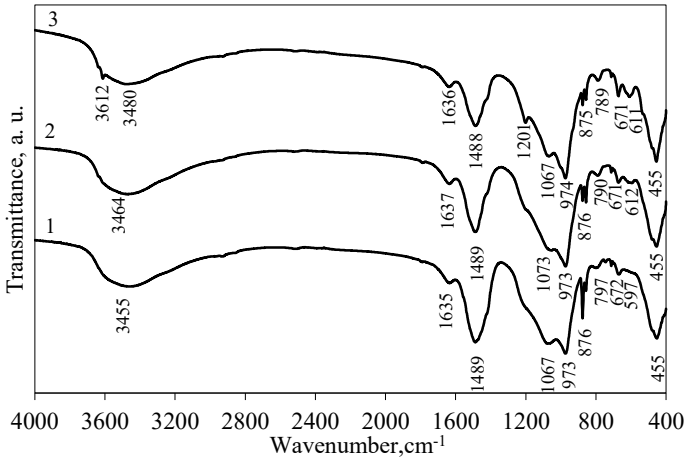

Figure 3.24. FT-IR curves of synthesis products in pure mixtures when C/S = 0.83 and the duration of isothermal curing are, h: 1 at 8 h; 2 at 16 h; 3 at 72 h.

Thus it was determined that in the system $CaO\text{-}SiO_2\text{-}H_2O$ with the C/S molar ratio of 0.83, the reactions of the compound formation occur in the following sequence:

$$CaO + SiO_2 \cdot nH_2O + H_2O \xrightarrow{8\ h} \left|\begin{array}{l}\text{1.13 nm tobermorite}\\ \text{C - S - H(I)}\end{array}\right. \xrightarrow{72\ h} \left|\begin{array}{l}\text{1.13 nm tobermorite}\\ \text{xonotlite}\\ \text{C - S - H(I)}\end{array}\right.$$

It should be noted that the obtained results are in good agreement with K. Baltakys' work (172). This scholar determined that in the pure system when the C/S molar ratio of initial mixture was 0.83, the 1.13 nm tobermorite already formed after 4 h of synthesis at 200 °C. Upon continuing the synthesis up to 72 h, the 1.13 nm tobermorite becomes unstable and starts to transform into a higher-basicity compound – xonotlite (172).

It should be underlined that the mechanism of hydrothermal reactions and the sequence of the compounds formed in the $CaO–AlF_3$ production waste $–H_2O$ system differs, as expected, because a part of the CaO reacts with the F^- and Al^{3+} ions and forms calcium fluoride and hydrogarnet, respectively (Figure 3.25., curves 1–4). Presumably, these formed compounds affect the formation of calcium silicate hydrates with a smaller C/S ratio, as was expected on the basis of the molar ratio of the initial mixture C/S being 0.83. It was estimated that after 8 h of hydrothermal synthesis, the low-base calcium silicate hydrate, the Z-phase whose stoichiometric composition corresponds to the molar ratio of C/S = 0.55, was identified (Figure 3.25., curve 1). After extending the duration of isothermal curing to 16 h, Z-phase formed together with gyrolite gel (Figure 3.25., curve 2). By prolonging the synthesis duration to 24 h, gyrolite gel becomes unstable and regroups into the final product of synthesis, gyrolite, which remains stable until the completion of the 72 h of synthesis (Figure 3.25., curves 3 and 4).

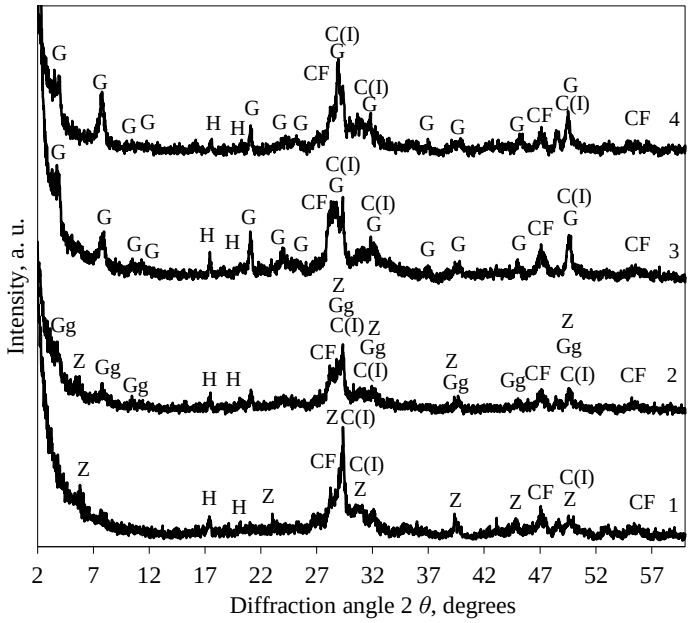

Figure 3.25. XRD patterns of hydrothermal synthesis products after various isothermal treatment at 200 °C in mixtures with AlF_3 production waste when C/S = 0.83 and the duration of isothermal curing is, h: 1 at 8 h; 2 at 16 h; 3 at 24 h; 4 at 72 h. Indexes: Z denotes Z phase; CF represents CaF_2; G stands for gyrolite; H shows hydrogarnet; Gg depicts gyrolite gel.

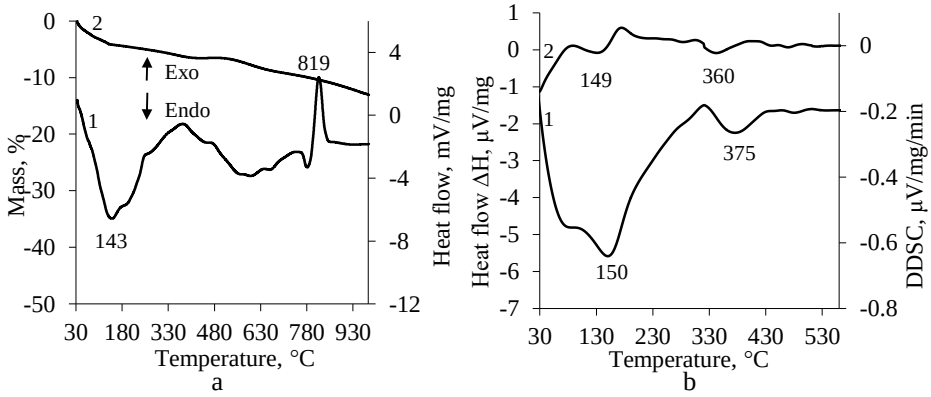

Figure 3.26. STA (1 for DSC, 2 for TG) (a) and DSC curves (1 for DSC, 2 for DDSC) (b) of synthesis products in mixtures with AlF_3 production waste when C/S = 0.83 and the duration of isothermal curing is 72 h.

The STA and DSC analysis data is in a good agreement with the XRD results. In the DSC curve, two endothermic effects were indicated: the 150 °C temperature is characteristic of dehydration of the structural water from the C-S-H crystal lattice, whereas the other endothermic effect at the temperature range of 375 °C is characteristic of the decomposition of hydrogarnet (Figure 3.26., b). It should be noted that the silica-containing compound exerts influence on C-S-H

recrystallization into wollastonite (as well as in the mixtures featuring the C/S molar ratio of 0.55 and 0.66) because in the mixtures with AlF_3 production waste, it is accelerated and identified at 819 °C temperature (Figure 3.26., a). Moreover, the heat of C-S-H recrystallization into wollastonite slightly increased to 60.76 $J \cdot g^{-1}$ in comparison with the pure system (55.69 $J \cdot g^{-1}$) after 72 h of synthesis.

The FT-IR spectra clearly show that a sharp band near 3636 cm^{-1}, which is visible only in the gyrolite spectrum, appears after 16 h of isothermal curing and becomes even sharper by prolonging the synthesis duration to 72 h (Figure 3.27.). Also, a doublet near ~597 and ~612 cm^{-1} that is due to Si–O–Si bending vibrations becomes more intense, and gyrolite has two bands in the range of 712–787 cm^{-1}. Thus in the system with the silica gel waste, gyrolite is the main compound.

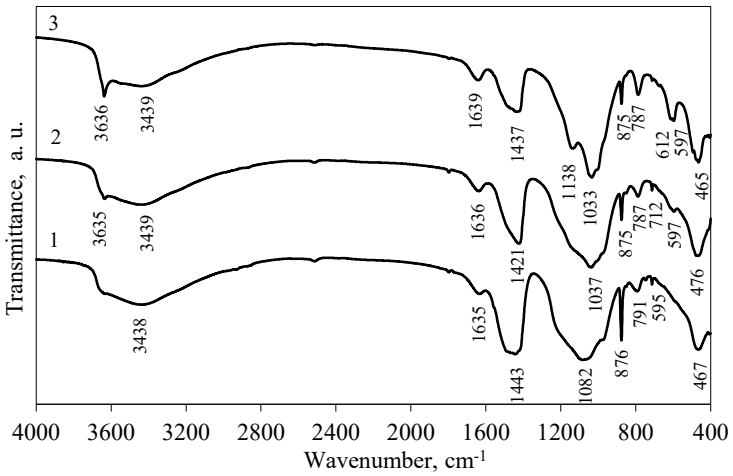

Figure 3.27. FT-IR curves of the synthesis products in mixtures with AlF_3 production waste when C/S = 0.83 and the duration of the isothermal curing is (in h): 1 at 8 h; 2 at 16 h; 3 at 72 h.

The chemical analysis of the synthesis solution showed that only a negligible amount of fluorine ions was released: the amount of F^- ions was not higher than 0.1 wt. % in the liquid medium (see Table 3.11.). It should be underlined that the latter value does not exceed the highest level according to the Centers for Disease Control and Prevention (CDC) (173–175). However, an insignificant increase of F^- ion concentration was observed when the synthesis duration was extended to 72 h.

Table 3.11. Concentration of F^- ions in the liquid medium after the synthesis process

Duration of the synthesis, h	The concentration of F^- ions, wt. %
8	0.035
16	0.052
48	0.061
72	0.066

Thus it can be stated that in the system with AlF_3 production waste, when C/S molar ratio equals 0.83, the formation of compounds can be presented as follows:

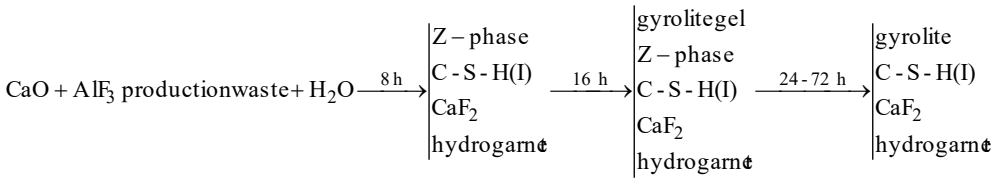

It was determined that in the $CaO\text{-}SiO_2\text{-}H_2O$system when C/S equals to 1.0 after 8 h of isothermal treatment, 1.13 nm tobermorite and C-S-H(I) (Figure 3.28., curve 1) is formed and remains stable till 24 h (Figure 3.28., curve 3). These results partially agree with the data obtained by other scientists (172) who claimed that xonotlite forms already within 8 h of the synthesis in the mixture of CaO and amorphous SiO_2. By prolonging the duration of the synthesis to 48 h (see Appendix 4, Figure A4.1., curve 4), peaks of xonotlite were observed and remained till 72 h (see Figure 3.28., curve 4). Moreover, carbonation appeared when the products were dried in an air-conditioned chamber (50 ºC, 24 h), because the diffraction peaks characteristic of calcium carbonate were detected in the XRD patterns (Figure 3.28., curves 1–4).

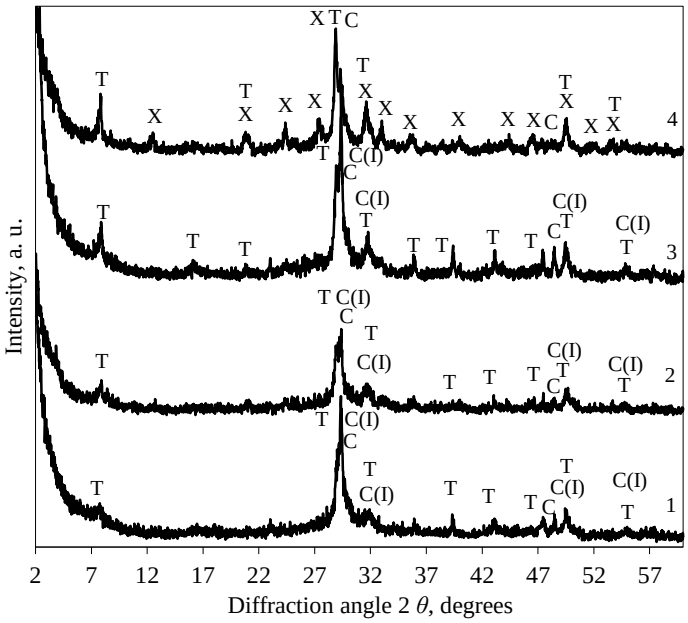

Figure 3.28. XRD patterns of hydrothermal synthesis products after various types of isothermal treatment at 200 °C in mixtures with amorphous silica oxide when the C/S molar ratio equals to 1 and the duration of isothermal curing is (in h): 1 at 8 h; 2 at 16 h; 3 at 24 h; 4 at 72 h. Indexes: T denotes 1.13 nm tobermorite; C represents calcite; X stands for xonotlite; C(I) depicts C-S-H(I).

Thus it was determined that in the $CaO\text{-}SiO_2\text{-}H_2O$ system with the C/S molar ratio of 1.0, the reactions of the compound formation occur in the following sequence:

$$CaO + SiO_2 \cdot nH_2O + H_2O \xrightarrow{8\,h} \left|\begin{array}{l}\text{1.13 nm tobermorite}\\ \text{C - S - H(I)}\end{array}\right. \xrightarrow{48\text{ - }72\,h} \left|\begin{array}{l}\text{1.13 nm tobermorite}\\ \text{xonotlite}\end{array}\right.$$

Meanwhile, in the system with AlF_3 production waste, the formation sequence of the intermediate and the final compounds differs if compared to the pure system (Figure 3.28.). It was estimated that after 8 h of hydrothermal synthesis Z-phase, 1.13 nm tobermorite and C-S-H(I) were identified (see Figure 3.29., curve 1). After 16 h of treatment, Z-phase transforms into 1.13 nm tobermorite and C-S-H(I) because the intensities of this compound noticeably increased (see Figure 3.29., curve 2). By prolonging the hydrothermal synthesis duration to 24 h, 1.13 nm tobermorite formed together with gyrolite gel and C-S-H(I) (see Figure 3.29., curve 3). This compound becomes unstable and starts to regroup into gyrolite after 48 h (see Appendix 5, Figure A5.1., curve 4) and remains stable till 72 h of synthesis (Figure 3.29). It should be mentioned that CaF_2 and hydrogarnet are formed and remain stable under all hydrothermal synthesis conditions (see Figure 3.29., curves 1–4) as well as with the C/S molar ratio of 0.83.

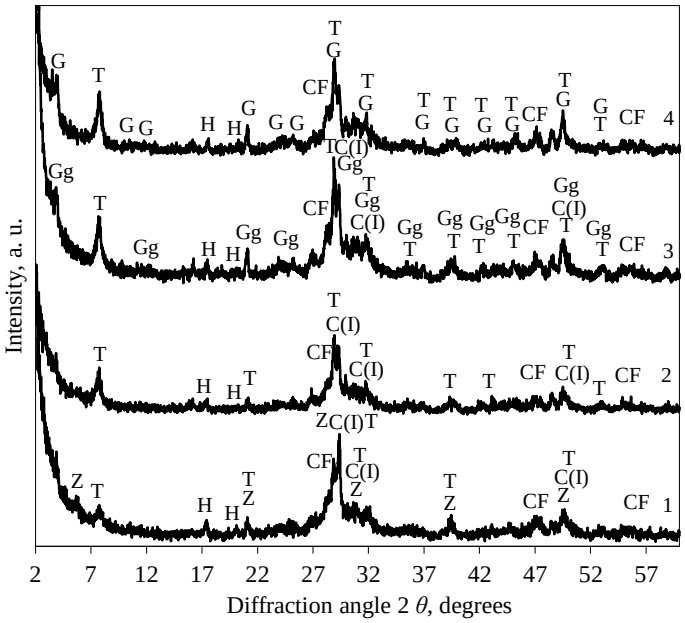

Figure 3.29. XRD patterns of hydrothermal synthesis products after various types of isothermal treatment at 200 °C in mixtures with AlF_3 production waste when the C/S molar ratio equals to 1 and the duration of isothermal curing is (in h): 1 at 8h; 2 at 16 h; 3 at 24 h; 4 at 72 h. Indexes: Z denotes Z phase; CF stands for CaF_2; G denotes gyrolite; H represents hydrogarnet; Gg shows gyrolite gel; T depicts 1.13 nm tobermorite; C(I) represents C-S-H(I).

Thus it was determined that in the system with AlF_3 production waste, when the C/S molar ratio equals to 1.0, the formation of compounds can be presented as follows:

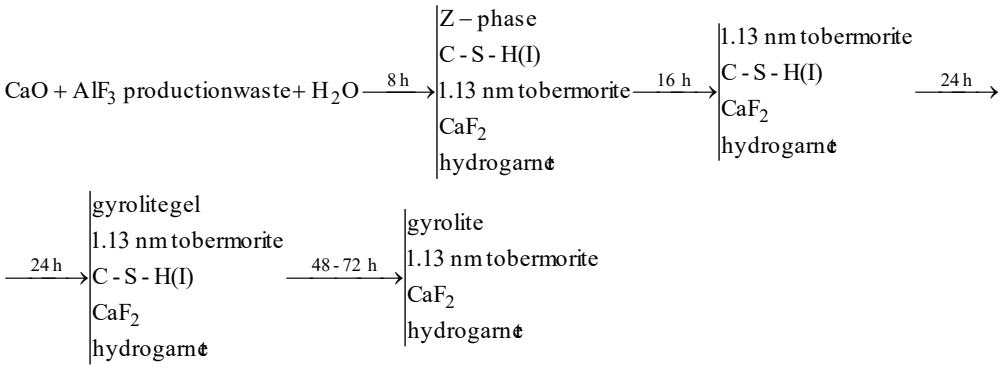

The experimental data and the theoretical hypothesis were also supported with thermodynamic calculations. The reactions that are possible during the interaction between $Ca(OH)_2$ and $SiO_2 \cdot nH_2O$ occur when the C/S ratio is equal to 0.83 (Equations 1–3), 0.66 (Equations 4–6) and 1.0 (Equations 7–9):

(1) 1.13 nm tobermorite:
$5Ca(OH)_2 + 6SiO_2 + 3H_2O \rightarrow 5CaO \cdot 6SiO_2 \cdot 5{,}5H_2O + 2.5H_2O$,
(2) Z-phase:
$5Ca(OH)_2 + 6SiO_2 + 3H_2O \rightarrow 3CaO \cdot 2SiO_2 \cdot 2H_2O + 2Ca(OH)_2$,
(3) gyrolite:
$5Ca(OH)_2 + 6SiO_2 + 3H_2O \rightarrow 2(2CaO \cdot 3SiO_2 \cdot 2.5H_2O) + 2Ca(OH)_2 + 2H_2O$,
(4) 1.13 nm tobermorite:
$2Ca(OH)_2 + 3SiO_2 + H_2O \rightarrow 0.4(5CaO \cdot 6SiO_2 \cdot 5.5H_2O) + 0.6SiO_2 + 0.8H_2O$,
(5) Z-phase:
$2Ca(OH)_2 + 3SiO_2 + H_2O \rightarrow CaO \cdot 2SiO_2 \cdot 2H_2O + Ca(OH)_2 + SiO_2$,
(6) gyrolite:
$2Ca(OH)_2 + 3SiO_2 + H_2O \rightarrow 2CaO \cdot 3SiO_2 \cdot 2.5H_2O + 0.5H_2O$,
(7) 1.13 nm tobermorite:
$Ca(OH)_2 + SiO_2 + H_2O \rightarrow 0.1667(5CaO \cdot 6SiO_2 \cdot 5.5H_2O) + 0.1665CaO + 1.083H_2O$,
(8) xonotlite:
$Ca(OH)_2 + SiO_2 + H_2O \rightarrow 0.1667(6CaO \cdot 6SiO_2 \cdot H_2O) + 1.833H_2O$,
(9) gyrolite:
$Ca(OH)_2 + SiO_2 + H_2O \rightarrow 0.333(2CaO \cdot 3SiO_2 \cdot 2.5H_2O) + 0.334CaO + 1.168H_2O$,

Moreover, for the calculation of the hypothetical reaction parameters, the values of enthalpy $\Delta H_{298}^{0,f}$, entropy $\Delta S_{298}^{0,f}$, molar specific heat capacities (C_p), and empirical constants (*a*, *b*, *c*, *c'*) of the formed compounds are applied and given in Table A2.1. (presented in Appendix 2)).

The theoretical possibilities of 1.13 nm tobermorite (1, 4, and 7), Z-phase (2 and 5), gyrolite (3, 6, and 9) and xonotlite (8) reactions are given in Figure 3.30. (a, b and c) $\Delta_r G_T^0 = f(T)$ plot and in Table A3.1. (presented in Appendix 3)).

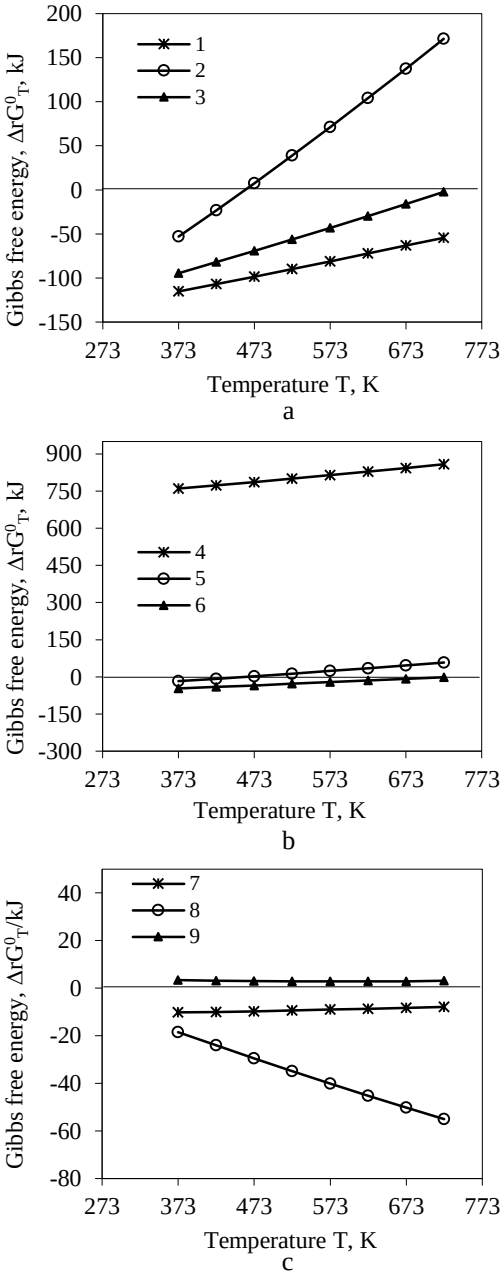

Figure 3.30. Gibbs free energy values as a function of temperature for 1.13 nm tobermorite (curves 1, 4, and 7); Z-phase (curves 2 and 5); gyrolite (curves 3, 6, and 9) and xonotlite (curve 8) reactions at 373–773 °K.

The data presented in Figure 3.30 *a* clearly shows that during the reaction, in the system $Ca(OH)_2$-SiO_2-H_2O, the greatest possibility is that the 1.13 nm tobermorite is one of the main compounds in the products (when C/S = 0.83) because the obtained Gibbs free energy value of this compound is the lowest one (Figure 3.30., a, curve 1, and Table A3.1. (see Appendix 3)). It should be noted that the formation of Z-phase in such conditions is the least probable, and it still decreases with the increasing temperature (Figure 3.30., a, curve 2, and Table A3.1. (see Appendix 3)).

Thermodynamic calculations for reactions 4–6 showed that gyrolite should dominate as the main product of synthesis when the C/S molar ratio equals to 0.66 (see Figure 3.30, b, curve 6, and Table A3.1 (see Appendix 3)). Meanwhile, the possibility of 1.13 nm tobermorite formation is the lowest (Figure 3.30., b, curve 5, and Table A3.1. (see Appendix 3)).

Meanwhile, thermodynamic calculations for reactions 7–9 showed that xonotlite should dominate as the main product of synthesis when the C/S molar ratio equals to 1.0 (see Figure 3.30, c, curve 8, and Table A3.1. (see Appendix 3)), and the possibility of gyrolite formation is the lowest (Figure 3.30., c, curve 9, and Table A3.1. (see Appendix 3)).

3.3 The Stability of Synthetic Calcium Silicate Hydrates and Formed CaF_2 at 600–1000 °C Temperature

In order to determine the influence of CaF_2 on the thermal behavior of C-S-H in the CaO-AlF_3 production waste -H_2O system, in the next stage of the experiment, the obtained products were calcined in the 600–1000 °C temperature range.

Hydrothermal synthesis was carried out on the basis of the previous results, with which it was determined that in the mixtures with the C/S molar ratio of 0.55, after 16 h of hydrothermal treatment, Z-phase and gyrolite gel were obtained (Figure 3.31., a, curve 1). After 48 h of isothermal curing, only gyrolite formed in the system with the C/S molar ratio of 0.66 (Figure 3.31., b, curve 1). The mentioned compound recrystallized into gyrolite gel and the 1.13 nm tobermorite when the C/S molar ratios were equal to 0.83 and 1.0 (Figure 3.32., a, b, curve 1). Thus it was discovered that the C/S molar ratio of the primary CaO- AlF_3 production waste -H_2O mixture exerts influence on the mineralogical composition of the synthesized C-S-H.

It was established that, under all experimental conditions, a part of CaO reacts with the F^- and Al^{3+} ions and forms calcium fluoride and hydrogarnet, respectively (Figures 3.31. and 3.32., curve 1). In addition, the intensities of diffraction maximums characteristic of calcium fluoride decreased with the increasing C/S molar ratio. Chemical analysis of the synthesis solution showed that fluoride ions reacted and/or were adsorbed by synthesis products because the amount of F^- ions in the liquid medium was very low (< 0.2%) if compared with the amount of F^- ions in the AlF_3 production waste.

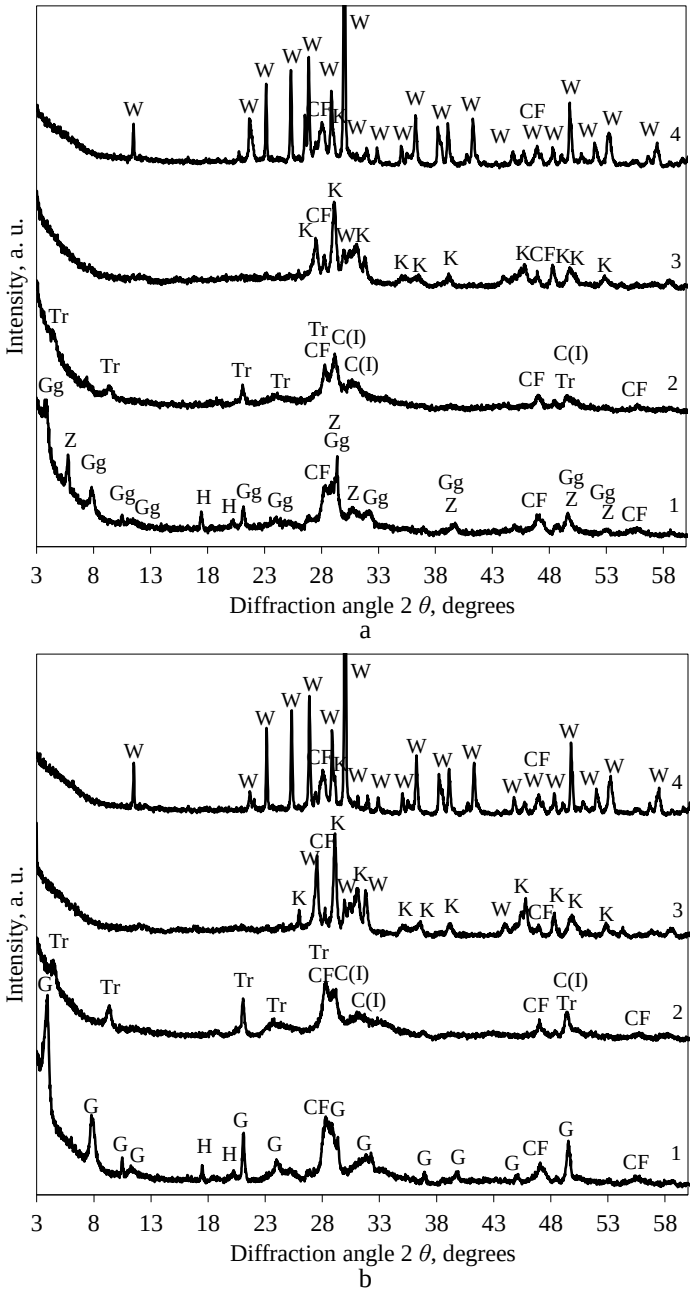

Figure 3.31. X-ray diffraction patterns of synthesized (curve 1) and calcined (2 at 600 °C; 3 at 800 °C; 4 at 1000 °C) products, when the C/S molar ratio: a is equal to 0.55 (16 h); b is equal to 0.66 (48 h). Indexes: Z denotes Z phase; CF shows CaF_2; Tr represents truscottite; K stands for cuspidine ($Ca_4Si_2O_7F_2$); W depicts wollastonite;Gg shows gyrolite gel; H represents hydrogarnet; G denotes gyrolite; C(I) shows C-S-H(I).

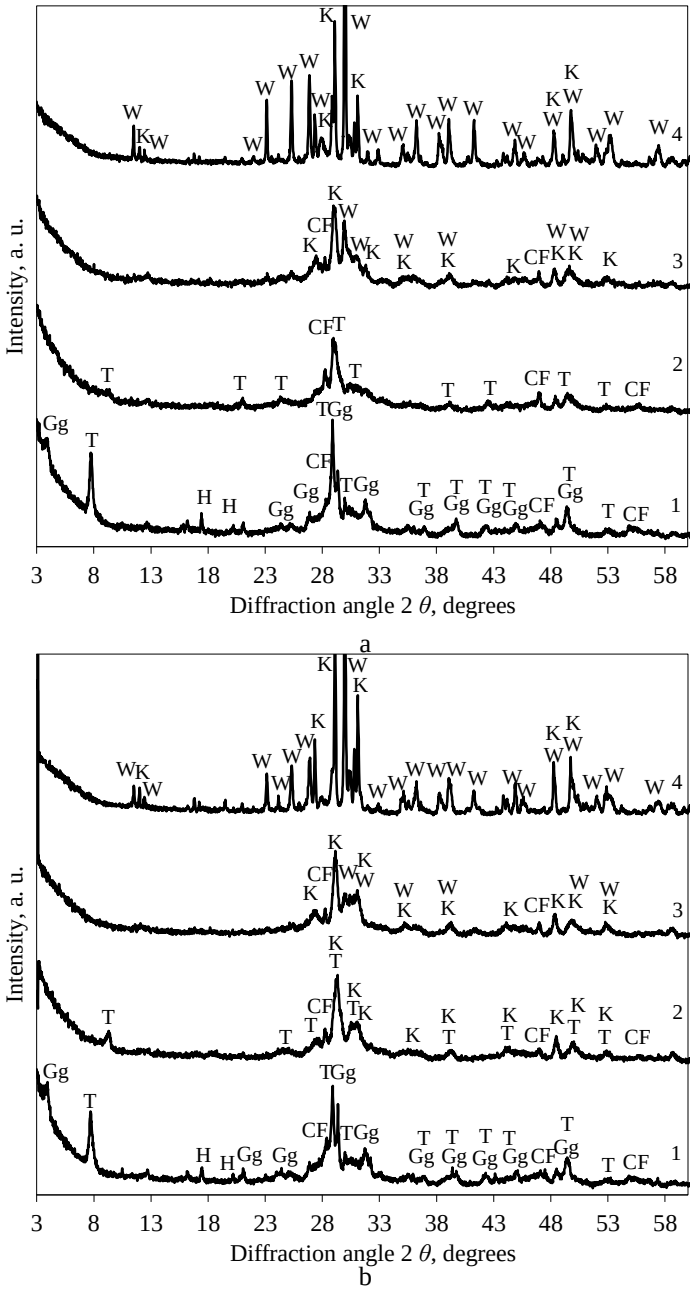

Figure 3.32. X-ray diffraction patterns of synthesized (curve 1) and calcined (2 at 600 °C, 3 at 800 °C, 4 at 1000 °C) products when the C/S molar ratio: a is equal to 0.83 (48 h); b is equal to 1.0 (48 h). Indexes: CF stands for CaF_2; K denotes cuspidine ($Ca_4Si_2O_7F_2$); W represents wollastonite; Gg shows gyrolite gel; H depicts hydrogarnet; T presents 1.13 nm tobermorite.

It was ascertained that already at the temperature of 600 °C, the synthesized gyrolite regroups into related compound truscottite (the *d*-spacing equaling 1.880,

0.942, 0.769, 0.471, 0.314, 0.183, and 0.176 nm) when the C/S molar ratio is 0.55 and 0.66 (see Figure 3.31., a, b, curve 2). Also, peaks of semi-crystalline calcium silicate hydrate C-S-H(I) were observed. Besides, a new compound – calcium fluoride silicate/cuspidine ($Ca_4Si_2O_7F_2$, with the *d*-spacing of 0.737, 0.343, 0.306, 0.287, 0.184, 0.183) – formed at 800°C. It should be underlined that CaF_2 remained stable after calcination at 1000 °C for 30 min in the system with the C/S molar ratio of 0.55 and 0.66 (Figure 3.31., a and b).

Meanwhile, in the system with higher C/S molar ratios (0.83 and 1.0), CaF_2 fully recrystallized into cuspidine at a temperature of 1000 °C (Fig. 3.32., a and b). In addition, a well-crystallized C-S-H compound – wollastonite ($CaSiO_3$) (*d*-spacing equalling 0.769; 0.409; 0.384; 0.351; 0.298; 0.183 nm) – started to form at 800°C temperature under all C/S molar ratios, and the peaks of the above mentioned compound significantly increased at 1000 °C (see Figures 3.31. and 3.32., curve 4).

The formation of CaF_2 was also proven with SEM/EDX analysis (Figure 3.33.). The accumulation of crystals of two different morphologies can be seen in SEM micrograph: gyrolite/Z-phase characteristic plate shape crystals and cube-shaped crystals of CaF_2 (the chemical composition of spectrum 1 is the following (in wt. %): F constituting 20.18%, O making up 40.91%, Si constituting 5.21%, Ca making up 20.18%, and Al constituting 13.52%) which are formed on plate crystals (Figure 3.30., a). Meanwhile, with the C/S molar ratio of C/S = 0.83, fluoride ions participate in only for the formation of CaF_2, but also interfere into the structure of products. The results of EDX analysis showed that there are 9.97 wt. % of fluorine in the structure of synthesis products (Figure 3.33., b).

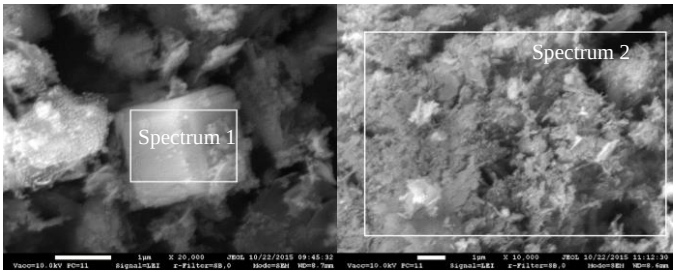

a b

Figure 3.33. Scanning electron micrograph (SEM) of synthesis products when the C/S molar ratios of the primary mixture are as follows: a is equal to 0.55; b is equal to 0.83. The chemical composition of spectrum 1, in wt. % was found to be as follows: F constituting 20.18%; O making up 40.91%; Si constituting 5.21%; Ca making up 20.18%; Al constituting 13.52%. The chemical composition of spectrum 2, in wt. %: F constituting 9.97%; O making up 47.44%; Si constituting 13.73%; Ca making up 26.74%; Al constituting 2.12%.

It was determined that the recrystallization processes and the formation of new compounds influence the morphology of calcined products. It is clearly seen from SEM micrographs that agglomerates with globules were formed under all the experimental conditions (Figure 3.34., a, b).

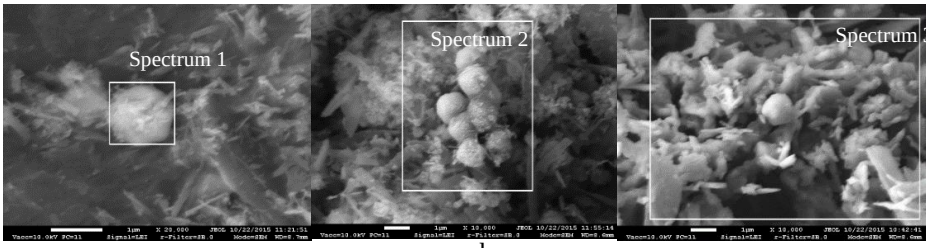

a b c

Figure 3.34. Scanning electron micrographs of synthesis products when the C/S molar ratios and calcination temperature are as follows: a is equal to 0.83 (600 °C); b is equal to 1.0 (600 °C); c is equal to 0.66 (1000 °C). The chemical composition of spectrum 1, wt. % was found out to be: F constituting 16.24%; O making up 52.47%; Si constituting 6.47%; Ca making up 19.13%; Al constituting 5.69%. The chemical composition of spectrum 2, in wt. % was found to be as follows: F constituting 9.13%; O making up 46.14%; Si constituting 15.25%; Ca making up 27.73%; Al constituting 1.75%. The chemical composition of spectrum 3, in wt. % was found to be as follows: F constituting 9.05%; O making up 47.02%; Si constituting 16.88%; Ca making up 25.42%; Al constituting 1.63%.

After calcination at 1000 °C, the agglomerates consisting of plate form crystals characteristic of wollastonite, and irregular globule-shaped crystals typical of fluorine-containing compounds were observed. Moreover, EDX analysis confirmed that fluorine is present in the crystal structure of calcination products (the chemical composition of spectrum 3 was found to be as follows, wt. %: F constituting 9.05%, O making up 47.02%, Si constituting 16.88%, Ca making up 25.42%, Al constituting 1.63%) (Figure 3.34., c).

FT-IR analysis data confirmed the above mentioned results. The FT-IR spectra present the decrease of the wide band intensity near 3431–3448 cm^{-1}, which shows the lower quantity of molecular water (which forms hydrogen bridge links in the interlayers) in the structure of the synthesis products. Also, bands in the ~1640 cm^{-1} frequency range, which are assigned to $\delta(H_2O)$ vibrations, disappear at 1000 °C. The two bands positioned at 513 cm^{-1} and 475 cm^{-1} were assigned to Si–O bending vibration. The bands at ~1061 cm^{-1} and ~904 cm^{-1} are due to the asymmetric stretching vibrations of the Si–O–Si and O–Si–O absorption peaks, respectively (Figure 3.35.). It should be noted that, the bands observed at ~715 and at ~650 cm^{-1} can be attributed to $[Si_2O_7]^6$-dimer, $[SiF_6]^{2-}$-octahedral complexes and confirm the formation of cuspidine in the temperature range of 800–1000 °C.

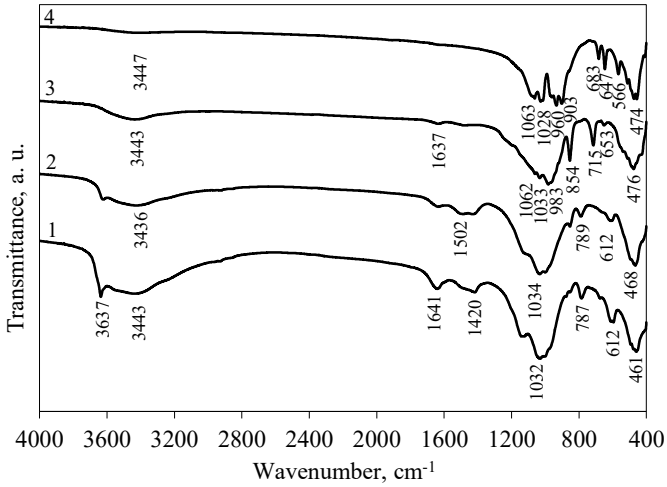

Figure 3.35. FT-IR spectra of synthesized (curve 1) and calcined products (2 at 600 °C; 3 at 800 °C; 4 at 1000 °C), the when C/S molar ratio is 0.66 (48 h).

In order to summarize the obtained experimental data, the formation sequence of compounds after hydrothermal treatment and calcination at different conditions is outlined in Figure 3.36. It was determined that the chemical composition of synthesized C-S-H affects the stability of the formed CaF_2, because it remained stable in the system with the C/S molar ratios of 0.55 and 0.66. Meanwhile, in the system with higher C/S molar ratios of 0.83 and 1.0, CaF_2 fully recrystallized into cuspidine.

Besides, it was determined that CaF_2 accelerates the reaction of C-S-H recrystallization into wollastonite because this compound started to form at lower temperatures (at ~800 °C, Figure 3.36.) comparing with the above mentioned reaction in the pure system.

<table>
<tr><td rowspan="2">Molar ratio of C/S</td><td rowspan="2">Products</td><td colspan="5">Calcination temperature, °C</td></tr>
<tr><td>600</td><td>700</td><td>800</td><td>900</td><td>1000</td></tr>
<tr><td>0.55</td><td>Gyrolite, Z-phase, CaF_2, hydrogarnet</td><td colspan="2" rowspan="2">Truscottite, C-S-H(I), CaF_2</td><td colspan="2" rowspan="3">Cuspidine, wollastonite, CaF_2</td><td rowspan="2">CaF_2, wollastonite, cuspidine</td></tr>
<tr><td>0.66</td><td>Gyrolite, CaF_2, hydrogarnet</td></tr>
<tr><td>0.83</td><td rowspan="2">Gyrolite gel, 1.13 nm tobermorite, CaF_2, hydrogarnet</td><td>1.13 nm tobermorite, CaF_2</td><td rowspan="2">Cuspidine, CaF_2</td><td rowspan="2">Cuspidine, wollastonite</td></tr>
<tr><td>1</td><td>Cuspidine, CaF_2</td></tr>
</table>

Figure 3.36. The formation sequence of compounds after hydrothermal treatment and calcination at different conditions.

On the other hand, AlF_3 production waste has positive influence on the formation of low basicity calcium silicate hydrates and independently on the initial

mixture of C/S molar ratio, one of the main compound of synthesis is gyrolite. Thus, in the next stage of the experiment gyrolite application in adsorption process were investigated.

3.4 Gyrolite Application for Zn^{2+} Ions Adsorption Process in Acidic and Alkaline Solutions

High levels of zinc can be found in certain soils naturally or as a result of a long-term anthropogenic activity which leads to its accumulation, such as the use of fertilizers or industrial waste (176, 177). It belongs to the second class of toxicity characterized by low mutagenic and carcinogenic properties (178). By ingesting food and drinking water containing a high concentration of zinc, human health may be endangered: corneal ulcers can form, and the oesophagus can be damaged with this heavy metal (179). Various adsorbents can be used for the removal of such metals from waste water: aluminosilicates, clays, zeolites, activated carbon and others. However, many of these adsorbents are not effective and have a lower adsorption capacity than synthetic adsorbents. Meanwhile, it is already known that calcium silicate hydrates prepared under hydrothermal treatment act as adsorbents for the removal of heavy metal ions. In previous work (167), it was found that gyrolite exhibits a higher adsorption rate for zinc ions; however, kinetic calculations were not performed. Thus the influence of adsorption kinetic parameters and adsorptive pH values on the reaction of Zn^{2+} ions with different crystallinity gyrolite samples were examined in detail.

The results of the adsorption analysis showed that in the $Zn(NO_3)_2$ solution with pH ~5.6 and the initial concentration of Zn^{2+} ions equal to 0.3 g/dm^3, after 30 s, more than 68% Zn^{2+} ions (20.43 mg Zn^{2+}/g) intercalate into gyrolite (synthesized after 48 h at 200 °C, in the $CaO\text{-}SiO_2\text{-}H_2O$ system) crystal lattice (Figure 3.37.).

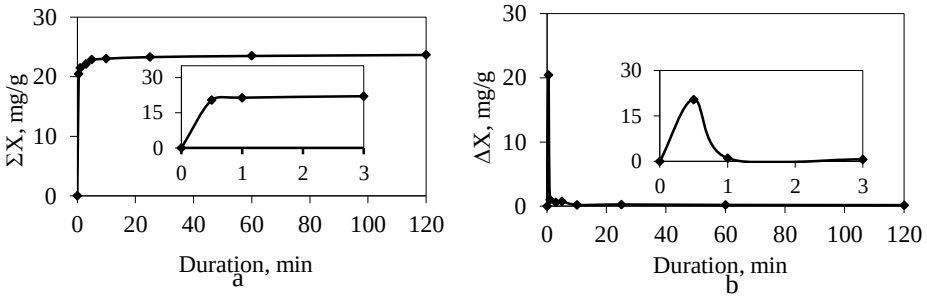

Figure 3.37. Integral (a) and differential (b) kinetic curves of Zn^{2+} ions adsorption on gyrolite synthesized after 48 h at 200 °C in the $CaO\text{-}SiO_2\text{-}H_2O$ system, in acidic solution.

After the increase duration of the interaction, the zinc ions concentration in the solution decreases steadily. It should be noted that the adsorption process occurs within 5 min because the amount of intercalated zinc ions into the gyrolite structure may only increase to 22.82 mg Zn^{2+}/g, and does not go up afterwards (Figure 3.37., a).

It should be noted that when zinc ions intercalate into the gyrolite structure, calcium ions are released from the crystal lattice of the adsorbent into the solution. Most Ca^{2+} ions are released during the first minutes because, after 5 minutes, their concentration (Σx_{Ca2+}) is equal to 17.95 mg Ca^{2+}/g, and after 2 h, Σx_{Ca2+} only increased till 18.79 mg Ca^{2+}/g (Figure 3.38.).

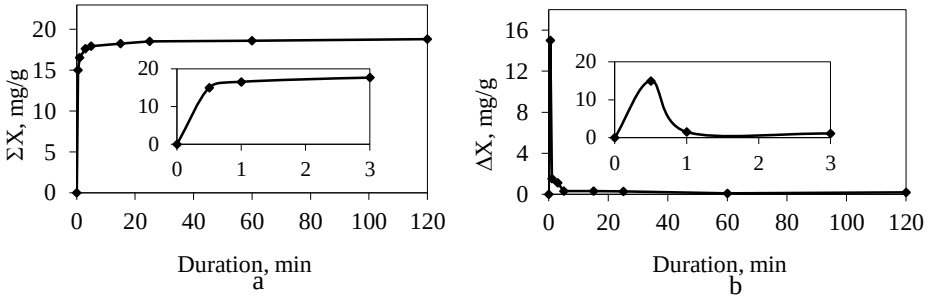

Figure 3.38. Integral (a) and differential (b) kinetic curves of Ca^{2+} ions concentration variation in acidic solution.

It was estimated that almost all zinc ions intercalated into the gyrolite structure only by the substitution reaction: gyrolite-Ca^0 + Zn^{2+} ↔ gyrolite-Zn^0 + Ca^{2+}. The main reason of this phenomenon could be the pH value of the initial cation metal solutions.

It should be noted that the significant change of the pH value in the reaction medium was observed at the beginning of adsorption (3–5 min) because the value of pH varied from 5.6 to 6.5 (Figure 3.39.). Presumably, this variation of the pH value depends on the increment of the quantity of Ca^{2+} ions in the solution.

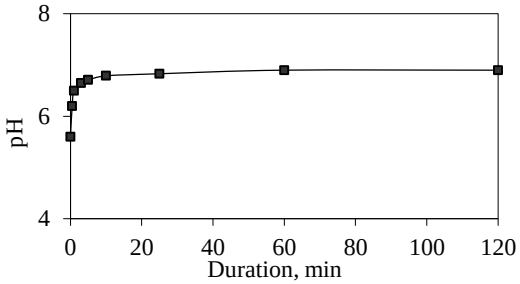

Figure 3.39. Variation of acidic solution pH value during Zn^{2+} ions adsorption on gyrolite.

After the adsorption experiment, gyrolite powder was dried and poured into decarbonized water for the leaching test. It was determined that the zinc ion sconcentration in the solution after 120 minutes at 25 °C did not exceed ~0.008 %.

Thus it was found that the adsorption of zinc ions by gyrolite is irreversible in the acidic solution.

The obtained data showed that the adsorptive nature has the determining influence on the gyrolite adsorption capacity because V. Kasperavičiūtė *et al*. (71)

showed that, in the acidic medium, gyrolite acts as a chemosorbent which can adsorb only as much as 41.48% of Cu^{2+} ions.

In order to identify the stability of gyrolite after adsorption, it was characterized by XRD and STA methods.

XRD analysis showed that gyrolite in the acidic solution is unstable because after 2 h of adsorption, the intensity of gyrolite main diffraction peak (the *d*-spacing of 2.273 nm) decreases (see Figure 3.40., a, curve 2). It was determined that gyrolite recrystallized into gyrolite gel (the *d*-spacing of 2.205, 1.106, 0.830, 0.304, 0.279, 0.183 nm) and variable (undefined) composition of the semi-crystalline compound – C-S-H(I) (the *d*-spacing of 0.304, 0.279, 0.183 nm) (see Figure 3.40., a, curve 2).

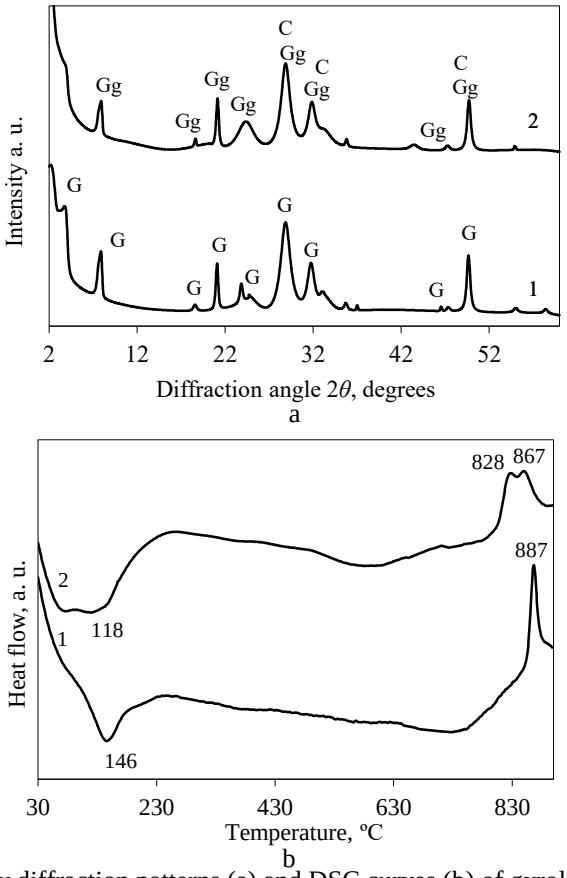

Figure 3.40. X-ray diffraction patterns (a) and DSC curves (b) of gyrolite synthesized after 48 h at 200 °C, in the $CaO\text{-}SiO_2\text{-}H_2O$ system: 1 shows data before adsorption, 2 represents values after adsorption. Indexes: G stands for gyrolite; Gg denotes gyrolite gel; C depicts C-S-H(I).

These results were confirmed by DSC data: the typical endothermic effect at ~146 °C is that of gyrolite (Figure 3.40., b) which moved to a lower temperature at ~118 °C after 2 h of adsorption (see Figure 3.40., b, curve 2). Also, two exothermic effects were identified at the temperatures of 828 °C and 867 °C which are typical of gyrolite gel and CSH(I), respectively (see Figure 3.40., b, curve 2). It should be

noted that these compounds recrystallize into wollastonite at lower temperatures compared to the pure gyrolite sample (see Figure 3.40., b, curve 1).

This data agrees with A. Stumm *et al*.'s (180) results – these scholars indicated that zinc incorporation into synthetic gyrolite is possible up to Zn/(Zn+Ca) = 1/6, corresponding to approximately 6 wt. %. Increasing the zinc content led to a gradual diminishing of the basal reflection (001) not only of gyrolite, but also to that of the nanocrystalline phases.

Thus it was found that gyrolite regroups into related compounds in the acidic solution; therefore, in order to increase the stability of the adsorbent, adsorption reactions of zinc ions were studied in the alkaline medium.

It was determined that in alkaline solution (pH ~ 9.0), adsorption proceeded faster and more efficiently than in acidic solution. After 30 s, more than 95% of Zn^{2+} ions (28.50 mg Zn^{2+}/g) intercalated into the gyrolite crystal lattice (Figure 3.41., a). It should be noted that the ion exchange in gyrolite occurred within 1 min because almost all the Zn^{2+} ions (29.12 mg Zn^{2+}/g) intercalated in the structure of this compound (Figure 3.41., b).

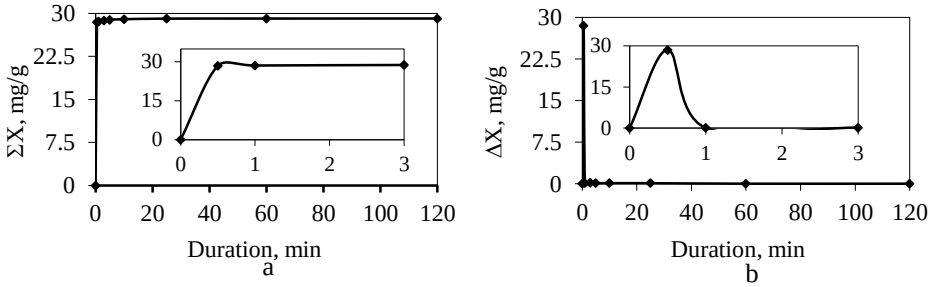

Figure 3.41. Integral (a) and differential (b) kinetic curves of Zn^{2+} ions adsorption on gyrolite synthesized after 48 h at 200 °C in the $CaO-SiO_2-H_2O$ system, in alkaline solution.

It should be noted that the amount of calcium ions released from gyrolite crystal structure in the alkaline solution is significantly lower than that in the acidic solution. Most of Ca^{2+} ions are released within 5 minutes because their concentration (Σx_{Ca2+}) is equal to 13.92 mg Ca^{2+}/g, and after 2 h, Σx_{Ca2+} only increased up to 14.53 mg Ca^{2+}/g (Table 3.12.).

Table 3.12. The amount of desorbed Ca^{2+} ions in alkaline solution

Time, min	$\Delta X(Ca^{2+})$, mg/g	$\Sigma X(Ca^{2+})$, mg/g
0	0	0
0.5	10.82	10.82
1	1.20	12.02
3	1.00	13.02
5	0.90	13.92
15	0.30	14.22
25	0.20	14.42
60	0.10	14.52
120	0.01	14.53

It was determined that the substitution reaction was typical of gyrolite in the alkaline solution because 82% of Zn^{2+} ions participated in the substitution/chemical reaction (gyrolite-Ca^0 + Zn^{2+} ↔ gyrolite-Zn^0 + Ca^{2+}), whereas the rest of these ions were present in gyrolite according to the addition interaction.

It was discovered that the pH value in the alkaline solution during the adsorption process does not vary: pH is equal to 9.0 ± 0.1.

In order to identify the stability of gyrolite, the products of adsorption were characterized by XRD and DSC analysis (see Figure 3.42., a, b).

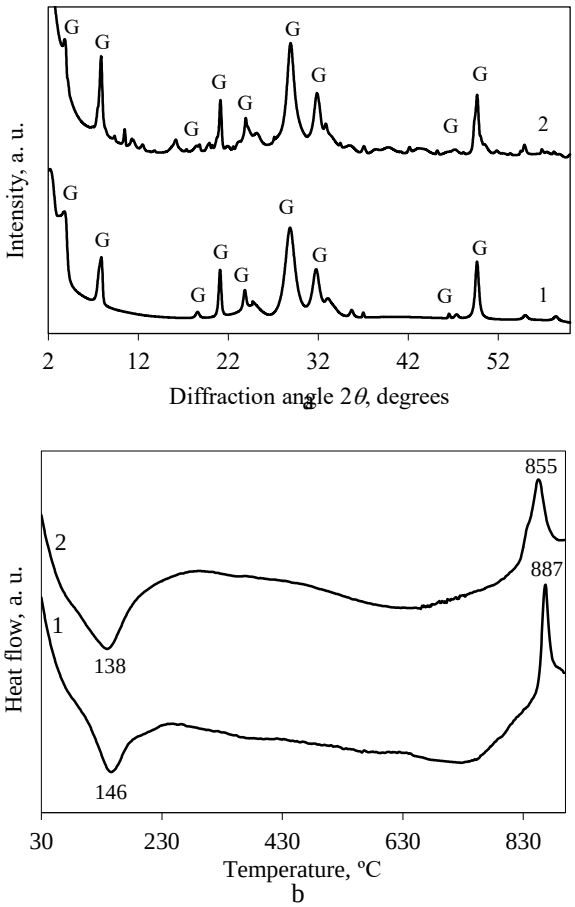

Figure 3.42. X-ray diffraction patterns (a) and DSC curves (b) of gyrolite synthesized after 48 h at 200 °C in the CaO-SiO_2-H_2O system: 1 the curve before adsorption, 2 the curve after adsorption. Indexes: G denotes gyrolite.

X-ray powder diffraction analysis showed that the structure of gyrolite did not change during the adsorption process. In the X-ray diffraction pattern, the most characteristic peak (the *d*-spacing of 2.273 nm) of gyrolite was identified. This principal reflection did not change over the duration of the adsorption process (see Figure 3.42., a, curve 2). In the DSC curve, the same thermal effects (the

endothermic effect at 138 °C of water dehydration and the exothermic effect at 855 °C of recrystallization to wollastonite) were identified (see Figure 3.42., b, curve 2) as in pure gyrolite (see Figure 3.42., b, curve 1). It should be noted that gyrolite substituted with Zn^{2+} ions recrystallizes into wollastonite at lower temperatures (855 °C).

After the adsorption experiment, gyrolite powder was dried and poured into decarbonized water for the leaching test. It was determined that zinc ions concentration in the solution after 120 min at 25 °C did not exceed 0.1%. Thus the adsorption process in the alkaline solution is irreversible.

Thus our research allows to state that the cation exchange reactions are specific of the chemisorption process. In order to determine the kinetic parameters of adsorption in the alkaline solution, kinetic models were applied for the adsorption process of the Zn^{2+} ions with gyrolite.

By using pseudo first-order kinetic rate equation in a linear form (Equation 2.7), the equilibrium adsorption capacity ($\Sigma X_{e(exp)}$) and the first order constant k_1 (1/min) was calculated from the slope and the intercept plot of $\log(\Sigma X_{e(exp)} - X_t)$ versus t. It was observed that the pseudo first-order model did not fit well because the calculated $\Sigma X_{e(cal)}$ value disagreed with the experimental $\Sigma X_{e(exp)}$ value, and the value of correlation coefficient (R^2) was as low as 0.557 (Table 3.13.).

Table 3.13.The kinetic parameters of the pseudo first- and pseudo second-order kinetic models of Zn^{2+} ions adsorption on gyrolite in alkaline solution

$\Sigma X_{e(exp)}$	Pseudo first-order			Pseudo second-order		
	k_1, 1/min	$\Sigma X_{e(cal.)}$, mg/g	R^2	k_2, g/mg·min	$\Sigma X_{e(cal)}$, mg/g	R^2
29.120	0.088	1.265	0.557	1.176	29.154	1.000

$\Sigma X_{e(exp)}$ represents the equilibrium adsorption capacity, mg/g, obtained from experimental data; $\Sigma X_{e(cal)}$ is the equilibrium adsorption capacity, mg/g, calculated by using equations (2.7) and (2.9) of kinetic models.

By using the pseudo second order kinetics equation (Equation 2.9), the equilibrium adsorption capacity ($\Sigma X_{e(cal)}$) and second-order constants k_2 (g/mg·min) were calculated from the slope and intercept of plot t/X_t versus t (Figure 3.43.). The values of the calculated $\Sigma X_{e(cal)}$ and experimental $\Sigma X_{e(exp)}$ are presented in Table 3.13.

Agreement between $\Sigma X_{e(exp)}$ experimental and $\Sigma X_{e(cal)}$ calculated values for the pseudo second order model was observed. Also, the correlation coefficient (R^2) for the second order increases to 1 and the adsorption rate constant (k_2) is equal to 1.176.

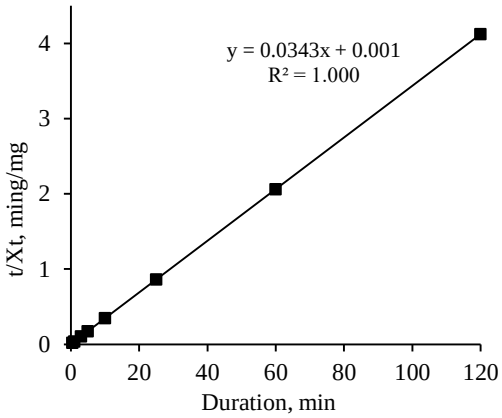

Figure 3.43. Pseudo-second order kinetic curve of Zn^{2+} ions adsorption on gyrolite in alkaline solution.

Hence, the pseudo-second order model was followed by adsorption kinetics, and it was suggested that the process of adsorption in the alkaline solution is chemisorption. Thus it is recommended to use gyrolite when pH of adsorptive is alkaline because when pH is acidic, this compound recrystallizes into other compounds and cannot be used as an adsorbent in acidic solution.

It is also important to ascertain the changes of the gyrolite structure properties by using different crystallinity above mentioned compound samples for the adsorption process. For this reason, gyrolite was synthesized after 32, 48, 72, 120 and 168 h at 200 °C (C/S = 0.66) and used for the zinc ions removal from alkaline (pH ~9.0) solution.

It was determined that in the CaO and $SiO_2 \cdot nH_2O$ mixture, after 32 h of isothermal curing, intermediate compounds (C-S-H(I), Z-phase) recrystallize to the main synthesis product, gyrolite, the stoichiometric composition of which corresponds to the molar ratio of the initial mixture (C/S ~0.66). In the X-ray diffraction pattern, the diffraction maximums most characteristic of the latter compound (the *d*-spacing of 2.273, 1.126, 0.844, 0.420, 0.365, 0.280, and 0.224 nm) are clearly seen, and no other peaks are identified (Figure 3.44., curve 1). The crystallinity of gyrolite increases by prolonging the isothermal curing duration from 32 to 168 h when the intensities of the diffraction peaks significantly increase (Figure 3.44., curves 2–5).

Thus gyrolite does not regroup into related compounds and remains stable when the hydrothermal synthesis duration varies from 32 h to 168 h at 200 °C, although its structure changes by prolonging the duration of synthesis. For this reason, the effect of the gyrolite structure properties on zinc ion adsorption was investigated during the next stage of the experiment.

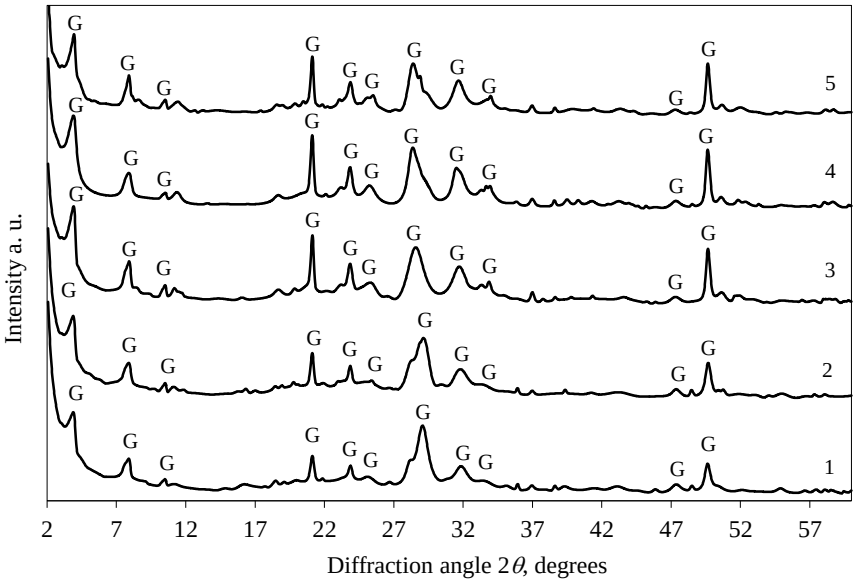

Figure 3.44. X-ray diffraction patterns of gyrolite synthesized in the $CaO\text{-}SiO_2\text{-}H_2O$ system with varying durations of hydrothermal synthesis at 200 °C, in h: 1 at 32 h; 2 at 48 h; 3 at 72 h; 4 at 120 h; 5 at 168 h. Index: G denotes gyrolite.

It was determined that after 30 s of adsorption, about 88% (26.48 mg Zn^{2+}/g) of zinc ions were intercalated into the structure of gyrolite which was synthesized for 32 h (see Figure 3.45., a, curve 1). Meanwhile, the uptake of these ions into the orderly structure of gyrolite was much slower: 71% (21.36 mg Zn^{2+}/g) of zinc ions were intercalated into gyrolite synthesized for 72 h and only 56% (21.36 mg Zn^{2+}/g) were intercalated into long-term synthesized (168 h) gyrolite. In addition, the adsorbent synthesis conditions have an effect on the total amount of adsorbed zinc ions in solution. For this reason, the maximum amount of adsorbed Zn^{2+} ions was two times higher when using gyrolite synthesized for 32 h than when using long-term synthesized (168 h) gyrolite (see Figure 3.45., a, curve 5).

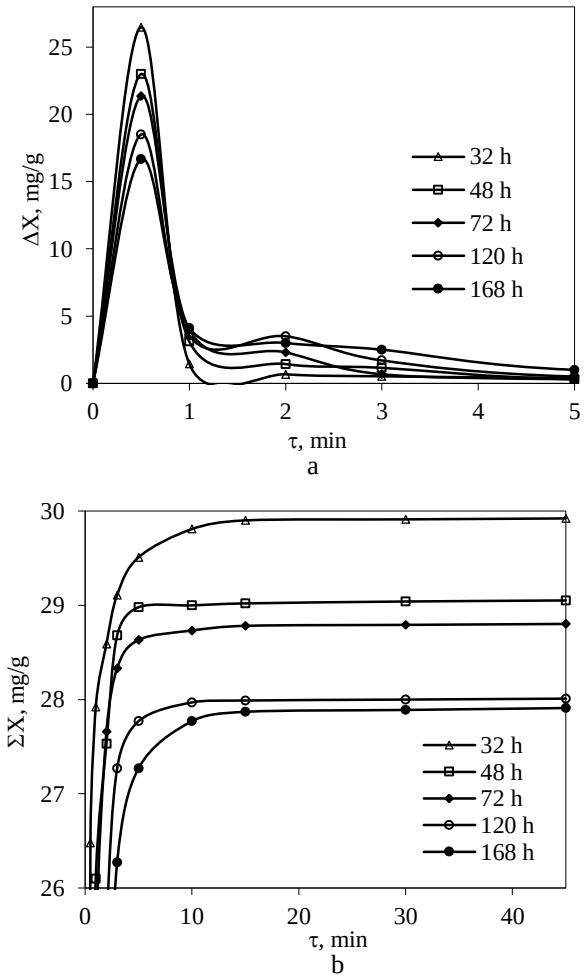

Figure 3.45. Differential (a) and integral (b) kinetic curves during Zn^{2+} ion adsorption process by using different crystallinity gyrolite samples.

It should be noted that during the intrusion of zinc ions into the gyrolite structure, calcium ions are released from the crystal lattice of the adsorbent into the solution. Most of the Ca^{2+} ions were released during the first minutes, and their amount slightly varies when the process of adsorption is prolonged (Figure 3.46.). It was determined that the largest amount of Ca^{2+} ions (15.09 mg Ca^{2+}/g) was released into the solution when using gyrolite synthesized for 32 h (see Figure 3.46., b, curve 1). As expected, the lowest amount of Ca^{2+} ions (13.21 mg Ca^{2+}/g) was released when using gyrolite synthesized for one week (see Figure 3.46., a, curve 5).

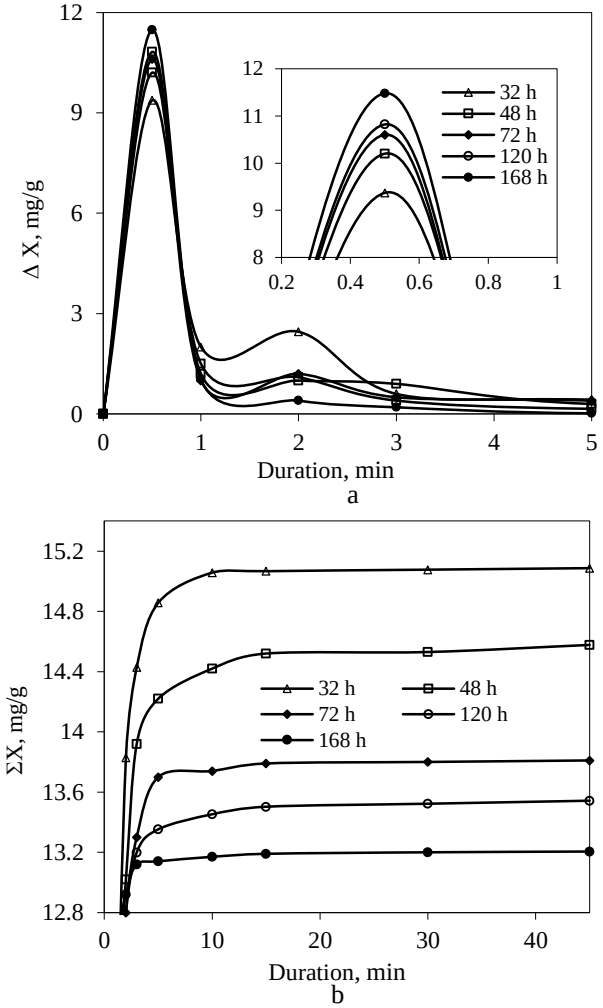

Figure 3.46. Differential (a) and integral (b) kinetic curves during Ca^{2+} ion desorption process when using different crystallinity gyrolite samples.

It was determined that Zn^{2+} ions entered into the gyrolite structure via substitution (gyrolite-Ca^0 + Zn^{2+}↔ gyrolite-Zn^0 + Ca^{2+}) and addition reactions. It was calculated that the zinc ions substituted 5.42% of Ca^{2+} ions in gyrolite synthesized for 32 h and for 3.87% when the duration of the adsorbent synthesis was extended (168 h), whereas the rest of these ions entered into the structure of gyrolite being involved in addition interaction.

It should be noted that the reactions took place during the adsorption process, and they are not reversible. In order to confirm this fact, after the adsorption process (25 °C, 45 min) gyrolite with substituted zinc ions was dried and immersed in distilled water. It was proven that the above mentioned ions did not appear in the solution after 45 min at 25 °C. Thus, our research allows us to state that the adsorption process is specific to the chemisorption. In order to determine the

adsorption kinetic parameters, kinetics models were applied to the reactions of Zn^{2+} ions by gyrolite.

By using a pseudofirst-order kinetic rate equation (Equation 2.7), the amount of adsorbed ions ($\Sigma X_{e(cal)}$) and the first-order constants k_1 (min^{-1}) were calculated from the slope and intercept plot of $\log(\Sigma X_{e(exp)} - X_t)$ versus t (Figure 3.47., a). It was observed that the pseudofirst-order model did not fit well because the calculated $\Sigma X_{e(cal)}$ values disagreed with the experimental $\Sigma X_{e(exp)}$ values, and the values of the correlation coefficient (R^2) were very low (from 0.781 to 0.8) (Table 3.14.).

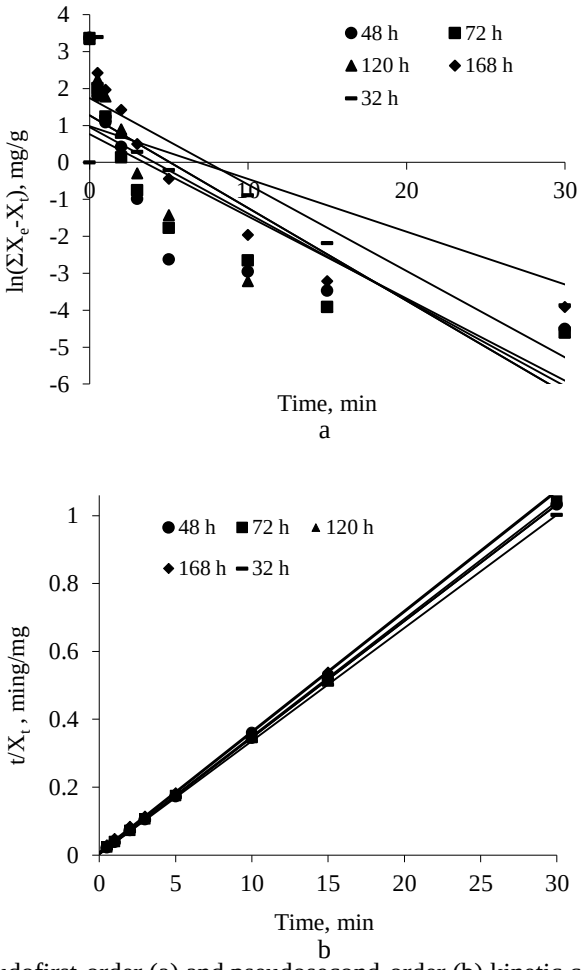

Figure 3.47. Pseudofirst-order (a) and pseudosecond-order (b) kinetic curves of Zn^{2+} ions adsorption on gyrolite synthesized in the $CaO\text{-}SiO_2\text{-}H_2O$ system with varying duration of hydrothermal synthesis at 200 °C.

By using the pseudosecond-order kinetic model (Equation 2.9), the amounts of adsorbed ions ($\Sigma X_{e(exp)}$) and the second-order constants k_2 ($g \cdot mg^{-1} \cdot min^{-1}$) were calculated from the slope and intercept of plot t/X_t versus t (Figure 3.47., b). The values of the calculated $\Sigma X_{e(cal)}$ and the experimental $\Sigma X_{e(exp)}$ are represented in Table 3.14.

Table 3.14. The kinetic parameters of the pseudo first- and pseudo second-order kinetic models of Zn^{2+} ions adsorption on gyrolite in alkaline solution

Duration of synthesis, h	$\Sigma X_{e(exp.)}$	The pseudo first-order			The pseudo second-order		
		K_1	$\Sigma X_{e(cal.)}$	R^2	K_2	$\Sigma X_{e(cal.)}$	R^2
32	29.923	0.227	2.719	0.781	0.446	29.940	1.000
48	29.052	0.222	2.154	0.659	0.435	29.154	1.000
72	28.803	0.233	2.592	0.718	0.352	28.901	0.999
120	28.010	0.250	3.579	0.736	0.225	28.169	0.999
168	27.910	0.233	5.679	0.800	0.142	28.089	0.999

Note: $\Sigma X_{e(exp)}$ = the amount of adsorbed ions, mg·g^{-1}, obtained from experimental data;$\Sigma X_{e(cal)}$ = amount of adsorbed ions, mg·g^{-1}, calculated by using Eq. (2.7) and (2.9) of kinetic models.

An agreement between $\Sigma X_{e(exp)}$ experimental and $\Sigma X_{e(cal)}$ calculated values for the pseudosecond-order model was obtained. Also, the adsorption rate constant (k_2) decreased from 0.446 to 0.142 by prolonging the duration of synthesis from 32 h to 168 h. The calculated values of the adsorption rate constant confirmed the experimental data: the synthesis conditions of gyrolite affect its adsorption capacity for zinc ions because the adsorption process takes place under more difficult conditions when using gyrolite with a more orderly structure.

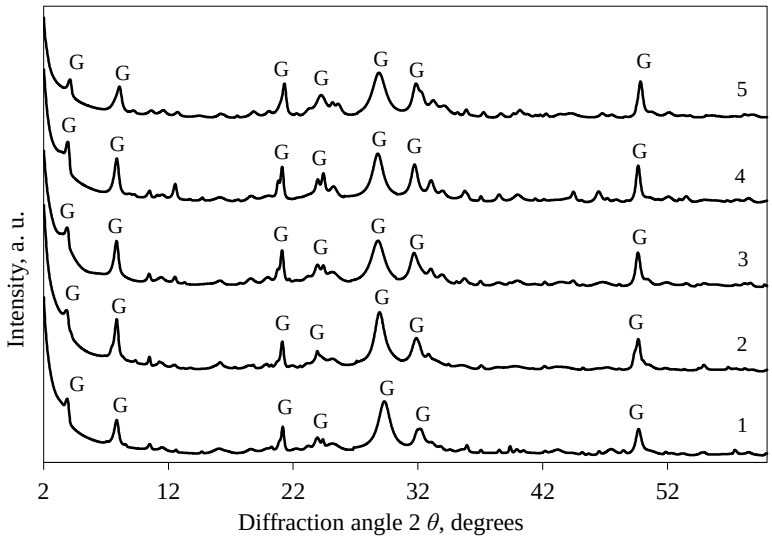

Figure 3.48. X-ray diffraction patterns of gyrolite, synthesized in the $CaO\text{-}SiO_2\text{-}H_2O$ system after the adsorption process. Duration of hydrothermal synthesis at 200 °C, in h: 1 at 32 h; 2 at 48 h; 3 at 72 h; 4 at 120 h; 5 at 168 h.

In order to identify the stability of gyrolite, the products of adsorption were characterized by X-ray powder diffraction analysis (Figure 3.48.). It was determined

that the structure of gyrolite remained stable because the most characteristic peak (*d*-spacing = 2.273 nm) did not change over the varying durations of the adsorption reactions (Figure 3.48.).

It was determined that, after the adsorption process, the crystallite size and diffraction peak area (001) of gyrolite decreased by about 51 nm and 19 a. u., respectively, in comparison with the results after synthesis (Figure 3.49., a, b).

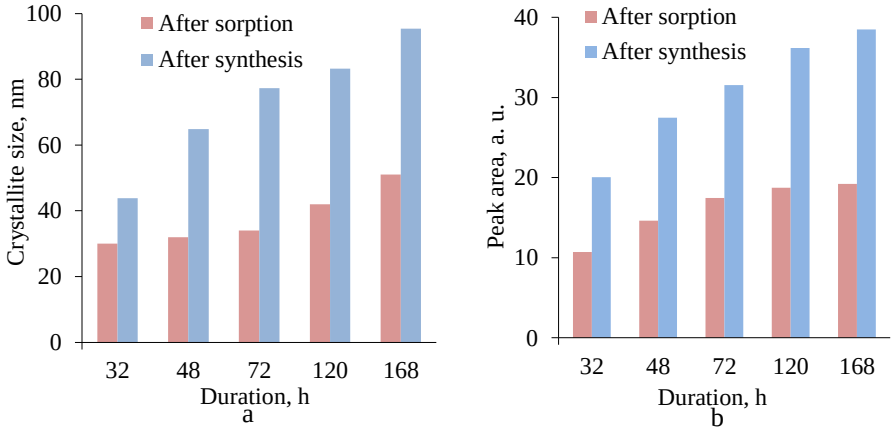

Figure 3.49. Dependence of the crystallite size (a) and the diffraction peak area (001) (b) of gyrolite on the duration of hydrothermal synthesis before and after the adsorption process.

This change is attributed to the degree of release of Ca^{2+} ions (from 5.42% after 32 h, to 3.87% after 168 h) from the gyrolite solid into the solution and the degree of Zn^{2+} ion intercalation into the orderly structure of gyrolite. This data confirmed the previous results that Zn^{2+} ions entered the gyrolite structure via substitution and addition reactions.

Table 3.15. Specific surface area (S_{BET}) parameters of gyrolite, synthesized in the $CaO\text{-}SiO_2\text{-}H_2O$ system, after adsorption of Zn^{2+} ions process

Duration of synthesis, h	Sample mass m, g	BET equation constants		Capacity of monolayer $X_m = 1/(S+I)$, g	Specific surface area S_{BET}, m^2/g	Constant $C_{BET} = 1/(I \cdot X_m)$	Reliability coefficient R^2
		Slope $S=tg\alpha$	Intercept I				
32	0.039	1205.8	0.634	0.0008	75.03	1903.19	0.9988
48	0.057	735.1	0.230	0.0014	83.93	3204.22	0.9988
72	0.039	2016.0	15.011	0.0005	44.45	135.30	0.9982
120	0.044	2061.2	8.454	0.0005	38.57	244.82	0.9993
168	0.047	1897.6	10.559	0.0005	39.33	180.71	0.9992

It was noted that Zn^{2+} ions have influence both on the gyrolite structure and the specific surface area (Table 3.15.). It was determined that after the adsorption experiment, the S_{BET} value of gyrolite (synthesized after 32 h) was equal to 75.03 m^2/g. By using gyrolite synthesized after 48 h, S_{BET} of this compound, interfered with Zn^{2+} ions, also increased to 83.93 m^2/g. It should be noted that S_{BET} being characteristic for gyrolite, interfered with Zn^{2+} ions, decreased more than two times (44.45 m^2/g) already by using gyrolite synthesized after 72 h. Besides, this tendency was also observed by using gyrolite synthesized after 120 h and 168 h because S_{BET} after adsorption experiment was equal to 38.57 m^2/g and 39.33 m^2/g, respectively. Meanwhile, in a pure system, before adsorption process, after 32 h of synthesis S_{BET} of gyrolite were 82.07 m^2/g and, after 168 h of treatment, it went down to 46.0 m^2/g (132).

3.5 Technological Recommendations for Application of AlF_3 Production Waste

Based on the data obtained in this research, a principal technological scheme for the AlF_3 production waste neutralization or utilization has been designed (Figure 3.50.).

The obtained experimental data showed that the reduction of mobility of F^- ions from AlF_3 production waste can be carried out in two ways by using Ca-containing compounds. In both cases, the required silica gel and the Ca-containing compound are weighed with weight dispensers (3) and supplied to the mixer/adsorber (5), in which, the required amount of water is added from the reservoir (2) by using the volumetric dispenser (4). By choosing the first neutralization method, the prepared suspension is kept for 1 h at 25 °C temperature in the mixer/adsorber (5). After that, the product is placed into a filtration unit (7) and, later, into a pulverous dryer (9), where 0.75–1.00 mm diameter pellets with a moisture content of 1.5–2% are produced. By using the second method for the utilization of AlF_3 production waste, the obtained suspension is supplied with the pump to an autoclave (6). Stable compounds are formed during the hydrothermal treatment of AlF_3 production waste with CaO in the autoclave (6), when the saturated water temperature is 200 °C. After the hydrothermal treatment, the product is placed into a filtration unit and, finally, into a pulverous dryer.

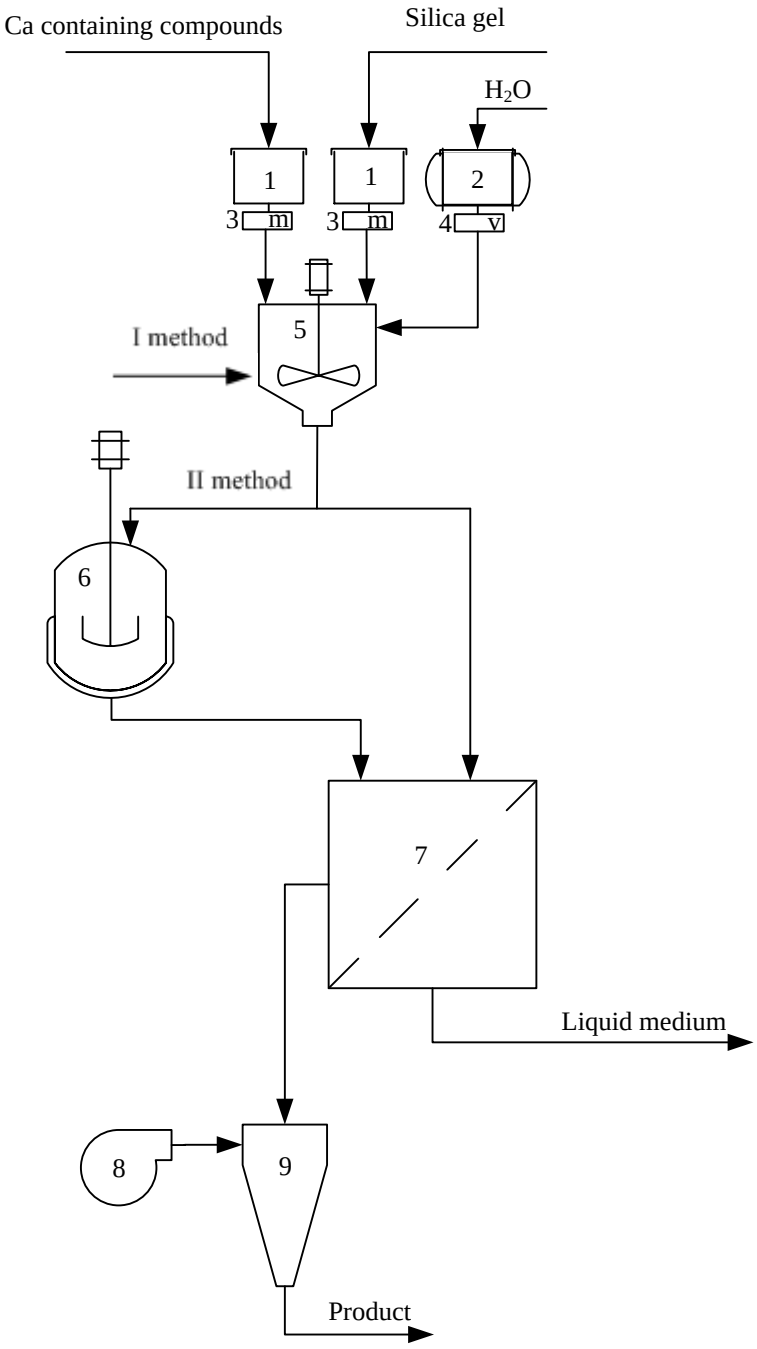

Figure 3.50. Principal technological scheme of AlF_3 production waste neutralization or/and utilization: 1 shows bunkers of raw materials; 2 is the reservoir of water; 3 are the weight dispensers; 4 is the volume dispenser; 5 is the mixer/adsorber; 6 is the autoclave; 7 is the unit of filtration; 8 is the heater; 9 is pulverous dryer.

Conclusions

1. It was determined that dry waste from AlF_3 production consists of 77.67% silicon dioxide, 8.82% F^-, and 4.08% Al_2O_3. It was found that under static elution conditions (at 25, 50, 75, and 95 °C temperatures for 1 h when water to solid ratio were 10 and 500) only 0.5–0.6 wt. % of F^- ions are released into the liquid medium and other ions are adsorbed by the main compound – amorphous silica. In addition, the ratio of AlF_3 production waste to the liquid medium affects the stability of $AlF_3 \cdot 3H_2O$ which decomposes when w/s is equal to 500 at 25 °C within 1 h. Also, it was found that CaO additive reduces the mobility of fluoride ions by combining them into CaF_2.
2. It was found that in the mixtures with AlF_3 production waste, the compound formation mechanism during low base calcium silicate hydrate hydrothermal treatment occurs differently than in pure mixtures. It was estimated that in mixtures when the molar ratio of CaO/SiO_2 is equal to 0.55 and 0.66, the main synthesis compound – gyrolite – formed faster than in pure mixtures. Besides the main compound in the AlF_3 production waste containing F^- ions, $AlF_3 \cdot 3H_2O$, decomposes, and new compounds are formed: CaF_2 and hydrogarnet.
3. It was found that in higher basicity mixtures (CaO/SiO_2; molar ratio 0.83 and 1.0) calcium silicate hydrate, compounds with a smaller CaO/SiO_2 ratio were formed, as was expected, based on the molar ratio of the initial mixture CaO/SiO_2: when CaO/SiO_2 molar ratio is 0.83, gyrolite is the predominated product, and with CaO/SiO_2molar ratio of 1.0, the above mentioned compound formed together with 1.13 nm tobermorite. Moreover, calcium fluoride and hydrogarnet formed together with synthesis products. Thermodynamic calculations confirmed that in the mixture with a smaller ratio (C/S = 0.55 and 0.66), gyrolite (ΔG = -1.20 kJ) is the main compound, and, by increasing CaO/SiO_2 molar ratio from 0.83 to 1.0, it gradually recrystallizes into 1.13 nm tobermorite and xonotlite in pure mixtures.
4. It was determined that the thermal stability of synthetic calcium silicate hydrates and the formed CaF_2 depends on the mineralogical composition of the synthesized compounds because when the main product of synthesis is gyrolite, (CaO/SiO_2 = 0.55 and 0.66), hydrothermally formed CaF_2 remains stable throughout the entire explored temperature range. Meanwhile, when the main product of synthesis was 1.13 nm tobermorite, (CaO/SiO_2 = 0.83 and 1.0), CaF_2 fully recrystallized into cuspidine at 1000 °C temperature.
5. It was found that the pH values of the adsorption solution have a significant importance for Zn^{2+} ion adsorption (c_{Zn2+} = 0.3 g/dm^3) process on gyrolite, because, after 30 s, 95% of Zn^{2+} ions (28.50 mg Zn^{2+}/g) intercalated into the gyrolite structure in the alkaline solution (pH ~9.0), whereas in the acidic solution (pH ~5.6), only 68% score was achieved (20.43 mg Zn^{2+}/g). It is recommended to use gyrolite when the pH of the adsorptive is alkaline because in a solution with a lower pH value (~5.6), this compound recrystallizes into other compounds. It was determined that gyrolite adsorption capacity also depends on the hydrothermal synthesis duration because by prolonging the

duration of the synthesis from 32 h to 168 h, the adsorption capacity of gyrolite decreases from 99% (29.92 mg Zn^{2+}/g) to 93% (27.91 mg Zn^{2+}/g), respectively. It was found that the adsorption reactions of gyrolite in the alkaline solution were specific to the chemisorption process, which was confirmed by the pseudo second-order model.

6. The principal technological scheme has been designed for AlF_3 production waste neutralization or utilization by using calcium-containing compounds under static (25 °C) or hydrothermal (200 °C) conditions.

References

1. BAHRAMI, A., SOLTANI, N., PECH-CANUL, M.I., GUTIÉRREZ, C.A. (2015). Development of Metal-Matrix Composites from Industrial/Agricultural Waste Materials and Their Derivatives. In: *Critical Reviews in Environmental Science and Technology*. Vol. 3389, p. 1–66. ISSN: 1547-6537.

2. JESWANI, H.K., AZAPAGIC, A. (2016). Assessing the Environmental Sustainability of Energy Recovery from Municipal Solid Waste in the UK. *Waste Management (New York, N.Y.)*. In press, available online as of 20 February 2016, doi: 10.1016/j.wasman.2016.02.010. ISSN: 0956-053X.

3. CHEN, P., XIE, Q., MIN, M., ZHOU, W., LIU, Y., WANG, Y., CHENG, Y., LI, K., RUAN, R. (2016). Utilization of Municipal Solid and Liquid Wastes for Bioenergy and Bioproducts Production. In: *Bioresource Technology*. In press, available online as of 5 March 2016. doi:10.1016/j.biortech.2016.02.094. ISSN: 0960-8524.

4. YANG, T., LI, Y., GAO, J.H.C., CHEN, B., ZHANG, L., WANG, X., ZHAO, Y., XI, B., LI, X. (2015). Performance of Dry Anaerobic Technology in the Co-Digestion of Rural Organic Solid Wastes in China. In: *Energy*. Vol. 93, p. 2497–2502. ISSN: 0360-5442.

5. APRILIA, A., TEZUKA, T., SPAARGAREN, G. (2013). Inorganic and Hazardous Solid Waste Management: Current Status and Challenges for Indonesia. In: *Procedia Environmental Sciences*. Vol. 17, p. 640–647. ISSN: 1878-0296.

6. ALEMAYEHU, E. (2004). *Solid and Liquid Waste Management*. Lecture notes by Jimma University, USAID.

7. SENER, S., SENER, E., KARAGÜZEL, R. (2011). Solid Waste Disposal Site Selection with GIS and AHP Methodology: A Case Study in Senirkent-Uluborlu (Isparta) Basin, Turkey. In: *Environmental Monitoring and Assessment*. Vol. 173, no. 1–4, p. 533–554. ISSN: 0167-6369.

8. ZAKHAROV, Y., BONDAREVA, L. (2015). Simulation of Domestic and Industrial Wastewater Disposal in Flooded Mine Workings. In: *Procedia Engineering*. Vol. 117, no. 1, p. 394–401. ISSN: 1877-7058.

9. BARAN, B., MAMIS, M.S., ALAGOZ, B.B. (2016). Utilization of Energy from Waste Potential in Turkey as Distributed Secondary Renewable Energy Source. In: *Renewable Energy*. Vol. 90, p. 493–500. ISSN: 0960-1481.

10. YESILNACAR, M.I., SÜZEN, M.L., KAYA, B.S., DOYURAN, V. (2012). Municipal Solid Waste Landfill Site Selection for the City of Şanliurfa-Turkey: an Example Using MCDA Integrated with GIS. In: *International Journal of Digital Earth*. Vol. 5, no. 2, p. 147–164. ISSN: 1753-8955.

11. GORSEVSKI, P.V., DONEVSKA, K.R., MITROVSKI, C.D., FRIZADO, J.P. (2012). Integrating Multi-Criteria Evaluation Techniques with Geographic Information Systems for Landfill Site Selection: A case study using ordered weighted average. In: *Waste Management*. Vol. 32, no. 2, p. 287–296. ISSN: 0956-053X.

12. PAP, N., PONGRÁCZ, E., MYLLYKOSKI, L., KEISKI, R. (2004). Waste Minimization and Utilization in the Food Industry: Processing of Arctic Berries, and Extraction of Valuable Compounds from Juice Processing By-Products. In: *Proceedings of the Waste Minimization and Resources Use Optimization Conference*, p. 159–168.

13. USEPA. Integrating Pollution Prevention – Getting Started. (2010). In: *Pollution Prevention*, p. 1–121.

14. *European Contributions to the Commission Consultation on the EU Waste*

Management Targets Review. (2013).

15. AKHTAR, M.N. (2014). Prospective Assessment for Long-Term Impact of Excessive Solid Waste. In: *International Journal of Advancement in Earth and Environmental Sciences.* In: Vol. 2, no. 2, p. 39–45. ISSN: 2321 – 9149.

16. LUNA-CAÑAS, L.M., RÍOS-REYES, C.A., QUINTERO-ORTÍZ, L.A. (2014). Recycling of Agroindustrial Solid Wastes as Additives in Brick Manufacturing for Development of Sustainable Construction Materials. In: *Dyna*. Vol. 81, no. 188, p. 34–41. ISSN: 0012-7353.

17. BADNERA, R., ROAD, A.B., AMRAVATI, M.S. (2013). Advantages of Waste-Phosphogypsum in Concrete. In: *International Journal of Scientific Research*. Vol. 2, no. 2.277, p. 153–154. ISSN: 2277-8179.

18. SAFIUDDIN, M., JUMAAT, M.Z., SALAM, M.A., ISLAM, M.S., HASHIM, R. (2010). Utilization of Solid Wastes in Construction Materials. In: *International Journal of Physical Sciences*. Vol. 5, no. 13, p. 1952–1963. ISSN: 1992-1950.

19. KARLSTRÖM, J. (1970). *Reactor Model for Production of Aluminum Fluoride*. No. 1966.

20. DREVETON, A. (2014). Economic Aspects of Utilizing Fluosilicic Acid as Raw Material for the Manufacture of Hydrofluoric Acid and Aluminium Fluoride. In: *Procedia Engineering*. Vol. 83, p. 279–285. ISSN: 1877-7058.

21. KRYSZTAFKIEWICZ A., RAGER B., MAIK M. (1996). Silica Recovery from Waste Obtained in Hydrofluoric Acid and Aluminum Fluoride Production from Fluosilicic Acid. In: *Journal of Hazardous Materials*. Vol. 48, p. 31–49. ISSN: 0304-3894.

22. VAIČIUKYNIENĖ D., VAITKEVIČIUS V., KANTAUTAS A., SASNAUSKAS, V. (2012). Utilization of By-Product Waste Silica in Concrete-Based Materials. In: *Materials Research*. Vol. 15, no. 4, p. 561. ISSN: 1980-5373.

23. IDRIS, A., SAED, K. (2003). Possible Utilization of Silica Gel Sludge for the Removal of Phenol from Aqueous Solutions: Laboratory Studies. In: *Environmentalist*.. Vol. 23, no. 4, p. 329–334. ISSN: 2194-5411.

24. ALDACO, R., IRABIEN, A., LUIS, P. (2005). Fluidized Bed Reactor for Fluoride Removal. In: *Chemical Engineering Journal*. Vol. 107, no. 1–3, p. 113–117. ISSN: 1385-8947.

25. PAUDYAL, H., PANGENI, B., NATH GHIMIRE, K., INOUE, K., OHTO, K., KAWAKITA, H., ALAM, S. (2012). Adsorption Behavior of Orange Waste Gel for Some Rare Earth Ions and Its Application to the Removal of Fluoride from Water. In: *Chemical Engineering Journal*. Vol. 195–196, p. 289–296. ISSN: 1385-8947.

26. ISLAM, M., MISHRA, P.Ch., PATEL, R. (2011). Fluoride Adsorption from Aqueous Solution by a Hybrid Thorium Phosphate Composite. In: *Chemical Engineering Journal*. Vol. 166, no. 3, p. 978–985. ISSN: 1385-8947.

27. SINGH, J., SINGH, P., SINGH, A. (2014). Fluoride Ions vs. Removal Technologies: A Study. *Arabian Journal of Chemistry*. In press, available online as of 4 July 2014. doi: 10.1016/j.arabjc.2014.06.005. ISSN: 1878-5352.

28. JADHAV, S.V., BRINGAS, E., YADAV, G.D., RATHOD, V.K., ORTIZ, I., MARATHE, K.V. (2015). Arsenic and Fluoride Contaminated Groundwaters: a Review of Current Technologies for Contaminants Removal. In: *Journal of Environmental Management*. Vol. 162, p. 306–325. ISSN: 0301-4797.

29. MOHAPATRA, M., ANAND, S., MISHRA, B.K., GILES, D.E., SINGH, P. (2009).

Review of Fluoride Removal from Drinking Water. In: *Journal of Environmental Management*. Vol. 91, no. 1, p. 67–77. ISSN: 0301-4797.

30. KETTUNEN, R., KESKITALO, P. (2000). Combination of membrane technology and limestone filtration to control drinking water quality. In: *Desalination*. Vol. 131, p. 271–283. ISSN: 0011-9164.

31. DENG, L., LIU, Y., HUANG, T., SUN, T. (2016). Fluoride Removal by Induced Crystallization Using Fluorapatite/Calcite Seed Crystals. In: *Chemical Engineering Journal*. Vol. 287, p. 83–91. ISSN: 1385-8947.

32. SHEN, J., SCHIFER, A.I. (2015). Factors Affecting Fluoride and Natural Organic Matter (NOM) Removal from Natural Waters in Tanzania by Nanofiltration/Reverse Osmosis. In: *Science of the Total Environment*. Vol. 527–528, p. 520–529. ISSN: 0048-9697.

33. AOUDJ, S., KHELIFA, A., DROUICHE, N., BELKADA, R., MIROUD, D. (2015). Simultaneous Removal of Chromium (VI) and Fluoride by Electrocoagulation–Electroflotation: Application of a Hybrid Fe-Al Anode. In: *Chemical Engineering Journal*. Vol. 267, p. 153–162. ISSN: 1385-8947.

34. REARDON, E.J., WANG, Y.A. (2000). Limestone Reactor for Fluoride Removal from Wastewaters. In: *Environmental Science and Technology*. Vol. 34, no. 15, p. 3247–3253. ISSN: 1520-5851.

35. JADHAV, S.V., GADIPELLY, C.R., MARATHE, K.V., RATHOD, V.K. (2014). Treatment of Fluoride Concentrates from Membrane Unit Using Salt Solutions. In: *Journal of Water Process Engineering*. Vol. 2, p. 31–36. ISSN: 2214-7144.

36. Xinhua, X.U., Xiangfeng, Z.H.U. (2004). Treatment of Refectory Oily Wastewater by Electro-Coagulation Process. In: *Chemosphere*. Vol. 56, no. 10, p. 889–894. ISSN: 0045-6535.

37. KHANDEGAR, V., SAROHA, A.K. (2013). Electrocoagulation for the Treatment of Textile Industry Effluent – a Review. In: *Journal of Environmental Management*. Vol. 128, p. 949–963. ISSN: 0301-4797.

38. HAKIZIMANA, J.N., GOURICH, B., VIAL, Ch., DROGUI, P., OUMANI, A., NAJA, J., HILALI, L. (2016). Assessment of Hardness, Microorganism and Organic Matter Removal from Seawater by Electrocoagulation as a Pretreatment of Desalination by Reverse Osmosis. In: *Desalination*. Vol. 393, p. 90–101. ISSN: 0011-9164.

39. PRICA, M., ADAMOVIC, S., DALMACIJA, B., RAJIC, L., TRICKOVIC, J., RAPAJIC, S., BECELIC-TOMIN, M. (2015). The Electrocoagulation/Flotation Study: The Removal of Heavy Metals from the Waste Fountain Solution. In: *Process Safety and Environmental Protection*. Vol. 94, p. 262–273. ISSN: 0957-5820.

40. HU, C.Y., LO, S.L., KUAN, W.H., LEE, Y.D. (2005). Removal of Fluoride from Semiconductor Wastewater by Electrocoagulation-Flotation. In: *Water research*. Vol. 39, no. 5, p. 895–901. ISSN: 0043-1354.

41. ZUO, Q., CHEN, X., LI, W., CHEN, G. (2008). Combined Electrocoagulation and Electroflotation for Removal of Fluoride from Drinking Water. In: *Journal of Hazardous Materials*. Vol. 159, no. 2–3, p. 452–457. ISSN: 0304-3894.

42. SHEN, F., CHEN, X., GAO, P., CHEN, G. (2003). Electrochemical Removal of Fluoride Ions from Industrial Wastewater. In: *Chemical Engineering Science*. Vol. 58, no. 3–6, p. 987–993. ISSN: 0009-2509.

43. ESKANDARPOUR, A., ONYANGO, M.S., OCHIENG, A., ASAI, S. (2008). Removal of Fluoride Ions from Aqueous Solution at Low pH Using Schwertmannite. In: *Journal of*

Hazardous Materials. Vol. 152, no. 2, p. 571–579. ISSN: 0304-3894.

44. VISWANATHAN, N., MEENAKSHI, S. (2009). Role of Metal Ion Incorporation in Ion Exchange Resin on the Selectivity of Fluoride. In: *Journal of Hazardous Materials*.. Vol. 162, no. 2–3, p. 920–930. ISSN: 0304-3894.

45. LUO, F., INOUE, K. (2004). The Removal of Fluoride Ion by Using Metal(III)-Loaded Amberlite Resins. In: *Solvent Extraction and Ion Exchange*. Vol. 22, no. 2, p. 305–322. ISSN: 1532-2262.

46. LI, G., ZHAOB, Z., LIUA, J., JIANGA, G. (2011). Effective Heavy Metal Removal from Aqueous Systems by Thiol Functionalized Magnetic Mesoporous Silica. In: *Journal of Hazardous Materials*. Vol. 192, p. 277–283. ISSN: 0304-3894.

47. MOTSA, M.M., THWALA, J.M., MSAGATI, T.A.M., MAMBA B.B. (2011). The Potential of Melt-Mixed Polypropylene-Zeolite Blends in the Removal of Heavy Metals from Aqueous Media. In: *Physics and Chemistry of the Earth*. Vol. 36, p. 1178–1188. ISSN: 1474-7065.

48. BABEL, S., KURNIAWAN, T.A. (2003). Low-cost Adsorbents for Heavy Metals Uptake from Contaminated Water: a Review. *Journal of Hazardous Materials*.. Vol. B97, p. 219–243. ISSN: 0304-3894.

49. BUEKENS A., ZYAYKINA N.N. (2005). Adsorbents and Adsorption Processes for Pollution Control. In: *Journal of Pollution Control Technologies*. Vol. 2.

50. SALAHUDEEN, N., AHMED, A.S., AL-MUHTASEB, A.H., DAUDA, M., WAZIRI, S.M., JIBRIL, B.Y., AL-SABAHI, J. (2015). Synthesis, Characterization and Adsorption Study of Nano-Sized Activated Alumina Synthesized from Kaolin Using Novel Method. In: *Powder Technology*. Vol. 280, p. 266–272. ISSN: 0032-5910.

51. HE, Z., LIU, R., XU, J., LIU, H., QU, J. (2015). Defluoridation by Al-Based Coagulation and Adsorption: Species Transformation of Aluminum and Fluoride. In: *Separation and Purification Technology*..Vol. 148, p. 68–75. ISSN: 1383-5866.

52. CHEN, C., DING, Z., TAN, Q., QI, H. HE, Y. (2014). Preparation of Nano α-Alumina Powder and Wear Resistance of Nanoparticles Reinforced Composite Coating. In: *Powder Technology*. Vol. 257, p. 83–87. ISSN: 0032-5910.

53. GLORIAS-GARCIA, F., ARRIAGA-MERCED, J.M., ROA-MORALES, G., VARELA-GUERRERO, V., BARRERA-DÍAZ, C.E., BILYEU, B. (2014). Fast Reduction of Cr(VI) from Aqueous Solutions Using Alumina. In: *Journal of Industrial and Engineering Chemistry*. Vol. 20, no. 4, p. 2477–2483. ISSN: 1226-086X.

54. CHIBUZO, A.J. (2013). *Energy-Efficient Low-Temperature Drying Using Adsorbents: a Process Systems Engineering Approach*. PhD Thesis. Wageningen University, the Netherlands.

55. SIVASANKAR, V., RAMACHANDRAMOORTHY, T. (2011). Water Softening Behaviour of Sand Materials – Mimicking Natural Zeolites in Some Locations of Rameswaram Island, India. In: *Chemical Engineering Journal*. Vol. 171, no. 1, p. 24–32. ISSN: 1385-8947.

56. BURRIESCI, N., VALENTE, S., ZIPELLI, C., BART, J.C.J. (1984). Studies on Zeolites in Agriculture. Effect on Crop Growth of Prunus Persica and Vifis Vinifera. In: *Zeolites*. Vol. 4, no. 4, p. 373–376.

57. VISA, M. (2016). Synthesis and Characterization of New Zeolite Materials Obtained from Fly Ash for Heavy Metals Removal in Advanced Wastewater Treatment. In: *Powder Technology*. Vol. 294, p. 338–347. ISSN: 0032-5910.

58. OZEN, S., GONCUOGLU, M.C., LIGUORI, B., DE GENNARO, B., CAPPELLETTI, P., GATTA, G.D., IUCOLANO, F., COLELLA, C. (2016). A Comprehensive Evaluation of Sedimentary Zeolites From Turkey as Pozzolanic Addition of Cement- and Lime-Based Binders. In: *Construction and Building Materials*. Vol. 105, p. 46–61. ISSN: 0950-0618.

59. KUZNIARSKA-BIERNACKA, I., FONSECA, A.M., NEVES, I.C. (2013). Manganese Complexes with Triazenido Ligands Encapsulated in NaY Zeolite as Heterogeneous Catalysts. In: *Inorganica Chimica Acta*. Vol. 394, p. 591–597. ISSN: 0020-1693.

60. SAMARGHANDI, M.R., AL-MUSAWI, T.J., MOHSENI-BANDPI, A., ZARRABI, M. (2015). Adsorption of Cephalexin from Aqueous Solution Using Natural Zeolite and Zeolite Coated with Manganese Oxide Nanoparticles. In: *Journal of Molecular Liquids*.. Vol. 211, p. 431–441. ISSN: 0167-7322.

61. SAYILGAN, S.C., MOBEDI, M. ULKU, S. (2016). Effect of Regeneration Temperature on Adsorption Equilibria and Mass Diffusivity of Zeolite 13x-Water Pair. In: *Microporous and Mesoporous Materials*. Vol. 224, p. 9–16. ISSN: 1387-1811.

62. BENTAHAR, Y., HUREL, C., DRAOUI, K., KHAIROUN, S., MARMIER, N. (2016). Adsorptive Properties of Moroccan Clays for the Removal of Arsenic(V) from Aqueous Solution. In: *Applied Clay Science*. Vol. 119, p. 385–392. ISSN: 0169-1317.

63. PADILLA-ORTEGA, E., LEYVA-RAMOS, R., FLORES-CANO, J.V. (2013). Binary Adsorption of Heavy Metals from Aqueous Solution onto Natural Clays. In: *Chemical Engineering Journal*. Vol. 225, p. 536–546. ISSN: 1385-8947.

64. REN, X., ZHANG, Z., LUO, H., HU, B., DANG, Z., YANG, C., LI, L. (2014). Adsorption of Arsenic on Modified Montmorillonite. In: *Applied Clay Science*.. Vol. 97–98, p. 17–23. ISSN: 0169-1317.

65. MANEERUNG, T., LIEW, J., DAI, Y., KAWI, S., CHONG, C., WANG, C.H. (2016). Activated Carbon Derived from Carbon Residue from Biomass Gasification and Its Application for Dye Adsorption: Kinetics, Isotherms and Thermodynamic Studies. In: *Bioresource Technology*. Vol. 200, p. 350–359. ISSN: 0960-8524.

66. SAYGILI, H., GUZEL, F. (2016). High Surface Area Mesoporous Activated Carbon from Tomato Processing Solid Waste by Zinc Chloride Activation: Process Optimization, Characterization and Dyes Adsorption. In: *Journal of Cleaner Production.*. Vol. 113, p. 995–1004. ISSN: 0959-6526.

67. IMAMOGLU, M., TEKIR, O. (2008). Removal of Copper (II) and Lead (II) Ions from Aqueous Solutions by Adsorption on Activated Carbon From a New Precursor Hazelnut Husks. In: *Desalination*.. Vol. 228, no. 1–3, p. 108–113. ISSN: 0011-9164.

68. BALTAKYS, K., SIAUČIŪNAS, R. (2010). Influence of Gypsum Additive on the Gyrolite Formation Process. In: *Cement and Concrete Research*. Vol. 40, no. 3, p. 376–383. ISSN: 0008-8846.

69. BANKAUSKAITĖ, A., BALTAKYS, K. (2009). The Sorption of Copper Ions by Gyrolite in Alkaline Solution. In: *Materials Science-Poland*. Vol. 27, no. 3, p. 899–908. ISSN: 2083-134X.

70. SIAUČIŪNAS, R., JANICKIS, V., PALUBINSKAITĖ, D., IVANAUSKAS, R. (2004). The Sorption Properties of Tobermorite Modified with Na^{+} and Al^{3+} Ions. In: *Ceramics-Silikáty*. Vol. 48, no. 2, p. 76–82. ISSN: 1804-5847.

71. KASPERAVIČIŪTĖ, V., BALTAKYS, K., SIAUČIŪNAS, R. (2008). The Sorption Properties of Gyrolite for Copper Ions. In: *Ceramics-Silikáty*. Vol. 52, no. 2, p. 95–101. ISSN: 1804-5847.

72. SIAUCIUNAS, R., IVANAUSKAS, R. (2002). Elimination of Heavy Metals from Water by Modified Tobermorite. In: *Environmental Research, Engineering and Management*. Vol. 3, no. 3, p. 61–66. ISSN: 1392-1649.

73. RICHARDSON, I.G. (2008). The Calcium Silicate Hydrates. In: *Cement and Concrete Research*. Vol. 38, no. 2, p. 137–158. ISSN: 0008-8846.

74. BALANDIS, A., JASIUKEVIČIUS, V., MARTYNAITIS, M., STRAZDAS, K. (1995). *The Fundamentals of Silicate Technology*. Vilnius, Lithuania: The Institute of Scientific and Encyclopaedic Press.

75. TAYLOR H.F.W. (1997). *Cement Chemistry*. San Diego: Academic Press.

76. BALTAKYS, K., PRICHOCKIENĖ, E. (2010). Influence of CaO Reactivity on the Formation of Low-Base Calcium Silicate Hydrates. In: *Materials Science-Poland*. Vol. 28, no. 1, p. 295–304. ISSN: 2083-134X.

77. BALTAKYS, K., SIAUČIŪNAS, R. (2007). Formation of Gyrolite in the CaO – Quartz – NaO – H_2O System. In: *Materials Science-Poland*. Vol. 25, no. 4, p. 4–10. ISSN: 2083-134X.

78. MOSTAFA, N.Y., GARIB, R.A., HEIBA, Z.K., ABD-ELKADER, O.H., AL-MAJTHOUB, M.M. (2015). Synthesis of Pure Zeolite P2 from Calcium Silicate Hydrate; Tobermorite. In: *Oriental Journal of Chemistry*. Vol. 32, no. 2, p. 1051–1056.

79. THURN, F., BURMESTER, K., POCHERT, J., WOLFF, S. (1975). *Rubber Compositions Containing Silica and an Organosilane*. Patent US3873489 A, 1975.

80. GUAN, W., ZHAO, X. (2016). Fluoride Recovery Using Porous Calcium Silicate Hydrates via Spontaneous Ca^{2+} and OH^- Release. In: *Separation and Purification Technology*. Vol. 165, p. 71–77. ISSN: 1383-5866.

81. WALTER, P.G. (1978). *High Density Asbestos-Free Tobermorite Thermal Insulation Containing Wollastonite*. High United States Patent 4,128,434, December 5, 1978.

82. OKANO, K., UEMOTO, M., KAGAMI, J., MIURA, K., AKETO, T., TODA, M., HONDA, K., OHTAKE, H. (2013). Novel Technique for Phosphorus Recovery from Aqueous Solutions Using Amorphous Calcium Silicate Hydrates (A-CSHs). In: *Water research*. Vol. 47, no. 7, p. 2251–2259. ISSN: 0043-1354.

83. EL-KORASHY, S.A. (2002). Synthetic Crystalline Calcium Silicate Hydrate (1): Cation Exchange and Caesium Selectivity. In: *Chemical Monthly*. Vol. 133, p. 333–343. ISSN: 1434-4475.

84. KOSSIK, J. (2004). Plasmid DNA Purification Possibilities Using the Disposable Rotary Drum Filter. In: *BioProcess International*, 2004, p. 72–73.

85. WILLIAMS, P.T. (2013). Universities of Leeds , Sheffield and York Pyrolysis of Waste Tyres: A Review. In: *Waste Management*. Vol. 33, p. 137–144. ISSN: 0956-053X.

86. WINTERS, M.A., RICHTER, J.D., SAGAR, S.L., LEE, A.L., LANDER, R.J. (2003). Plasmid DNA Purification by Selective Calcium Silicate Adsorption of Closely Related Impurities. In: *Biotechnology Progress*. Vol. 19, no. 2, p. 440–447.

87. YANAGISAWA, K., FENG, Q., YAMASAKI, N. (1997). Hydrothermal Synthesis of Xonotlite Whiskers by Ion Diffusion. In: *Journal of Materials Science Letters*. Vol. 16, no. 11, p. 889–891. ISSN: 1573-4811.

88. MERLINO, S; BONACCORSI, E; ARMBRUSTER, T. (2001). The Real Structure of Tobermorite 11 Angstrom: Normal and Anomalous Forms, OD Character and Polytypic Modifications. In: *European Journal of Mineralogy*. Vol. 13, no. 3, p. 577–590. ISSN 0935-1221.

89. MAESHIMA, T., NOMA, H., SAKIYAMA, M., MITSUDA, T. (2003). Natural 1.1 and 1.4 nm Tobermorites from Fuka, Okayama, Japan: Chemical Analysis, Cell Dimensions, 29Si NMR and Thermal Behavior. In: *Cement and Concrete Research*. Vol. 33, no. 10, p. 1515–1523. ISSN: 0008-8846.

90. MOON, J., YOON, S., MONTEIRO, P.J.M. (2015). Mechanical Properties of Jennite: A Theoretical and Experimental Study. In: *Cement and Concrete Research*. Vol. 71, p. 106–114. ISSN: 0008-8846.

91. BONACCORSI, E., MERLINO, S., KAMPF, A.R. (2005). The Crystal Structure of Tobermorite 14 Å (Plombierite), a C-S-H phase. In: *Journal of American Ceramic Society*. 2005. Vol. 88. no. 3, p. 505–512. ISSN: 1551-2916.

92. BONACCORSI, E., MERLINO, S., TAYLOR, H. (2004). The Crystal Structure of Jennite, $Ca_9Si_6O_{18}(OH)_6 \cdot 8H_2O$. In: *Cement and Concrete Research*. Vol. 34, p. 1481–1488. ISSN: 0008-8846.

93. YU, P., KIRKPATRICK, R. (1999). Thermal Dehydration of Tobermorite and Jennite. In: *Concrete Science and Engineering*. Vol. 1, no. 3, p. 185–191. ISSN: 1295-2826.

94. SIAUČIŪNAS, R., BALTAKYS, K. (2004). Formation of gyrolite during Hydrothermal Synthesis in the Mixtures of CaO and Amorphous SiO_2 or Quartz. In: *Cement and Concrete Research*. Vol. 34, no. 11, p. 2029–2036. ISSN: 0008-8846.

95. GARBEV, K., BLACK, L., BEUCHLE, G., STEMMERMANN, P. (2002). Inorganic Polymers in Cement Based Materials. In: *Wasser- und Geotechnologie*. Vol. 1, no. 2, p. 19–30.

96. PALOU, M., ŽIVICA, M., IFKA, T., BOHAČ, M., ZMRZLY, M. (2014). Effect of Hydrothermal Curing on Early Hydration of G-oil Well Cement. In: *Journal of Thermal Analysis and Calorimetry*. Vol. 116, p. 597–603. ISSN: 1588-2926.

97. ISHIDA, H., YAMAZAKI, S., SASAKI, K., OKADA, Y. MITSUDA, T. (1993). α-Dicalcium Silicate Hydrate – Preparation, Decomposed Phase, And Its Hydration. In: *Journal Of The American Ceramic Society*. Vol. 76, p. 1707. ISSN: 1551-2916.

98. GARBEV, K., GASHAROVA, B., BEUCHLE, G., KREISZ, S. STEMMERMANN, P. (2008). First Observation of α-$Ca_2[SiO_3(OH)](OH)$-$Ca_6[Si_2O_7][SiO_4](OH)_2$ Phase Transformation upon Thermal Treatment in Air. In: *Journal Of The American Ceramic Society*. Vol. 91, p. 263. ISSN: 1551-2916.

99. BALTAKYS, K., DAMBRAUSKAS, T., SIAUČIŪNAS, R., EISINAS, A. (2014). Formation of α-C_2S Hydrate in the Mixtures with CaO/SiO_2 = 1.75 by Hydrothermal Treatment at 200 °C. In: *Romanian Journal of Materials*. Vol. 44, no. 1, p. 109–115. ISSN: 2457-502X.

100. BALTAKYS, K., SIAUČIŪNAS, R. (2007). The Influence of Stirring and γ -Al_2O_3 or Na_2O Additives on the Gyrolite Formation in the CaO – Quartz – H_2O System. In: *Materials Science-Poland*. Vol. 51, no. 2, p. 106–111. ISSN: 2083-134X.

101. RÓŻYCKA, A., KOTWICA, L., MAŁOLEPSZY, J. (2014). Synthesis of Single Phase Gyrolite in the CaO-Quartz-Na_2O-H_2O System. In: *Materials Letters*. Vol. 120, p. 166–169. ISSN: 0167-577X.

102. *THE MINERAL GYROLITE*. Available from: http://www.galleries.com/Gyrolite

103. MACKAY, A.L., TAYLOR, H.F.W. (1953). Gyrolite. In: *Mineralogical Magazine*, 1953, 30, 80.

104. KALOUSEK, G.L., NELSON, E.B. (1978). Hydrothermal Reactions of Dicalcium Silicate and Silica. In: *Cement and Concrete Research*. Vol. 8, no. 3, p. 283–289. ISSN:

0008-88461978.

105. STEVULA, L., PETROVIC, J. (1983). Formation of an Intermediate C-S-H Phase during the Hydrothermal Synthesis of Gyrolite. In: *Journal of Cement and Concrete Research*. Vol. 13, p. 684. ISSN: 0008-8846.

106. SHAW S., HENDERSON C.M.B., CLARK S.M. (2002). In-Situ Synchrotron Study of the Kinetics, Thermodynamics, and Reaction Mechanism of the Hydrothermal Crystallization of Gyrolite $Ca_{16}Si_{24}O_{60}(OH)_8 \cdot 14H_2O$. In: *American Mineralogist*. Vol. 87, p. 533.

107. JAUBERTHIE, R., TEMIMI, M., LAQUERBE, M. (1996). Hydrothermal Transformation of Tobermorite Gel to 10 Å Tobermorite. In: *Cement and Concrete Research*. Vol. 26, no. 9, p. 1335–1339. ISSN: 0008-8846.

108. CHALMERS, R.A., FARMER, V.C., HARKER, R.I., TAYLOR, H.F.W. (1964). Reyerite. In: *Mineralogical Magazine*. Vol. 33, no. 1, p. 821–840. ISSN 0026-461X.

109. ABO-EL-ENEIN, S.A., KISHAR, E.A., MOSTAFA, N.Y. (2009). FTIR Study and Cation Exchange Capacity of Fe^{3+}- and Mg^{2+}-Substituted Calcium Silicate Hydrates. In: *Journal of Alloys and Compounds*. April 2009. Vol. 473, no. 1–2, p. 538–542. ISSN: 0925-8388.

110. KIKUMA, J., TSUNASHIMA, M., ISHIKAWA, T., MATSUNO, S., OGAWA, A., MATSUI, K., SATO, M. (2011). In Situ Time-Resolved X-Ray Diffraction of Tobermorite Synthesis Process under Hydrothermal Condition. In: *IOP Conference Series: Materials Science and Engineering*. Vol. 18, no. 2, p. 60–66. ISSN: 1097-0002.

111. *TOBERMORITE*. Available from: http://rruff.info/Tobermorite

112. COLEMAN, N.J. (2005). Synthesis, Structure and Ion Exchange Properties of 11Å Tobermorites from Newsprint Recycling Residue. In: *Materials Research Bulletin*. Vol. 40, no. 11, p. 2000–2013. ISSN: 0025-5408.

113. COLEMAN, N.J., BRASSINGTON, D.S. (2003). Synthesis of Al-Substituted 11 Å Tobermorite from Newsprint Recycling Residue: a Feasibility Study. In: *Materials Research Bulletin*. Vol. 38, no. 3, p. 485–497. ISSN: 0025-5408.

114. YOUSSEF, H., IBRAHIM, D., KOMARNENI, S., MACKENZIE, K.J.D. (2010). Synthesis of 11Å Al-Substituted Tobermorite from Trachyte Rock by Hydrothermal Treatment. In: *Ceramics International*. Vol. 36, no. 1, p. 203–209. ISSN: 0272-8842.

115. KOMARNENI, S., ROY, D.M. (1983). Tobermorites: a New Family of Cation Exchangers. In: *Nature*. Vol. 221, no. 12, p. 647–648. ISSN 0028-0836.

116. ABH, N.J.B.M., BERNSTEIN, S., FEHR, K.T., HOCHLEITNER, R. (2009). Crystal Chemistry of Xonotlite $Ca_6Si_6O_{17}(OH)_2$. Part I : Determination of Polytypes Using X-Ray. In: *Powder Diffraction* (XRPD). Vol. 186, no. August, p. 70176.

117. *XONOTLITE*. Available from: http://www.dakotamatrix.com/mineralpedia/8626/xonotlite

118. LIU, F., ZENG, L.K., CAO, J.X., ZHU, B., YUAN, A. (2010). Hydrothermal Synthesis of Xonotlite Fibers and Investigation on Their Thermal Property. In: *Advanced Materials Research*. Vol. 105–106, no. 1, p. 841–843. ISSN: 1435-1889.

119. CAO, J., LIU, F., LIN, Q., ZHANG, Y. (2008). Hydrothermal Synthesis of Xonotlite from Carbide Slag. In: *Progress in Natural Science*. Vol. 18, no. 9, p. 1147–1153. ISSN: 1002-0071.

120. LI, X., CHANG, J. (2006). A Novel Hydrothermal Route to the Synthesis of Xonotlite Nano-Fibers and Investigation on Their Bioactivity. In: *Journal of Materials Science*.

Vol. 41, p. 4944–4947. ISSN: 1573-4803.

121. KYRITSIS, K., HALL, C., BENTZ, D.P., MELLER, N., WILSON, M.A. (2009). Relationship between Engineering Properties, Mineralogy, And Microstructure in Cement-Based Hydroceramic Materials Cured at 200 °C–350 °C. In: *Journal of the American Ceramic Society*. Vol. 92, no. 3, p. 694–701. ISSN: 1551-2916.

122. BASPINAR, M.S., DEMIR, I., KAHRAMAN, E., GORHAN, G. (2014). Utilization Potential of Fly Ash together with Silica Fume in Autoclaved Aerated Concrete Production. In: *Environmental Engineering*. Vol. 18, p. 47–52.

123. LIU, F., WANG, X.D., Cao, J.X. (2013). Effect of Na^+ on Xonotlite Crystals in Hydrothermal Synthesis. In: *International Journal of Minerals, Metallurgy, and Materials*. Vol. 20, no. 1, p. 88–93. ISSN: 1869-103X.

124. BALTAKYS, K., JAUBERTHIE, R., KASPERAVIČIŪTĖ, V. (2009). Formation and Stability of C-S-H(I) in $Ca(OH)_2$/CaO–Thermal Silica Densified–H_2O System. In: *Ceramics Silicáty*. Vol. 53, no. I, p. 81–87. ISSN: 1804-5847.

125. ARABI, N., JAUBERTHIE, R., MOLEZ, L. (2015). Formation of C-S-H in Calcium Hydroxide – Blast Furnace Slag – Quartz – Water System in Autoclaving Conditions. Vol. 27, no. 3, p. 153–162. ISSN: 0951-7197.

126. EL-KORASHY, S.A., AL-WAKEEL, E.I., Kishar, E.A. (1998). Hydrothermal Synthesis of Calcium Silicate Hydrates in The Presence Of 3D-Ferromagnetic Cations. In: *Indian Journal of Chemistry*. Vol. 37, no. 12, p. 1098–1101. ISSN: 0975-0983.

127. KOIZUMI, K., TSUYUKI, N. (2004). Effect of Silicate Anion Structure on Fixation of Chloride Ions by Calcium Silicate Hydrates. In: J*ournal of the American Ceramic Society*. Vol. 87, p. 412–416. ISSN: 1551-2916.

128. MELLER, N., HALL, C., PHIPPS, J.S. (2005). A New Phase Diagram for the CaO-Al_2O_3-SiO_2-H_2O Hydroceramic System at 200 Degrees. In: *Materials Research Bulletin*. Vol. 40, no. 5, p. 715–723. ISSN: 0025-5408.

129. NOCUÒ-WCZELIK, W. (1999). Effect of Na and Al on the Phase Composition and Morphology of Autoclaved Calcium Silicate Hydrates. In: *Cement and Concrete Research*. Vol. 29, no. 11, p. 1759–1767. ISSN: 0008-8846.

130. BALTAKYS, K. and SIAUČIŪNAS, R. (2006). The Influence of γ-Al_2O_3 and Na_2O on the Formation of Gyrolite in the Stirring Suspension. In: *Journal of Materials Science*. Vol. 41, no. 15, p. 4799–4805. ISSN: 0022-2461.

131. BLAKEMAN, E.A., GARD, J.A., RAMSAY, C.G., TAYLOR, H.F.W. (1974). Studies on the System Sodium Oxide-Calcium Oxide-Silica-Water. In: *Journal of Applied Chemistry and Biotechnology*. 24 (1974), p. 239. ISSN: 1097-4660.

132. BALTAKYS, K., EISINAS, A., DIZHBITE, T., JASINA, L., SIAUČIŪNAS, R., KITRYS, S. (2011). The Influence of Hydrothermal Synthesis Conditions on Gyrolite Texture and Specific Surface Area. In: *Materials and Structures*. 25 March 2011. Vol. 44, no. 9, p. 1687–1701. ISSN: 1871-6873.

133. EISINAS, A., BALTAKYS, K., SIAUČIŪNAS, R. (2012). The Effect of Gyrolite Additive on the Hydration Properties of Portland Cement. In: *Cement and Concrete Research*. Vol. 42, no. 1, p. 27–38.ISSN: 0008-8846.

134. BALTAKYS, K., SIAUČIŪNAS, R. (2010). Influence of Gypsum Additive on the Gyrolite Formation Process. In: *Cement and Concrete Research*. Vol. 40, no. 3, p. 376–383. ISSN: 0008-8846.

135. BALTAKYS, K., SIAUČIŪNAS, R. (2007). Formation of Gyrolite in the CaO – Quartz – Na_2O – H_2O System. In: *Materials Science-Poland.* 2007. Vol. 25, no. 4, p. 1089 – 1100. ISSN: 2083-1331.

136. COLEMAN, N.J. (2005). Synthesis, Structure and Ion Exchange Properties of 11 Å Tobermorites from Newsprint Recycling Residue. In: *Materials Research Bulletin*. Vol. 40, no. 11, p. 2000–2013. ISSN: 0025-5408.

137. SHRIVASTAVA, O.P., SHRIVASTAVA, R. (2001). Study on Selective Sorption of Cs-137 on Al-Substituted Calcium Silicate Hydroxy Hydrate. In: *Journal of the Indian Chemical Society*. Vol. 78, p. 392–394. ISSN: 00194522.

138. EL-KORASHY, S.A., AL-WAKEEL, E.I., EL-HEMALY, S.A., RIZK, M.A. (2001). Divalent Ion Uptake of Heavy Metal Cations by (Aluminum + Alkali Metals) – Substituted Synthetic 1.1 nm-Tobermorites. In: *Journal of Materials Science*. Vol. 36, p. 2405–2415. ISSN: 0022-2461.

139. ILJINA, A., BALTAKYS, K., EISINAS, A. (2016). The Effect of Gyrolite Structure Properties on Zn^{2+} Ion Adsorption. In: *Desalination and Water Treatment*. Vol. 57, no. 4, p. 1756–1765. ISSN: 1944-3994.

140. ILJINA, A., BALTAKYS, K., EISINAS, A. (2015). Gyrolite Adsorption of Zn^{2+} Ions in Acidic and Alkaline Solutions. In: *Materials Science (Medžiagotyra).* Vol. 21, no. 1. ISSN: 1392-1320.

141. BANKAUSKAITĖ, A., EISINAS, A., BALTAKYS, K., ZADAVIČIŪTĖ, S. (2014). A Study on the Intercalation of Heavy Metal Ions in a Wastewater by Synthetic Layered Inorganic Adsorbents. In: *Desalination and Water Treatment*. Vol. 3994. p. 1–11. ISSN: 1944-3994.

142. ZADAVIČIŪTĖ, S., BALTAKYS, K., EISINAS, A. (2015). Adsorption Kinetic Parameters of Fe^{3+} and Ni^{2+} Ions by Gyrolite. In: *Materials Science (Medžiagotyra).* Vol. 21, no. 1, p. 117–122. ISSN: 1392-1320.

143. HUNCE, S.Y., AKGUL, D., DEMIR, G., MERTOGLU, B. (2012). Solidification/Stabilization of Landfill Leachate Concentrate Using Different Aggregate Materials. In: *Waste Management*. Vol. 32, no. 7, p. 1394–1400. ISSN: 0956-053X.

144. ERDEM, M., ZVERDI, A. (2011). Environmental Risk Assessment and Stabilization/Solidification of Zinc Extraction Residue: II. Stabilization/Solidification. In: *Hydrometallurgy*. 2011. Vol. 105, no. 3–4, p. 270–276. ISSN: 0304-386X.

145. AKHTER, H., CARTLEDGE, F.K., ROY, A., TITTLEBAUM, M.E. (1997). Solidification/Stabilization of Arsenic Salts: Effects of Long Cure Times. In: *Journal of Hazardous Materials*. Vol. 52, no. 2–3, p. 247–264. ISSN: 0304-3894.

146. COLORADO, H.A., GARCIA, E., BUCHELY, M.F. (2016). White Ordinary Portland Cement Blended with Superfine Steel Dust with High Zinc Oxide Contents. In: *Construction and Building Materials*. June 2016. Vol. 112, p. 816–824. ISSN: 0950-0618.

147. LI, Y., LIU, Y., GONG, X., NIE, Z., CUI, S., WANG, Z., CHEN, W. (2015). Environmental Impact Analysis of Blast Furnace Slag Applied to Ordinary Portland Cement Production. In: *Journal of Cleaner Production.* Vol. 120, p. 221–230. ISSN: 0959-6526.

148. PARIS, J.M., ROESSLER, J.G., FERRARO, C.C., DEFORD, H.D., TOWNSEND, T.G. (2016). A Review of Waste Products Utilized as Supplements to Portland Cement in Concrete. In: *Journal of Cleaner Production*. February 2016. Vol. 121, p. 1–18. ISSN: 0959-6526.

149. PARIA, S., YUET, P.K. (2006). Solidification–Stabilization of Organic and Inorganic

Contaminants Using Portland Cement: a Literature Review. In: *Environmental Reviews*. Vol. 14, no. 4, p. 217–255.

150. ACHTERNBOSCH, M., BRÄUTIGAM, Kr., GLEIS, M.N. (2003). Heavy Metals in Cement and Concrete Resulting from the Co-Incineration of Wastes in Cement Kilns with Regard to the Legitimacy of Waste Utilisation. In: *Investigación de Karlsruhe, en la Asociación Helmholtz*. Vol. 6923, p. 1–200.

151. EISINAS, A. BALTAKYS, K., SIAUČIŪNAS, R. (2013). Utilisation of Gyrolite with Impure Cd^{2+} Ions in Cement Stone. In: *Advances in Cement Research*. Vol. 25, no. 2, p. 69–79. ISSN: 1751-7605.

152. EUROPEAN COMMITTEE FOR STANDARDIZATION. *European Standard. Building Lime - Part 2: Test Methods.* LSTEN 459-2:2010. 2010.

153. АЛЕКИН О.А. *Химический анализ вод суши (при стационарном их изучении).* Гидрометеорологическое изд-во. 1954.

154. HAMEED, B.H., MAHMOUD, D.K., AHMAD, A.L. (2008). Equilibrium Modeling and Kinetic Studies on the Adsorption of Basic Dye by a Low-Cost Adsorbent: Coconut (Cocos Nucifera) Bunch Waste. In: *Journal of Hazardous Materials*. Vol. 158, no. 1, p. 65–72.ISSN: 0304-3894.

155. QIU, H.,PAN, B., ZHANG, Q.Q., ZHANG, W., ZHANG, Q.Q. (2009). Critical Review in Adsorption Kinetic Models. In: *Journal of Zhejiang University SCIENCE A*. Vol. 10, no. 5, p. 716–724. doi: 10.1631/jzus.A0820524.

156. CHEARY R.W., COELHO, A.A. (1996). *Programs XFIT and FOURYA, Deposited in CCP14 Powder Diffraction Library, Engineering and Physical Sciences Research Council, Daresbury Laboratory*, Warrington, England.

157. LOWELL, S., SHIELDS, J.E., THOMAS, M.A. (2004). *Characterization of Porous Solids and Powders: Surface Area, Pore Size and Density*. New York: Kluwer Academic Publisher.

158. BAOUIA, K., MESSAITFA, A. (2015). Distribution and Removal of Fluoride Ions in the Drinking Waters in the Algerian South (Ouargla as a Showcase). In: *Energy Procedia*. Vol. 74, p. 294–300. ISSN: 1876-6102.

159. DEHGHANI, M.H., HAGHIGHAT, G.A., YETILMEZSOY, K., MCKAY, G., HEIBATI, B., TYAGI, I., AGARWAL, S., GUPTA, V.K. (2016). Adsorptive Removal Of Fluoride from Aqueous Solution Using Single- and Multi-Walled Carbon Nanotubes. In: *Journal of Molecular Liquids*. Vol. 216, p. 401–410. ISSN: 0167-7322.

160. GOGOI, S., DUTTA, R.K. (2016). Fluoride Removal By Hydrothermally Modified Limestone Powder Using Phosphoric Acid. In: *Journal of Environmental Chemical Engineering*. Vol. 4, no. 1, p. 1040–1049. ISSN: 2213-3437.

161. GUZMÁN, A., NAVA, J.L., COREÑO, O., RODRÍGUEZ, I., GUTIÉRREZ, S. (2016). Arsenic and Fluoride Removal from Groundwater by Electrocoagulation Using a Continuous Filter-Press Reactor. In: *Chemosphere*. Vol. 144, p. 2113–2120. ISSN: 0045-6535.

162. TANG, D., ZHANG, G. (2016). Efficient Removal of Fluoride by Hierarchical Ce–Fe Bimetal Oxides Adsorbent: Thermodynamics, Kinetics and Mechanism. In: *Chemical Engineering Journal*. Vol. 283, p. 721–729. ISSN: 1385-8947.

163. ZHU, R., ZHAO, W., ZHAI, M., WEI, F., CAI, Z., SHENG, N., HU, Q. (2010). Molecularly Imprinted Layer-Coated Silica Nanoparticles for Selective Solid-Phase Extraction of Bisphenol A From Chemical Cleansing and Cosmetics Samples. In: *Analytica Chimica Acta*. Vol. 658, p. 209. ISSN: 0003-2670.

164. ŽVIRONAITĖ, J., GAIDUČIS, S., KAMINSKAS, A., MAČIULAITIS, R. (2008). Hydration and Hardening of Composite Binder Containing Mechanically Activated Hemihydrate Phosphogypsum. In: *Materials Science* (*Medžiagotyra)*. Vol. 14, no. 4, p. 356–360. ISSN: 1392-1320.

165. GAIDUČIS, S., ŽVIRONAITĖ, J., MAČIULAITIS, R., JAKOVLEV, G. (2011). Resistance of Phosphogypsum Cement Pozzolanic Compositions against the Influence of Water. In: *Materials Science (Medžiagotyra)*. Vol. 17, no. 3, p. 308–313. ISSN: 1392-1320.

166. PALUBINSKAITĖ, D., KANTAUTAS, A. (2005). Ceolitų sintezė naudojant technogeninį silikagelį. In: *Materials Science (Medžiagotyra)*. Vol. 4, no. 4, p. 35–40. ISSN: 1392-1320.

167. EISINAS A. (2013). *Girolito sandaros ypatybės ir panaudojimas*. PhD Thesis. Kaunas: Kaunas University of Technology.

168. GARBEV, K. (2004). *Ph.D. Thesis*. Sofia: Faculty of Geology and Geography, St. Kliment Ohridski University.

169. GARD, J.A., MITSUDA, T., TAYLOR, H.F.W. (1975). Some Observations on Assarsson's Z-Phase and Its Structural Relations to Gyrolite, Truscottite, and Reyerite. In: *Mineralogical Magazine*. Vol. 40, p. 325. ISSN: 1471-8022.

170. LACHOWSKI, E.E., MURRAY, L.W., TAYLOR, H.F.W. (1979). Truscottite Composition and Ionic Substitutions. In: *Mineralogical Magazine*. Vol. 43, p. 333. ISSN: 1471-8022.

171. GARBEV, K., GASHAROVA, B., STUMM, A., BLACK, L., MATHIS, Y.L., STEMMERMANN, P. (2004). Phase Transition of Gyrolite into Truscottite upon Thermal Treatment as Studied at the ANKA Infrared and XRD Beamlines. In: *Mineralogische und Technische Kristallographie*. Vol. 21, p. 118.

172. BALTAKYS, K. (2009). Influence of Gypsum Additive on the Formation of Calcium Silicate Hydrates in Mixtures with C/S = 0.83 or 1.0. In: *Materials Science-Poland*. Vol. 27, no. 4, p. 1091–1101. ISSN: 2083-134X.

173. WORLD HEALTH ORGANIZATION (WHO). (2008). *Guideline for Drinking Water Quality*. Third edition. Geneva. Vol. 1, p. 375–377. ISBN 92-4-154638-7.

174. VÁZQUEZ-GUERRERO, A., ALFARO-CUEVAS-VILLANUEVA, R., RUTIAGA-QUIÑONES, J.G., CORTÉS-MARTÍNEZ, R. (2016). Fluoride Removal by Aluminum-Modified Pine Sawdust: Effect of Competitive Ions. In: *Ecological Engineering*. Vol. 94, p. 365–379. ISSN: 0925-8574.

175. PARASHAR, K., BALLAV, N., DEBNATH, S., PILLAY, K., MAITY, A. (2016). Rapid and Efficient Removal of Fluoride Ions from Aqueous Solution Using a Polypyrrole Coated Hydrous Tin Oxide Nanocomposite. In: *Journal of Colloid and Interface Science*. Vol. 476, p. 103–118. ISSN: 2215-0382.

176. KATSOU, E., MALAMIS, S., TZANOUDAKI, M., HARALAMBOUS, K.J., LOIZIDOU, M. (2011). Regeneration of Natural Zeolite Polluted by Lead and Zinc in Wastewater Treatment Systems. In: *Journal of Hazardous Materials*. Vol. 189, p. 773–786. ISSN: 0304-3894.

177. VAN DEN BERGE, J., NAUDTS, K., JANSSENS, I.A., CEULEMANS, R., NIJS, I. (2011). Does the Stress Tolerance of Mixed Grassland Communities Change in a Future Climate? A Test with Heavy Metal Stress (Zinc Pollution). In: *Environmental Pollution*.. Vol. 159, p. 329–331. ISSN: 0269-7491.

178. CESUR, H., BALKAYA, N. (2007). Zinc Removal from Aqueous Solution Using an

Industrial By-Product Phosphogypsum. In: *Chemical Engineering Journal*. Vol. 131, p. 203–208. ISSN: 1385-8947.

179. PENG, L., SUN, D., SU, M., HAN, J., DONG, C. (2012). Rapid Analysis on the Heavy Metal Content of Spent Zinc–Manganese Batteries by Laser-Induced Breakdown Spectroscopy. In: *Optics & Laser Technology*. Vol. 44, p. 2469–2475. ISSN: 0030-3992.

180. STUMM, A., GARBEV, K., BEUCHLE, G., BLACK, L., STEMMERMANN, P., NÜESCH, R. (2005). Incorporation of Zinc into Calcium Silicate Hydrates, Part I: Formation of C-S-H(I) with C/S=2/3 and Its Isochemical Counterpart Gyrolite. *Cement and Concrete Research*. Vol. 35, no. 9, p. 1665–1675. ISSN: 0008-8846.

List of Scientific Publications

List of Scientific Publications on the Theme of the Dissertation

Publications in Journals Included into the Institute for Scientific Information (ISI) Database

1. Iljina, Aliona; Baltakys, Kęstutis; Eisinas, Anatolijus. (2015). Gyrolite Adsorption of Zn^{2+} Ions in Acidic and Alkaline Solutions // In: *Materials science = Medžiagotyra* / Kaunas University of Technology, Academy of Sciences of Lithuania. Kaunas: KTU. ISSN 1392-1320. Vol. 21, no. 1, p. 123–128.
2. Baltakys, Kęstutis; Iljina, Aliona; Bankauskaitė, Agnė. (2015). Thermal Properties and Application of Silica Gel Waste Contaminated with F^- Ions for C-S-H Synthesis / Kestutis Baltakys, Aliona Iljina, Agne Bankauskaite // In: *Journal of Thermal Analysis and Calorimetry*. Dordrecht: Springer. ISSN 1388-6150. Vol. 121, issue 1, p. 145–154.
3. Iljina, Aliona; Baltakys, Kęstutis; Baltakys, Marius; Šiaučiūnas, Raimundas. (2014). Neutralization and Removal of Compounds Containing Fluoride Ions from Waste Silica Gel // In: *Revista Romana de materiale = Romanian Journal of Materials*. Bucharest: Serban Solacolu Foundation. ISSN 1583-3186. Vol. 44, issue 3, p. 265–271.
4. Iljina, Aliona; Baltakys, Kęstutis; Eisinas, Anatolijus. (2016). The Effect of Gyrolite Structure Properties on Zn^{2+} Ion Adsorption // Desalination and Water Treatment. Philadelphia, PA: Taylor & Francis. ISSN 1944-3994. Vol. 57, issue 4, p. 1756–1765.
5. Iljina, Aliona; Baltakys, Kęstutis; Eisinas, Anatolijus. (2015). The Influence of Hydrothermal Treatment Duration on Gyrolite Synthesis // In: *Revista Romana de materiale = Romanian Journal of Materials*. Bucharest: Serban Solacolu Foundation. ISSN 1583-3186. Vol. 45, issue 3, p. 240–243.
6. Iljina, Aliona; Baltakys, Kęstutis; Bankauskaitė, Agnė; Eisinas, Anatolijus; Kitrys, Saulius. (2016). The stability of formed CaF_2 and its influence on the thermal behaviour of C-S-H in CaO-silica gel waste-H_2O system // *Journal of Thermal Analysis and Calorimetry*. ISSN 1388-6150. Vol. 127, issue 1, p. 221–228.

Publications of International Scientific Conferences

1. Iljina, Aliona; Baltakys, Kęstutis; Eisinas, Anatolijus. (2013). Zn^{2+} jonų adsorbcija girolitu skirtingo rūgštingumo tirpaluose // *Medžiagų inžinerija 2013* : respublikinė konferencija : konferencijos pranešimų santraukos, November 15, 2013, Kaunas / Kauno technologijos universitetas, Lietuvos

medžiagų tyrinėtojų asociacija. Kaunas: Technologija. ISSN 2345-0886. p. 16–17.
2. Iljina, Aliona; Baltakys, Kęstutis. (2014). Crystallization of C-S-H Compounds in CaO-Waste Silica Gel-H_2O Mixture when CaO/SiO_2 = 0.83 // In: *Proceedings of the BaltSilica 2014*, Poznan, Poland, June 1–3, 2014 / Editors: Wawrzynczak, A., Nowak, I. Poznan: Faculty of Chemistry, Adam Mickiewicz University. ISBN 9788-3627-8301-4. p. P-3.
3. Iljina, Aliona; Baltakys, Kęstutis. (2014). Crystallization of Z-Phase and Gyrolite in CaO – Waste Silica Gel – H_2O System // Chemistry and Chemical Technology : proceedings of the international conference, April 25, 2014 / Kaunas University of Technology. Kaunas: Technologija. ISSN 2351-5643. p. 61–63.
4. Iljina, Aliona; Baltakys, Kęstutis; Bankauskaitė, Agnė; Eisinas, Anatolijus. (2015). The Stability of Synthesized CaF_2 and Its Influence on the Thermal Behaviour of C-S-H // In: *3rd Central and Eastern European Conference on Thermal Analysis and Calorimetry, 25–28 August, 2015, Ljubljana, Slovenia: book of abstracts* / Editors: Andrei Rotaru, Romana Cerc Korošec. Rostock: Academia Greifswald. ISBN 978-3-940237-34-7. p. 296. PS2.42.
5. Iljina, Aliona; Baltakys, Kęstutis; Rudelis, Vaidas. (2016). Binding Peculiarities of F^- Ions in $Ca(OH)_2$ – Waste Silica Gel – H_2O System at 25 °C // In: *Proceedings of the BaltSilica 2016, Kaunas, Lithuania, 26–27 May, 2016* / Editors: Siaučiūnas, R., Bankauskaitė, A., Vaickelionis, G. Kaunas: Faculty of Chemical Technology, Kaunas University of Technology. ISSN 2243-6057. p. 83.

SL344. 2017-04-11, 13,75 leidyb. apsk. l. Tiražas 12 egz. Užsakymas 130
Išleido Kauno technologijos universitetas, K. Donelaičio g. 73, 44249 Kaunas
Spausdino leidyklos „Technologija“ spaustuvė, Studentų g. 54, 51424 Kaunas

Acknowledgments

I would like to gratefully acknowledge the enthusiastic and encouraging supervision of professor **Kestutis Baltakys** who has been providing me with invaluable counselling and advise on the thesis, and has also been showing nothing but confidence in me.

I also owe special thanks to professors R. Siaučiūnas and R. Kaminskas for their support, professional comments and valuable remarks.

I am highly grateful to all of my friends and colleagues from the Department of Silicate Technology, and especially to A. Bankauskaitė, T. Dambrauskas and A. Eisinas for their continual support and friendship. They all contributed to the success of this project in very different ways. Finally, I would like to thank my family and my fiancé, who, throughout my childhood and academic career have always been encouraging me to follow my heart and curious mind in whatever direction it may have taken me.

Appendices

Appendix 1

Table A1.1. Standard molar thermodynamic properties at 25 °C and 1 bar

Material	$\Delta H_{298}^{0,f}$, kJ·mol^{-1}	$\Delta G_{298}^{0,f}$, kJ·mol^{-1}	ΔC_p, J·mol^{-1}·K^{-1}	$\Delta S_{298}^{0,f}$, J·mol^{-1}·K^{-1}
$H_2O_{(v)}$	-241.8	-228.6	33.2	188.7
SiO_2	-910.9	-856.6	44.5	41.8
$Ca(OH)_2$	-985.1	-897.5	87.4	83.3
Z-phase	-3135.8	-	161.9	170.9
Gyrolite	-4914.4	-4550.1	325.9	271.2
1.4 nm tobermorite	-12175.1	-11090.1	973.5	874.5
1.1 nm tobermorite	-10680.9	-9889.2	764.9	692.5
Xonotlite	-10022.1	-9465.1	548.3	507.5
Okenite	-3135.7	-2881.7	210.0	208.5
Truscottite	-16854.6	-15280.4	1034.1	927.6

Appendix 2

Table A2.1. Standard molar thermodynamic properties at 25 °C and 1 bar

Material	$\Delta H_{298}^{0,f}$, kJ·mol^{-1}	$\Delta S_{298}^{0,f}$, J·mol^{-1}·K^{-1}	$C_p = f(T)$ coefficient			
			a	b·10^3	c·10^6	c'·10^{-5}
$H_2O_{(v)}$	-241.81	188.72	30.0	10.71	0.33	-
SiO_2	-910.94	41.84	46.99	34.31	-	-11.30
$Ca(OH)_2$	-985.12	83.39	105.19	12.01	-	-19.0
CaO	-635.09	38.07	49.62	4.52	-6.95	-
Z-phase	-3135.84	170.96	187.31	78.17	-43.26	-
gyrolite	-4914.43	271.28	332.19	151.73	-73.36	-
1.13 nm tobermorite	-10684.08	610.91	462.31	790.44	-	-
xonotlite	-10016.95	507.03	552.81	272.54	-76.70	-

Appendix 3

Table A3.1. Thermodynamic properties of reaction dependence on temperature for 1.13 nm tobermorite (1 and 4), Z-phase (2 and 5), and gyrolite (3 and 6) reactions at 373–723K

Reactions	T, K	373	423	473	523	573	623	673	723
1	$\Delta_r H_T^0$, kJ	-174.94	-177.48	-179.81	-181.63	-182.72	-182.95	-182.22	-180.45
	$\Delta_r S_T^0$, J	-160.32	-166.72	-171.95	-175.61	-177.61	-178.0	-176.88	-174.37
	$\Delta_r G_T^0$, kJ	-115.14	-106.96	-98.49	-89.79	-80.95	-72.06	-63.18	-54.39
3	$\Delta_r H_T^0$, kJ	-185.29	-188.04	-190.66	-193.18	-195.58	-197.88	-200.08	-202.17
	$\Delta_r S_T^0$, J	-243.84	-250.76	-256.62	-261.68	-266.07	-269.92	-273.31	-276.32
	$\Delta_r G_T^0$, kJ	-94.34	-81.97	-69.28	-56.32	-43.13	-29.72	-16.14	-2.40
4	$\Delta_r H_T^0$, kJ	665.83	661.83	657.79	653.86	650.12	646.64	643.46	640.61
	$\Delta_r S_T^0$, J	-64.13	-66.68	-68.78	-70.25	-71.04	-71.20	-70.75	-69.75
	$\Delta_r G_T^0$, kJ	-46.06	-42.78	-39.40	-35.92	-32.38	-28.82	-25.27	-21.76
6	$\Delta_r H_T^0$, kJ	-92.64	-94.02	-95.33	-96.59	-97.79	-98.94	-100.04	-101.08
	$\Delta_r S_T^0$, J	220.37	260.42	298.08	333.54	367.02	398.75	428.93	457.74
	$\Delta_r G_T^0$, kJ	-5065	-5077	-5091	-5107	-5124	-5143	-5164	-5186
8	$\Delta_r H_T^0$, kJ	23580	22552	21425	20232	18998	17735	16456	15167
	$\Delta_r S_T^0$, J	112.85	110.27	107.75	105.35	103.10	100.99	99.02	97.17
	$\Delta_r G_T^0$, kJ	-18.51	-24.09	-29.54	-34.87	-40.08	-45.18	-50.18	-55.09

Appendix 4

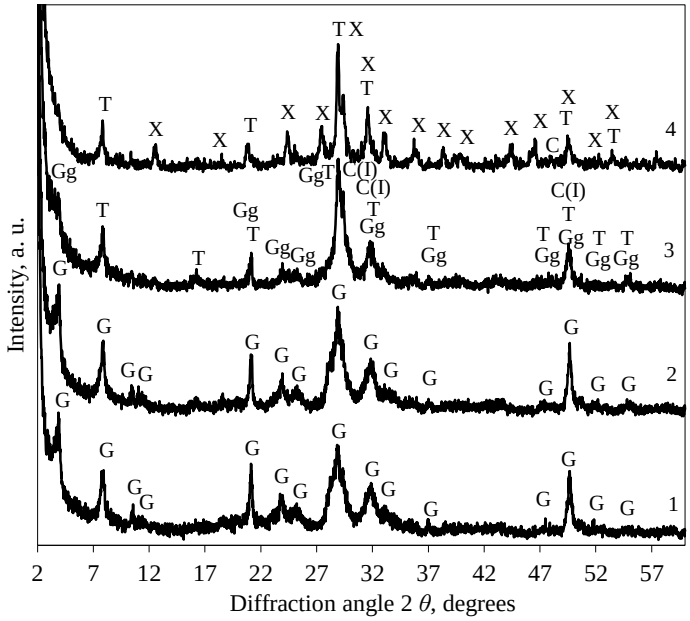

Fig. A4.1. XRD patterns of hydrothermal synthesis products after 48 h of isothermal treatment in the mixtures with amorphous silica oxide, when C/S molar ratio: 1 stands at 0.55; 2 stands at 0.66, 3 stands at 0.83, 4 stands at 1.0. Indexes: G denotes gyrolite, Gg denotes gyrolite gel, C(I) denotes CSH(I); T denotes 1.13 nm tobermorite; X denotes xonotlite, C denotes $CaCO_3$

Appendix 5

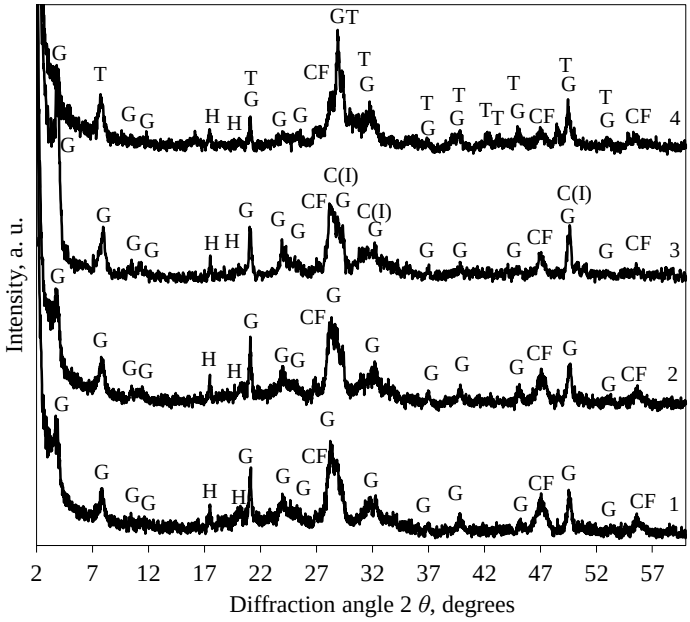

Fig. A5.1. XRD patterns of hydrothermal synthesis products after 48 h of isothermal treatment in the mixtures with AlF_3 production waste, when C/S molar ratio: 1 stands at 0.55; 2 stands at 0.66, 3 stands at 0.83, 4 stands at 1.0. Indexes: G denotes gyrolite, C(I) denotes CSH(I); T denotes 1.13 nm tobermorite; CF denotes CaF_2;
H denotes hydrogarnet